

**EXPERIMENTAL INVESTIGATION OF MICROSTRUCTURE AND  
PROPERTIES IN STRUCTURAL ALLOYS THROUGH IMAGE  
ANALYSES AND MULTIRESOLUTION INDENTATION**

A Dissertation  
Presented to  
The Academic Faculty

by

Almambet Iskakov

In Partial Fulfillment  
of the Requirements for the Degree  
Doctor of Philosophy in the  
George W. Woodruff School of Mechanical Engineering

Georgia Institute of Technology  
May 2021

**COPYRIGHT © 2021 BY ALMAMBET ISKAKOV**

**EXPERIMENTAL INVESTIGATION OF MICROSTRUCTURE AND  
PROPERTIES IN STRUCTURAL ALLOYS THROUGH IMAGE  
ANALYSES AND MULTIREOLUTION INDENTATION**

Approved by:

Dr. Surya R. Kalidindi, Advisor  
George W. Woodruff School of  
Mechanical Engineering  
*Georgia Institute of Technology*

Dr. Hamid Garmestani  
School of Materials Science and  
Engineering  
*Georgia Institute of Technology*

Dr. David L. McDowell  
George W. Woodruff School of  
Mechanical Engineering  
*Georgia Institute of Technology*

Dr. Sudhir Rajagopalan  
Siemens Corporate Technology  
*Siemens*

Dr. Richard W. Neu  
George W. Woodruff School of  
Mechanical Engineering  
*Georgia Institute of Technology*

Date Approved: January 21, 2021

To my family, for their unconditional love and support.

## ACKNOWLEDGEMENTS

In the first place, I would like to express gratitude to my advisor, Dr. Surya R. Kalidindi for his mentorship and guidance throughout the tenure of my PhD. I have gained many invaluable skills and knowledge through our interactions throughout the years.

I would like to thank Dr. David L. McDowell, Dr. Richard W. Neu, Dr. Hamid Garmestani, and Dr. Sudhir Rajagopalan for their participation in my defense committee and their valuable guidance.

I would also like to thank the Office of Naval Research (ONR N00014-18-1-2879) and our industry collaborator, Siemens (Dr. Sudhir Rajagopalan), for their support.

I am thankful to Dr. Jordan Weaver, Dr. Yuksel Yabansu, Dr. Ali Khosravani, Dr. Dipen Patel, Dr. Sepideh Parvinian, Dr. David Montes de Oca Zapiain, Berkay Yucel, Hyung Nun Kim and the rest of the research group for their support, collaboration, and friendship.

Lastly, I am thankful to my family and my friends who supported and encouraged me throughout the years.

# TABLE OF CONTENTS

<b>ACKNOWLEDGEMENTS</b>	<b>iv</b>
<b>LIST OF TABLES</b>	<b>vii</b>
<b>LIST OF FIGURES</b>	<b>ix</b>
<b>SUMMARY</b>	<b>xiii</b>
<b>CHAPTER 1. Introduction</b>	<b>1</b>
1.1 Challenges in mechanical property testing at multiple length scales	3
1.2 Indentation stress-strain (ISS) protocols	4
1.3 Evaluation of microstructure statistics analysis through micrographs	5
1.4 Research objectives	6
<b>CHAPTER 2. Mechanical characterization of hierarchical materials at multiple length scales</b>	<b>9</b>
2.1 Kalidindi and Pathak spherical indentation (ISS) stress-strain protocols	9
2.1.1 Microindentation stress-strain protocols	10
2.1.2 Nanoindentation stress-strain protocols	15
2.1.3 Application of ISS protocols on small volume samples excised from high-temperature exposed components	17
<b>CHAPTER 3. Microstructure image segmentation framework</b>	<b>25</b>
3.1 Introduction	27
3.2 Challenges in segmentation	30
3.3 Segmentation framework	32
3.3.1 Image acquisition	35
3.3.2 Image preprocessing for segmentation	40
3.3.3 Segmentation	51
3.3.4 Post-processing	54
3.3.5 Segmentation validation	56
3.4 Segmentation workflows	58
3.4.1 Custom-built workflow for Ni-based superalloy microstructures	59
3.4.2 Templated segmentation workflows	61
3.5 Conclusions	67
<b>CHAPTER 4. Application of protocols to multiresolution study of thermally aged ferrite-pearlite steels</b>	<b>69</b>
4.1 Introduction	69
4.2 Thermally aged ferrite-pearlite steels	70
4.3 Sample Preparation	72
4.4 Image Segmentation	73
4.5 Mechanical characterization results	79
4.5.1 Evaluation of bulk properties with microindentation	80

4.5.2	Evaluation of ferrite and pearlite constituents with nanoindentation	82
<b>4.6</b>	<b>Correlation of yield strength at multiple scales</b>	<b>84</b>
4.6.1	Rule of mixtures	85
4.6.2	Self-consistent model	87
4.6.3	Results of composite model evaluation	89
<b>4.7</b>	<b>Conclusions</b>	<b>91</b>
<b>CHAPTER 5.</b>	<b>Conclusions</b>	<b>93</b>
<b>5.1</b>	<b>Future Work</b>	<b>95</b>
<b>REFERENCES</b>		<b>97</b>

## LIST OF TABLES

Table 1	– Specimens received for study with different exposure conditions. Superscript * indicates samples where tensile test specimen were made in addition to microstructure and indentation measurements.	19
Table 2	– Measurements obtained from tensile and microindentation tests for Unexposed and 91-0.85ST samples. Note the higher variance in the indentation measured yield strengths.	22
Table 3	– Summary of the five steps of the segmentation framework developed in this work. Within each step, tasks and subtasks are specified. Examples of available methods to be considered for addressing each subtask are also specified.	34
Table 4	– Functions available for image noise reduction in MATLAB [87] and Python scikit-image [145].– Functions available for image contrast enhancement in MATLAB [87] and Python scikit-image [145].	47
Table 5	– Functions available for image contrast enhancement in MATLAB [87] and Python scikit-image [145].	50
Table 6	– Functions available for image segmentation in MATLAB [87] and Python scikit-image [145].	51
Table 7	– Functions available for post-processing in MATLAB [87] and Python scikit-image [145].	54
Table 8	– Custom-built segmentation workflow for segmentation of Ni-based superalloy microstructures.	60
Table 9	– Templated workflows that can be used in the segmentation of most microstructure images.	64
Table 10	– Specimens received for study with different exposure conditions. Superscript * indicates samples where tensile test specimen were made in addition to microstructure and indentation measurements.– Summary of microstructure statistics and indentation measurements on the thermally aged steels samples.	73
Table 11	– Summary of microstructure statistics and indentation measurements on the thermally aged steels samples.	84

Table 12 – Indentation yield strength of pearlite-ferrite steel samples from microindentation measurements and the predicted indentation from composite models (average and one standard deviation). An average MAPE (mean absolute percentage error) between the indentation yield strength estimated by each composite model is displayed at the bottom.

89

## LIST OF FIGURES

- Figure 1 - Hierarchical structure of ferrite-pearlite steel. 2
- Figure 2 - Example of raw microscopy image of a microstructure with precipitates (darker object), its segmented version (precipitates labelled as white pixels), and quantification of the segmented precipitates using 2-point spatial correlations. 6
- Figure 3 – Schematic of spherical indentation at different stages of the indentation test. a) initial elastic contact between the indenter and the sample, b) load at which plastic deformation in sample occurs, c) complete unload after plastic deformation in the sample. 13
- Figure 4 – An example of microindentation test data. (a) The measured load-displacement data in multiple load-unload cycles. Highlighted red data corresponds to the initial elastic portion used to determine  $E_{ind}$ . (b) Indentation stress-strain (ISS) data extracted from the load-displacement data. Each post-elastic point on the ISS curve corresponds to an individual unload cycle in the load-displacement measurement. The yield point,  $Y_{ind}$ , is determined from the intersection of the linear fit of post-elastic data with the 0.2% indentation strain offset. 15
- Figure 5 – Schematic of a nanoindentation stress-strain protocol analysis, (a) load displacement data, (b) extracted indentation stress-strain curve from the test data. 17
- Figure 6 – Schematic of mechanical test specimens extracted from turbine components and their relative sizes. Left side shows round tension test specimen. Right side shows epoxy-mounted scoop specimen (after scoop trimming and polishing). 19
- Figure 7 – (a) Tensile stress-strain curves with 0.2% offset for the Unexposed and the 91-0.85ST specimens. Considerable reduction in yield strength is observed between Unexposed (average yield strength = 311 MPa), and after 91,000 service hours at 0.85ST (average yield strength = 221 MPa). (b) An example SEM-BSE micrograph for the Unexposed sample. (c) An example SEM-BSE micrograph for the 91-0.85ST sample (black particles are graphite). 20

Figure 8	– Tensile stress-strain curve and scaled indentation stress-strain data for Unexposed specimen.	23
Figure 9	– Summary of the measured tensile and scaled indentation yield strengths with error bars representing one standard deviation. A trend of changing yield strength with increasing service time is clearly discernible.	24
Figure 10	– A schematic of an image segmentation example. Left side shows a raw microscopy image in grayscale with pixel values ranging between 0 and 255. Right side shows the segmented version of the raw with pixels values of only 0 or 1.	26
Figure 11	– Examples of challenges encountered in the segmentation of feature regions in micrographs: a) Ni-based superalloy microstructure image showing clear features but of low contrast resulting in poor segmentation (see regions near the arrows in the top and bottom images), b) segmentation of an image with pixel-level noise, c) segmentation of image with global shadow gradient in its intensity, d) image with oversegmentation that requires post-processing (see regions near the arrows in the top and bottom images).	32
Figure 12	– a) SEM images of the same location in steel microstructure using BSE detector (left) and SE detector (right). Foreign inclusion shows as a dark feature similar to graphite (darker colored regions) in SEM-BSE image, whereas it is clearly distinguishable in SEM-SE image on right. b) SEM images of the same Ni-based superalloy sample using BSE detector (left) and SE detector (right). The combination of etched $\gamma'$ precipitates and SEM-BSE imaging (left) yields better contrast between $\gamma$ and $\gamma'$ , compared to etched $\gamma$ matrix and SEM-SE imaging (right).	37
Figure 13	– Images of a $50\ \mu\text{m} \times 50\ \mu\text{m}$ area taken with different spatial resolutions: a) higher spatial resolution image ( $0.05\ \mu\text{m}/\text{px}$ ), and b) lower spatial resolution image ( $0.2\ \mu\text{m}/\text{px}$ ). Note the lower fidelity of the feature detail in (i) and nearly indistinguishable small feature in (ii) in the lower resolution image.	39
Figure 14	– Example of intensity gradient noise reduction from an SEM image: a) input image $I$ with intensity gradient, b) approximated intensity gradient $f$ , and c) corrected image $I_R$ .	42

Figure 15	– Random noise reduction using Gaussian filtering on input image in the middle row of a). Top row shows the removed noise, $R$ , corresponding to different filter strengths. The middle row shows the associated filtered images $I_F$ , and the bottom row shows segmented versions of the filtered images obtained by using simple thresholding. Higher values of $\sigma$ results in loss of image detail, while lower values leave some of the local noise in the image. Optimal filtering is close to image c), between $\sigma = 1$ and $\sigma = 1.5$ .	45
Figure 16	– Examples of global and local contrast enhancement: a) input image with low contrast, b) contrast stretching with bottom and top 1% intensity saturation, c) bottom 0% and top 15% saturation, d) global histogram equalization, e) contrast-limited adaptive histogram equalization (CLAHE).	49
Figure 17	– a) Input image and b) modified image using unsharp filtering. Note that the contrast is increased around feature edges, but the visual appearance is not necessarily enhanced.	50
Figure 18	– Segmentation examples: a) TiMn alloy, where the dark regions are the $\alpha$ -Ti and light regions are $\beta$ -Ti, and c) segmented result of a) using intensity thresholding. b) Ni-based superalloy microstructure with $\gamma'$ precipitates and $\gamma$ matrix, and d) segmented result of b) using edge detection.	53
Figure 19	– Examples of post-processing on segmented images: a) image closing to connect objects that are close to each other, b) image opening to disconnect objects with thin bridges, c) removal of small objects, d) removal of objects cut by the image boundaries.	55
Figure 20	– Qualitative segmentation validation examples. a) original image, b) segmented image, c) outline of segmented features, d) overlay of segmented features, e) labelled contiguous features.	57
Figure 21	– Ni-based microstructure images at each of the five steps (images a)-e)) of the custom-built segmentation workflow.	61
Figure 22	– Previously acquired microstructure raw images (left column) and their segmented results utilizing the three templated workflows (right three columns) identified in Table 9.	66

Figure 23	– Example optical microscopy (OM) microstructure images at different magnifications for different levels of thermal exposure. a) unexposed sample with ferrite (f) and lamellar pearlite (p), b) moderate exposure sample with pearlite spheroidization (at higher magnification than a) and c)), c) high exposure sample with pearlite spheroidization and graphitization (g). The details of exposure times and temperature are provided in Table 10.	71
Figure 24	– Illustration of the individual steps in the segmentation workflow developed and implemented on the images studied in this work. Note that these images show a magnified region of the original image to display the microstructure details. a) Acquired raw image from optical microscopy, b) preprocessed image with removed noise and increased contrast, c) segmented image showing three microstructural states, d) post-processed image, and e) visualization of segmented pearlite (outlined in magenta) on the preprocessed image.	78
Figure 25	- Example of visualization of segmented images for the thermally aged samples.,(a) Unexposed sample, (b) moderate exposure, (c) high exposure.	79
Figure 26	– a) Top view of residual indentation impression after a microindentation test, where the yellow outline corresponds to the contact area at indentation yield stress displayed on an etched sample, b) top view of residual indentation impression (arrow) after a nanoindentation test within a ferrite grain.	81
Figure 27	– Microindentation yield strength measured for the thermally exposed samples in this study.	81
Figure 28	– Examples of nanoindentation load-displacement (left column) and corresponding indentation stress-strain curves (right column) for (a) ferrite and (b) pearlite constituents for all samples.	83
Figure 29	– Comparison of indentation yield strength from evaluated composite models to the microindentation measurements.	91

## SUMMARY

This work addresses the challenges in the investigation of structural alloy microstructures and their mechanical properties at multiple length scales. The investigations are performed on small volume ferrite-pearlite steel samples that were excised from in-service gas turbine components after prolonged exposure (up to 99,000 hours) to elevated temperatures, which promotes microstructural changes (spheroidization of pearlite and graphitization) as well as their yield strengths. Recent advances in spherical indentation protocols are combined for the first time to investigate the mechanical response of microscale ferrite-pearlite constituents and estimates of bulk properties on macroscale. It is shown that indentation yield strength captured with large indenter tips on an ensemble of ferrite-pearlite grains correlate strongly to the bulk yield strength evaluated with tensile measurements. Measurements on the individual ferrite and pearlite constituents follow a similar trend of decreasing yield strength as the bulk measurements.

Second, to advance the reliability and accuracy of microstructure characterization, an image segmentation framework is developed that consists of five main steps designed to achieve systematic image segmentation on broad classes of microstructures utilizing widely available image processing tools. The flexibility and modularity of the framework was demonstrated on various types of microstructures images. The developed framework was used to segment the microstructures of ferrite-pearlite samples. The extracted microstructure statistics from the segmented images and multiresolution indentation yield strength measurements were used to evaluate established composite theory estimates and have demonstrated highly consistent estimates for these material systems.

# CHAPTER 1.

## INTRODUCTION

Many materials innovation efforts are focused on the study and development of high performance hierarchical materials that are needed in advanced technology applications [1-4]. Our understanding and ability to design high performance materials critically depends on experimental characterization of heterogeneous microstructures and their properties at multiple length scales. However, this task is not easy, and even for a single alloy requires high effort and considerable time to perform. New protocols are urgently needed that can reliably evaluate heterogeneous material microstructures and their mechanical properties at multiple resolutions in a high-throughput manner.

Most structural alloys exhibit hierarchical microstructures that consist of multiple constituents (e.g., thermodynamic phases) at different material structure/length scales [5-8]. The complex spatial arrangements of these constituents in the material's representative volume control the effective mechanical properties used by designers of engineered components made from these alloys [9-11]. An example of hierarchical structure of ferrite-pearlite steel is shown in Figure 1, where different chemical compositions form individual phases of  $\alpha$ -ferrite and cementite ( $\text{Fe}_3\text{C}$ ), and the lamellar arrangement of  $\alpha$ -ferrite and cementite form pearlite grains and  $\alpha$ -ferrite grains, and finally, the spatial arrangement of ferrite and pearlite grains form a polycrystalline aggregate of the component material. Many steel alloy microstructures often consist of soft ferrite matrix and hard grain-scale constituents (e.g., pearlite, martensite), which influence strongly the steel's overall mechanical properties such as strength and ductility [5, 12-15]. Consequently, many

materials innovation efforts have been focused on the design of material microstructures for improved effective mechanical properties needed in advanced technology applications.

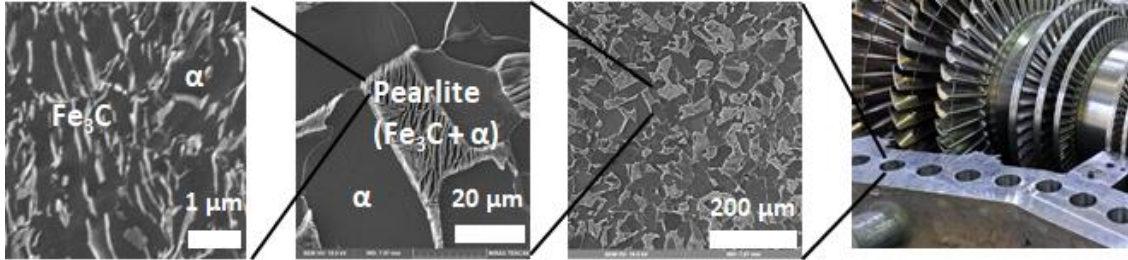


**Figure 1 - Hierarchical structure of ferrite-pearlite steel.**

Even for a single alloy, the microstructure space can be vast, and the optimization of its mechanical properties is not practical without the theoretical guidance of physics-based models. Composite theories addressing heterogeneous materials have presented avenues to guide and accelerate the optimization of properties [16-23]. In particular, homogenization models relate the material's overall mechanical response to the details of its microstructure, and have been successfully demonstrated on various material systems [2, 24-27]. In order to successfully guide the design of hierarchical materials through physics-based models, evaluation of microstructure and their properties at multiple length scales is essential. Specifically, this requires evaluation of (i) the individual properties of the microscale constituents, (ii) the macroscale effective properties, and (iii) relevant microstructure statistics.

A significant hurdle in the advancement of composite theories necessary for hierarchical materials design has been the lack of a sufficiently large experimentally measured datasets of microstructures and their effective properties. The focus of this dissertation is to bridge this gap by developing and demonstrating protocols for reliable

and high-throughput experimental evaluation of microstructures and mechanical properties at multiple resolutions. This is achieved by developing a framework for design of workflows for micrograph image segmentation and by extending multiresolution spherical indentation stress-strain protocols recently developed by Kalidindi and Pathak [28]. The challenges in current experimental evaluation of mechanical properties and image segmentation are introduced next, followed by the scope of this dissertation.

### **1.1 Challenges in mechanical property testing at multiple length scales**

One of the major challenges in multi-length scale testing comes from the need to measure the mechanical properties of individual microscale constituents at very small length scales that must be performed on very small material volumes, often on the order of microns [29-31]. Most of the current methods used at the different material structure/length scales are very different from each other, require substantial investment of time and effort, and produce very limited data (i.e., low throughput). As a result, it has not been easy to collect consistent and reliable multiresolution mechanical property information on heterogeneous materials. Conventionally, evaluation of macroscale mechanical properties has been performed using uniaxial tension [32] and compression [33] tests to extract stress-strain curves, which have been standardized and widely adopted. However, adaptation of uniaxial testing to microscale constituents using miniaturized versions of uniaxial tension [30, 31] or micropillar compression [29, 34] tests has proven to be challenging. Small scale uniaxial testing usually requires significant effort and highly specialized equipment for sample preparation, such as focused ion beam (FIB) milling for micropillar sample fabrication.

As a lower-cost and high-throughput alternative to uniaxial testing, indentation testing has been performed for many decades. Traditionally, indentation methods utilize sharp tip geometries [35] (e.g., Vickers, Berkovich) to probe the mechanical response of the material. However, the main limitation of these protocols is that they measure hardness values at a specified load/depth and lack the insight into the intrinsic mechanical properties captured by uniaxial tests. In fact, there have been many efforts to scale hardness measurements to uniaxial stress-strain properties such as the tensile yield strength and ultimate tensile strength for various alloys [36-40]. However, these studies generally report high variability in hardness measurements on the same material and across different length scales [39, 41-43], making it difficult to rely on these results for guiding the efforts aimed at the refinement of the multiscale composite theories mentioned earlier.

## **1.2 Indentation stress-strain (ISS) protocols**

Recently Kalidindi and Pathak [28] have demonstrated rigorous protocols capable of extracting reliable and useful indentation stress-strain (ISS) curves using spherical indenters. The consistency and fidelity of these protocols have been demonstrated at multiple material length scales [44-55] using different indenter tip sizes. These demonstrations have included measurements within regions inside individual grains [44, 45, 48, 49, 51, 52] as well as on an ensemble of grains [50, 55-59]. These protocols have been validated using a combination of measurements on samples where ground-truth data (from standard tension tests) was available [50, 55, 57, 59] as well as with numerical simulations of the indentation experiment [60, 61].

### **1.3 Evaluation of microstructure statistics analysis through micrographs**

The second major challenge in the study of the heterogenous materials comes from the need to label the features of interest (i.e., segment) in the raw microstructure images (two or three-dimensional) obtained in microscopy protocols used for evaluation of microstructure statistics (e.g., thermodynamic phase volume fraction, n-point statistics [62, 63]). Often, the raw microscopy images are produced in grayscale, where each pixel (or voxel) is assigned a grayscale value between 0 and 255, as shown in Figure 2. However, the number of distinct features of interest (e.g., thermodynamic phases) present in the sample is typically far smaller than the number of grayscales in the raw images (refer to middle image in Figure 2). Evaluation of microstructure statistics is commonly performed on segmented microstructure features represented in images collected using various microscopy techniques (refer to right image in Figure 2). Raw microscopy images typically contain noise that is often highly heterogeneous and requires segmentation procedures with multiple image processing functions to tackle various types of noise arising from a combination of equipment or sample conditions in the imaging protocols. Therefore, segmentation protocols need to be designed to produce the correct labelling of the microscale features of interest in the microstructure images. This task is generally achieved by assembling together a workflow using a variety of image processing functions and filters [64-68]. One of the major hurdles encountered in this process is that the successful construction and implementation of the workflow leading to accurate segmentation is highly dependent on the user's expertise in the application of the image processing functions. Consequently, these efforts often lead to non-standard approaches that can strongly influence the accuracy of the microstructure analysis. To resolve the challenges

described above, new protocols are critically needed that reduces the dependence on user's expertise in image processing to design workflows leading to consistent and reliable segmentation results.

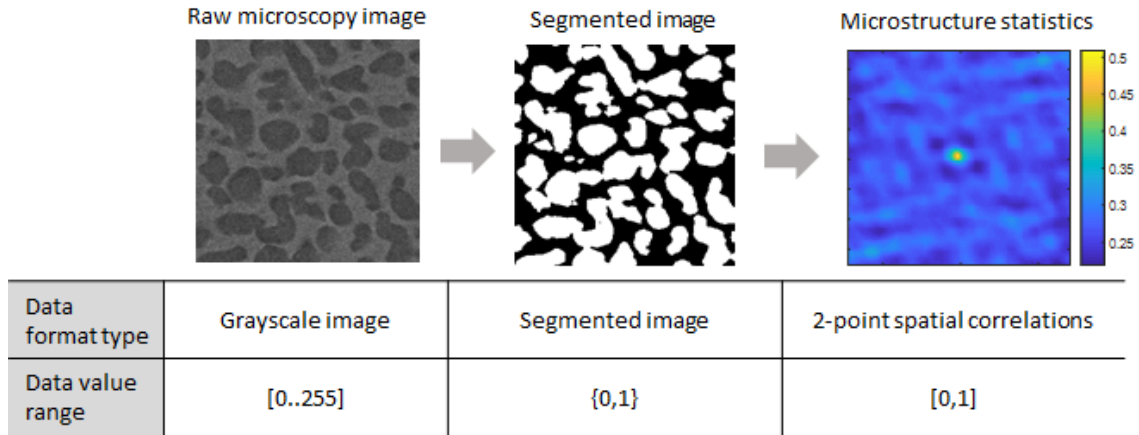


**Figure 2 - Example of raw microscopy image of a microstructure with precipitates (darker object), its segmented version (precipitates labelled as white pixels), and quantification of the segmented precipitates using 2-point spatial correlations.**

#### 1.4 Research objectives

This dissertation focuses on developing and demonstrating protocols for reliable and systematic investigation of microstructures and mechanical response of heterogeneous materials across multiple length scales. The research objectives are described below, and are demonstrated in a case study on ferrite-pearlite steels:

- (i) Extension of spherical indentation stress-strain (ISS) protocols (by Kalidindi and Pathak [28]) to multiresolution testing of hierarchical material microstructures.

- (ii) Development and demonstration of a framework for systematic design of segmentation workflows for image segmentation required for microstructure analysis.
- (iii) Apply the protocols developed in (i) and (ii), investigate microstructures and mechanical properties of thermally aged ferrite-pearlite steels.
- (iv) Apply the measurements collected in (iii) to evaluate simple composite theories.

First, the ISS protocols by Kalidindi and Pathak [28] for multiresolution mechanical evaluation are covered in Chapter 2, and are extended to testing bulk properties of small scoops samples extracted from gas in-service turbine components. In Chapter 3, a novel framework for systematic design of workflows for micrograph image segmentation is developed and demonstrated.

Using the developed protocols, Chapter 4 presents a case study investigating the microstructures and mechanical properties at multiple resolutions of thermally aged ferrite-pearlite steels. The prolonged thermal aging exposures (up to 91,000 hours) in these steel samples contribute to significant changes in the microstructure and yield strength [69-73]. In this investigation, ISS protocols are applied on the individual microscale constituents (i.e., ferrite, pearlite, and graphite) as well as at the macroscale. The respective yield strengths of the microscale constituents and the bulk yield strength of the sample were estimated from these measurements. The microstructures of these samples were documented using optical microscopy (OM), where images were segmented and the relevant microstructure statistics were extracted. All of this information was used to

evaluate simple composite theory estimates. Finally, in Chapter 5, the main conclusions of this dissertation are presented and possible future work is discussed.

## **CHAPTER 2.**

# **MECHANICAL CHARACTERIZATION OF HIERARCHICAL MATERIALS AT MULTIPLE LENGTH SCALES**

As mentioned earlier, evaluation of mechanical properties at multiple length scales presents formidable challenges in study of hierarchical materials. One of the main challenges in testing mechanical properties across multiple length scales is that most of the current testing methods used at the different length scales are very different from each other, require substantial effort, and produce limited data (i.e., low throughput). The novel protocols recently developed by Kalidindi and Pathak have demonstrated the capability of extracting indentation stress-strain (ISS) curves in a high-throughput manner at multiple resolutions using different spherical indenter sizes [51, 53, 55, 58, 74-77].

### **2.1 Kalidindi and Pathak spherical indentation (ISS) stress-strain protocols**

The instrumented spherical indentation stress-strain protocols developed by Kalidindi and Pathak [36] have demonstrated a robust, high throughput ability to extract mechanical properties from small material volumes [28, 45, 46, 74, 78]. Most of the early effort of studies utilizing ISS was focused on very small length scales of the volumes probed in the indentation tests (controlled mainly by the indenter tip radii), which typically varied between ~50 nms to ~5 microns. This is because these prior studies were aimed at studying mechanical response of volumes within individual grains of a polycrystalline sample, referred to as nanoindentation protocols. Nanoindentation tests typically require low forces ( $\ll 10$  N) and benefit from continuous stiffness measurement (CSM) [28, 45,

47, 48, 78] for reliably estimating the changes in the contact radius during the indentation tests.

Only recently [49, 50, 56], ISS protocols have been extended to studies where the sizes of the indentation zones are of the order of several hundreds of microns, referred to as microindentation protocols. The indentation stress-strain curves obtained using microindentation aim to capture the overall response of a polycrystalline aggregate with relatively large indenter tips (0.5-6.35 mm in radius). Previous microindentation measurements have been shown to be well-correlated to the stress-strain curves measured in conventional tension/compression tests [50, 61]. Typically, indentations with the larger tip radii require larger forces ( $\gg 10$  N). Suitable instrumented testing machines allowing for these larger indents along with the CSM capability are not yet commercially available. In order to address this gap, suitable approaches have been developed [46, 49, 50, 56] that employ multiple load-unload cycles during the test. It is important to note that microindentation protocols produce a more discrete indentation stress-strain curve compared to the ones produced using nanoindenters with a built-in CSM capability. Both microindentation and nanoindentation protocols are largely based on Hertz's contact theory and are described next.

### *2.1.1 Microindentation stress-strain protocols*

The extraction of stress-strain response from microindentation tests follows the recently developed protocols [46, 50] to convert the measured load-displacement data to indentation stress-strain curves based on Hertz's theory. As mentioned earlier, due to instrumentation limitation, microindentation tests are currently performed without the

CSM and therefore multiple load-unload cycles must be performed to produce the indentation stress-strain curve.

Hertz theory [79] for frictionless, elastic contact between two isotropic, homogeneous bodies with quadratic surfaces can be expressed using the following relations:

$$P = \frac{4}{3} E_{eff} R_{eff}^{1/2} h_e^{3/2} \quad (1)$$

$$a = \sqrt{R_{eff} h_e} \quad (2)$$

$$\frac{1}{E_{eff}} = \frac{1 - \nu_s^2}{E_s} + \frac{1 - \nu_i^2}{E_i} \quad (3)$$

$$\frac{1}{R_{eff}} = \frac{1}{R_s} + \frac{1}{R_i} \quad (4)$$

where  $P$  and  $h_e$  denote indentation load and elastic displacement, respectively,  $R$  and  $E$  are the radius and Young's modulus, and  $a$  denotes the indentation contact radius. Subscripts  $s$  and  $i$  are associated with sample and indenter, respectively, while  $R_{eff}$  and  $E_{eff}$  are the effective radius and elastic modulus of the indenter-sample system.

The central strategy in the spherical indentation stress-strain protocols employed in this work is to utilize Hertz's theory to estimate  $E_{eff}$  from the initial elastic loading segment (before the onset of any plastic deformation in the sample), and subsequently use

the same value of  $E_{eff}$  to estimate the evolving  $R_{eff}$  by analyzing the elastic unloading segments (again using Hertz's theory).

First, the analysis of the initial load cycle is utilized to achieve two goals: (i) estimate the initial contact between the indenter and the sample (i.e., zero-point correction) and (ii) estimate the elastic modulus of the indenter-sample system,  $E_{eff}$ . Zero-point correction is critical to mitigate common issues related to the sample (e.g., surface roughness, surface oxide layer) and the indenter (e.g., shape imperfections) that can affect consistent analysis using Hertz's theory [28]. The estimation of zero-point load and displacement correction ( $P^*$  and  $h^*$ ) for indentation without CSM signal has been outlined in prior work [46] and is performed on recast Eq. (1):

$$(\tilde{h}_e - h^*) = k(\tilde{P} - P^*)^{\frac{2}{3}}, \quad k = \left[ \frac{3}{4} \frac{1}{E_{eff}} \frac{1}{\sqrt{R_{eff}}} \right]^{2/3}, \quad (5)$$

$\tilde{P}$  and  $\tilde{h}$  are the raw load and displacement measurements, respectively. During the initial elastic loading on a flat sample surface, shown in Figure 3, the effective radius of the indenter-sample system is equal to the radius of the indenter, i.e.,  $R_{eff} = R_i$ . The values of  $h^*$  and  $E_{eff}$  are estimated by performing regression on  $\tilde{h}_e$  and  $\tilde{P}$  in Eq. (5), whereas the value of  $P^*$  is selected as one that minimizes the log of the average absolute error of the regression fit. In microindentation experiments, the sample surface and tip disparities are very small compared to the tip radii and in many cases, there is no need for load correction.  $E_s$  is then obtained from Eq. (3) by using Poisson ratio ( $\nu_s$ ) for the sample and Poisson ratio ( $\nu_i$ ) and Young's modulus  $E_i$  for the indenter material.

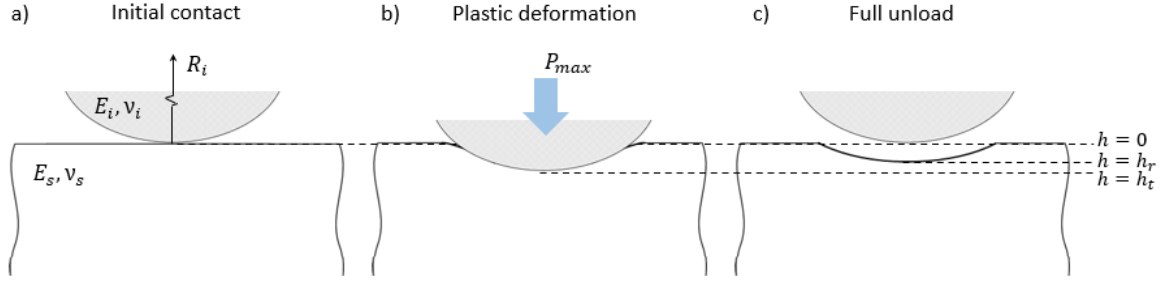


**Figure 3 – Schematic of spherical indentation at different stages of the indentation test. a) initial elastic contact between the indenter and the sample, b) load at which plastic deformation in sample occurs, c) complete unload after plastic deformation in the sample.**

After plastic deformation of the sample shown in Figure 3c, the total displacement,  $h$ , consists of elastic displacement,  $h_e$ , and residual displacement,  $h_r$ , represented using the following relations:

$$h = kP^{2/3} + h_r. \quad (6)$$

The coefficients  $k$  and  $h_r$  are determined using regression techniques on the measured load and total displacement during the unload data (95-50% of peak force). Subsequently,  $R_{eff}$  is extracted from Eq. (5), where  $E_{eff}$  is assumed to remain constant from the initially established value. This is a reasonable assumption because the average plastic deformations are very small in these indentations. The contact radius,  $a$ , is then determined using the following Hertz's relation:

$$a = \sqrt{R_{eff}(h_{s,max} - h_r)}, \quad (7)$$

where  $h_{s,max}$  is the indentation displacement in the sample at the peak of each loading cycle. The indentation stress,  $\sigma_{ind}$ , and indentation strain,  $\varepsilon_{ind}$ , are defined as:

$$\sigma_{ind} = \frac{P_{max}}{\pi a^2} \quad (8)$$

$$\varepsilon_{ind} = \frac{3}{4\pi} \frac{h_{s,max}}{a} \approx \frac{h_{s,max}}{2.4a} \quad (9)$$

$$h_s = h - h_i \quad (10)$$

$$h_i = \frac{3(1 - \nu_i^2)P}{4E_i a} \quad (11)$$

where  $h_s$  denotes the sample displacement and  $h_i$  is the elastic deformation of the indenter. Eq. (10) estimates the indenter elastic displacement by assuming that it is subjected to the applied load against a flat rigid surface. The indentation strain defined in the above equations can be interpreted as compressing by distance  $h_s$  an idealized indentation zone of cylindrical region of radius  $a$  and height  $2.4a$ . This definition of indentation strain can be visualized as change of length per unit length and is more physical than commonly used indentation strain definitions, and has been validated in several prior studies [28, 46, 50, 60]. After several load-unload cycles, an ISS curve is constructed with the post-elastic indentation stress-strain data and with indentation modulus  $\frac{E_s}{(1-\nu_s^2)}$ , as shown in Figure 4. Using the ISS curve, the indentation yield strength is determined using a 0.2% indentation strain offset intersection with a linear fit of post-elastic data.

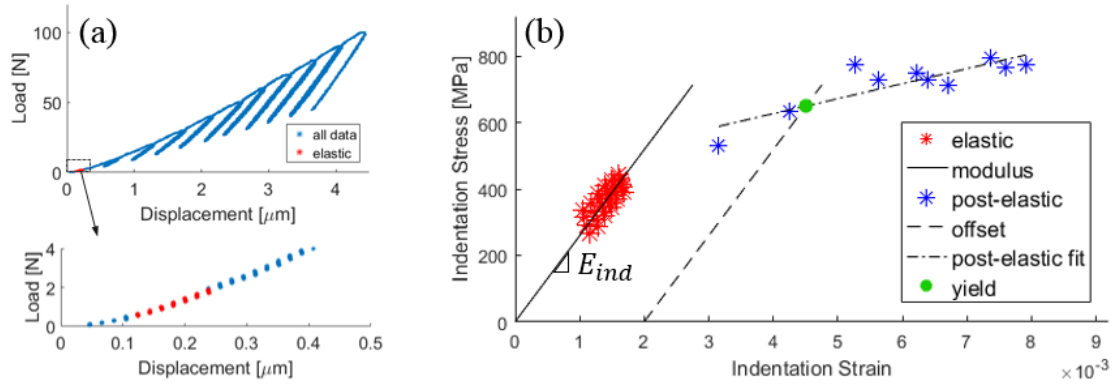


**Figure 4 – An example of microindentation test data. (a) The measured load-displacement data in multiple load-unload cycles. Highlighted red data corresponds to the initial elastic portion used to determine  $E_{ind}$ . (b) Indentation stress-strain (ISS) data extracted from the load-displacement data. Each post-elastic point on the ISS curve corresponds to an individual unload cycle in the load-displacement measurement. The yield point,  $Y_{ind}$ , is determined from the intersection of the linear fit of post-elastic data with the 0.2% indentation strain offset.**

### 2.1.2 Nanoindentation stress-strain protocols

Nanoindentation stress-strain protocols are extensively used to evaluate microscale constituents (e.g., measurements within grains) and utilize much smaller indenters than microindentation. Thus, unlike microindentation, the accuracy of nanoindentation analysis tend to be sensitive to both load and displacement zero-point corrections. In addition, the zero-point correction methodology determined by the current nanoindentation protocols (Kalidindi and Pathak) can differ from the protocols that are often built-in into indentation machines with CSM capability. Values identified by machines (e.g., analysis software) may be susceptible to common sample or indenter tip issues mentioned earlier that can affect the accuracy of the test analysis [28]. The determination of zero-point load and displacement corrections ( $P^*$  and  $h^*$ ) with CSM-enabled nanoindentation protocols is performed using the following Hertz’s theory relation:

$$S = \frac{3P}{2h_e} = \frac{3(\tilde{P} - P^*)}{2(\tilde{h} - h^*)}, \quad (12)$$

where  $S$  is the elastic unloading stiffness measured with CSM. The  $P^*$  and  $h^*$  zero-point correction values can be extracted by recasting Eq. (12) and performing linear regression between the raw  $\tilde{P}$  and  $\tilde{h}_e$  measurements [28]:

$$\tilde{P} - \frac{2}{3}S\tilde{h}_e = -\frac{2}{3}h^*S + P^*. \quad (13)$$

After the zero-point corrections have been applied, the effective elastic modulus,  $E_{eff}$ , is extracted from the initial elastic loading segment and performing regression on  $P$  and  $h^{3/2}$  in Eq. (1). This is possible because during the initial elastic loading the sample surface remains flat and without permanent deformation and  $R_{eff} = R_i$ . The  $E_{eff}$  value is assumed to remain constant throughout the test and is further used in estimation of the constantly evolving indentation contact radius,  $a$  following Hertz's theory:

$$a = \frac{S}{2E_{eff}}. \quad (14)$$

An example of an extracted nanoindentation stress-strain curve using the nanoindentation protocol is shown in Figure 5.

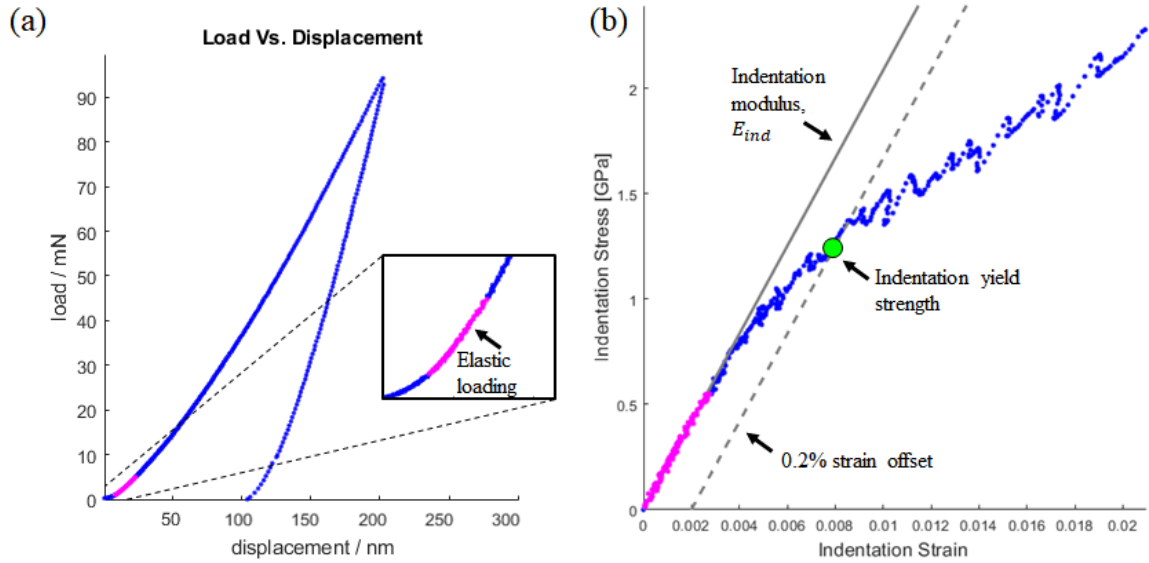


**Figure 5 – Schematic of a nanoindentation stress-strain protocol analysis, (a) load displacement data, (b) extracted indentation stress-strain curve from the test data.**

### 2.1.3 Application of ISS protocols on small volume samples excised from high-temperature exposed components

In this case study, we explore for the first time, the feasibility of applying the novel microindentation stress-strain protocols described earlier on small scoop samples excised from in-service gas turbine components and correlating them to measurements from tensile tests. The material of interest for the present study is a 0.35 wt.% carbon steel, used extensively in turbine equipment. The study is based on a library of small scoop samples excised from similar locations in structural turbine components subjected to prolonged periods of service time at elevated temperatures. Prolonged exposure at elevated temperatures promotes microstructural changes (graphitization and spheroidization) [69-71, 73, 80, 81] that is typically accompanied with a change in the mechanical properties,

as documented in prior work using tensile tests [71, 72, 80]. Accurate assessment of the change in mechanical properties, such as yield strength, with service exposure is critical for life cycle management of such components, which can exceed operational lifetime of 100,000 hours [82]. However, nondestructive mechanical testing of the material in operating components is not possible using conventional uniaxial tests, which require a substantial volume of material to be extracted. As a consequence, a practical way forward has been to excise small shallow scoops from the in-service components at selected time intervals in their service lifetime, and to extract useful and reliable information from them regarding both the changes in the material microstructure as well as the degradation of the mechanical properties.

One of the main challenges in assessing the mechanical properties of the small shallow scoops in this study is that the conventional mechanical tests (e.g., compression or tension tests) are not viable due to the small volumes of material and scoop shapes extracted from operating turbine components. Each scoop specimen is irregular-shaped and measures about 20x20x5 mm (these are the largest dimensions in each of the three orthogonal sample directions). A schematic for mounted scoop samples in epoxy and its relative size difference with standard tension sample is shown in Figure 6. The small size and irregular geometry of the scoop make it difficult to fabricate specimens for conventional tests (e.g., compression or tension tests). However, the small scoop samples provide enough material volume for multiple indentation measurements and microstructure characterization without a significant compromise to the structural integrity of the turbine components.

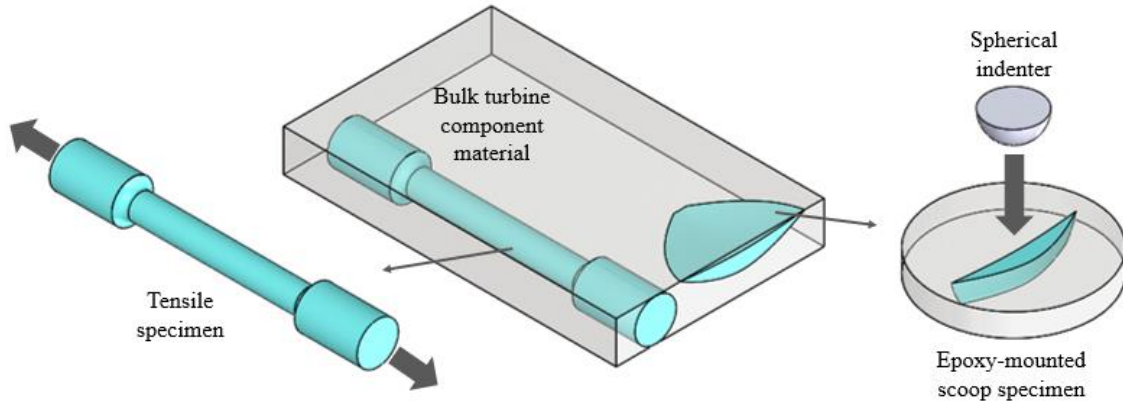


**Figure 6 – Schematic of mechanical test specimens extracted from turbine components and their relative sizes. Left side shows round tension test specimen. Right side shows epoxy-mounted scoop specimen (after scoop trimming and polishing).**

Each specimen was subjected to service temperatures in the range of 25 - 600 °C and operating service times in the range of 22,000 - 99,000 hours, as summarized in Table 1. In addition, a baseline material sample (no service exposure) is included in this study, totaling 8 samples with unique exposure conditions. The sample name indicates the service time in thousands of hours and the normalized service temperature code (note that baseline material is labelled as Unexposed).

**Table 1 – Specimens received for study with different exposure conditions. Superscript \* indicates samples where tensile test specimen were made in addition to microstructure and indentation measurements.**

Sample name	Approximate service hours
Unexposed*	0
22-0.98ST	22,000
49-0.78ST	49,000
55-0.79ST	55,000
71-0.80ST	71,000
91-0.85ST*	91,000
98-0.83ST	98,000
99-1.00ST	99,000

Before indentation test, each scoop specimen was ground on both sides to provide parallel surfaces. Furthermore, specimens were mounted in epoxy such that their top and bottom surfaces were both exposed (see Figure 6). This was done to provide maximum stability to the sample during the indentation test (i.e., prevent any unintended rotations of the sample). After mounting, the sample surfaces for indentation were ground and polished up to 0.02  $\mu\text{m}$  colloidal alumina suspension and vibropolished as the final step.

The two sample conditions, the Unexposed and the 91-0.85ST samples, evaluated using tensile tests revealed a significant decrease in yield strength (0.2% plastic strain offset), shown in Figure 7. The corresponding SEM-BSE micrographs show a considerable increase in graphite fraction in the 91-0.85ST microstructure compared to the Unexposed sample.

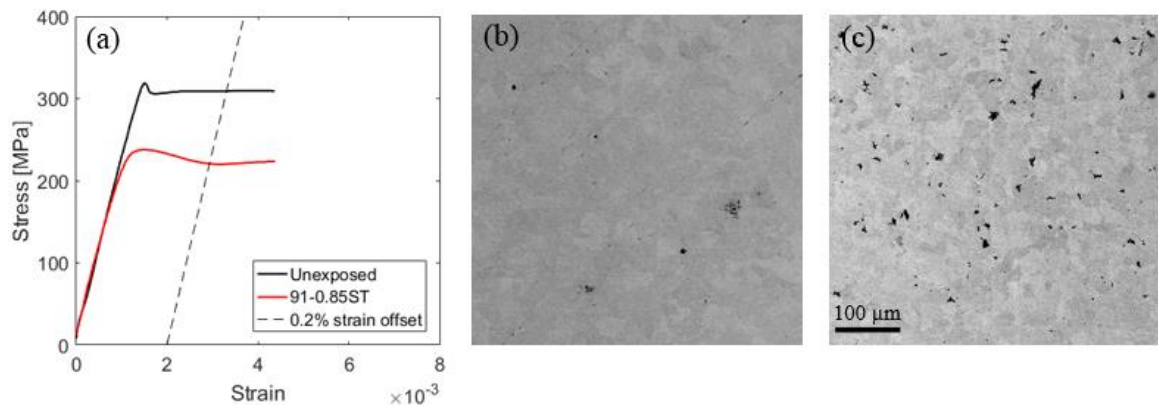


**Figure 7 – (a) Tensile stress-strain curves with 0.2% offset for the Unexposed and the 91-0.85ST specimens. Considerable reduction in yield strength is observed between Unexposed (average yield strength = 311 MPa), and after 91,000 service hours at 0.85ST (average yield strength = 221 MPa). (b) An example SEM-BSE micrograph for the Unexposed sample. (c) An example SEM-BSE micrograph for the 91-0.85ST sample (black particles are graphite).**

### 2.1.3.1 Scaling ISS curves to uniaxial stress-strain curves

Recent work [50, 61] has demonstrated correlations between indentation stress-strain measurements and those obtained in conventional tests such as simple compression or tension. In these comparisons one usually identifies a scaling factor between the stresses and strains involved in these curves. For example, the ratio of the flow stress in indentation to that in uniaxial compression is often referred as the constraint factor in literature [36, 38, 50, 60, 61, 83-85]. In recent numerical simulations using finite element (FE) models Patel and Kalidindi [50, 61] developed and demonstrated protocols for converting indentation stress and strain values to equivalent values in uniaxial compression stress states. This study extracted ISS curves consistent with the protocols used in this work and have suggested that the value of the constraint factor should be 2.2 for materials exhibiting isotropic plasticity based on  $J_2$  flow theory. This study also suggested specific scaling factors for elastic and plastic strains between the two test methods as 2.0 and 1.3, respectively [61]. It has been demonstrated that these scaling factors result in excellent agreement between the indentation and uniaxial compression stress-strain curves for a broad range of material hardening behaviors. Note that the uniaxial tests in the current study were performed in tension and we assume very little asymmetry between tensile and compressive behavior in the current steel samples. The use of FE models to systematically study such scaling relationships separates many of the difficulties and uncertainties that can arise in similar experimental investigations (e.g., non-ideal indenter or sample geometry, assumed elastic-plastic material behavior of sample and indenter, friction between the sample and indenter surfaces). In this study, we employ the proposed scaling

factors from the above FE study [61] to relate the current indentation stress-strain curves to the tensile stress-strain measurements.

Indentation stress-strain (ISS) measurements on samples where tensile tests were also performed serve to calibrate the indentation protocols described earlier. The average and one standard deviation of extracted modulus and yield strength measurements from indentation and tensile tests are shown in Table 2. Note that on average the sample elastic modulus,  $E_s$ , is slightly lower than the tensile modulus,  $E$ , for both samples, however, considering the spread in measurements (one standard deviation), there is overlap and reasonably good agreement between the two testing protocols. The yield strength ratio between the indentation and tensile tests ( $\frac{Y_{ind}}{Y}$ ) for both Unexposed and 91-0.85ST specimens was observed to be about 2. This value is in excellent agreement with corresponding values suggested by Patel and Kalidindi [61] and recent microindentation ISS measurements on Al-6061 [50].

**Table 2 – Measurements obtained from tensile and microindentation tests for Unexposed and 91-0.85ST samples. Note the higher variance in the indentation measured yield strengths.**

Sample name	Average tensile modulus, $E$ (GPa)	Average sample modulus, $E_s$ (GPa)	Average tensile yield strength, $Y$ (MPa)	Average indentation yield strength, $Y_{ind}$ (MPa)	Average yield strength ratio, $\frac{Y_{ind}}{Y}$
Unexposed	205 ±14.0	186 ±9.6	311 ±2.0	615 ±18.6	1.98
91-0.85ST	206 ±37.5	187 ±11.6	221 ±1.0	436 ±32.2	1.97

Using the three scaling factors suggested by Patel and Kalidindi [61], one can transform measurements on the indentation stress-strain curves to uniaxial stress-strain curves. Figure 8 shows the comparison between the scaled indentation measurements and

the tensile test measurements for the Unexposed samples, which display very good correlation between the two testing techniques.

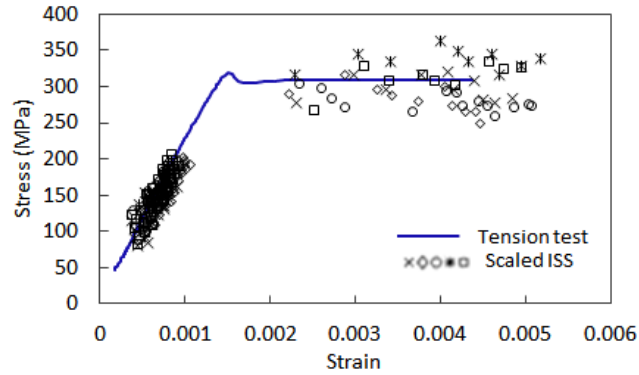


**Figure 8 – Tensile stress-strain curve and scaled indentation stress-strain data for Unexposed specimen.**

All of the scoop samples were evaluated using the indentation stress-strain protocols outlined earlier, totaling 77 indentation tests on 8 samples with distinct in-service exposure conditions. At least seven indentation measurements were conducted on each scoop sample. Figure 9 summarizes the uniaxial yield strengths extracted from these indentation measurements using the yield strength scaling above ( $Y_{ind}/2$ ) along with the tensile test results for two of the sample conditions.

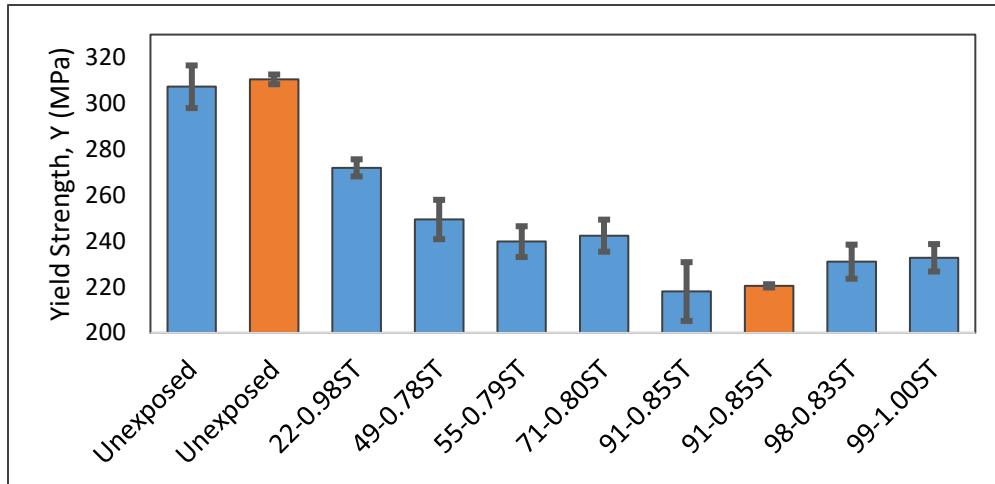


**Figure 9 – Summary of the measured tensile and scaled indentation yield strengths with error bars representing one standard deviation. A trend of changing yield strength with increasing service time is clearly discernible.**

The indentation measurements shown in Figure 9 reveal a trend of decreasing yield strength with increasing service time. It is also seen that the ISS protocols presented here are able to provide reliable measurements on small volume samples extracted from in-service gas turbine components. It is emphasized that there is no other practical alternative for extracting this critically needed information for the present study. It should be noted that the indentation results show a higher variability in yield strength measurements. Some of this variability reflects the inherent variation in the microstructure features (e.g., phase fractions, particles, inclusions) in the indentation zone.

## **CHAPTER 3.**

### **MICROSTRUCTURE IMAGE SEGMENTATION FRAMEWORK**

A major challenge in the study and microstructure quantification of heterogeneous materials comes from the need to label the features of interest (i.e., segment) in the raw microstructure images (two or three-dimensional) obtained in microscopy protocols used for evaluation of microstructure statistics. Often, the raw microscopy images are produced in grayscale, where each pixel (or voxel) is assigned a grayscale value between 0 and 255. However, the number of distinct features of interest (e.g., thermodynamic phases) present in the sample is typically far smaller than the number of grayscales in the raw images, as shown in Figure 10. This is because the pixel values of raw images reflect various types of noise arising from a combination of equipment or sample conditions in the imaging protocols. Therefore, segmentation protocols need to be designed to produce the correct labelling of the microscale features of interest in the microstructure images. This task is generally achieved by assembling together a workflow using a variety of image processing functions and filters [64-68]. One of the major hurdles encountered in this process is that the successful construction and implementation of the workflow leading to accurate segmentation is highly dependent on the user's expertise in the application of the image processing functions. Consequently, these efforts often lead to non-standard approaches that can strongly influence the accuracy of the microstructure analysis.

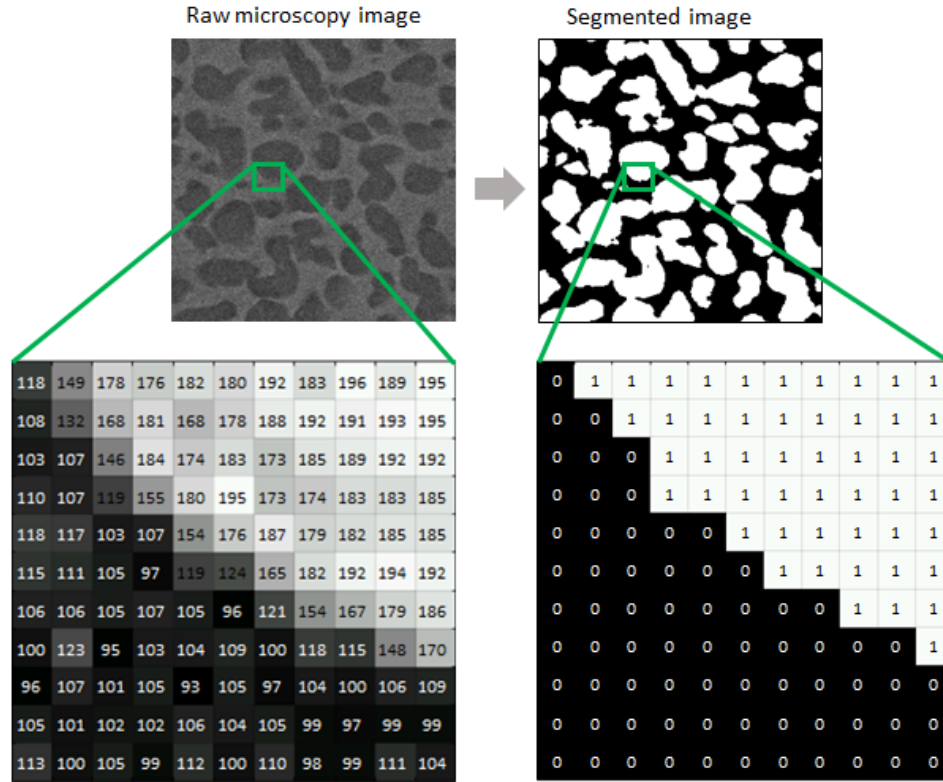


**Figure 10 – A schematic of an image segmentation example. Left side shows a raw microscopy image in grayscale with pixel values ranging between 0 and 255. Right side shows the segmented version of the raw with pixels values of only 0 or 1.**

In this dissertation, a framework is developed and demonstrated that reduces the dependence on user’s expertise in image processing to design workflows leading to consistent and reliable segmentation results. This approach for design of segmentation workflows consists of five sequential steps that systematically address common challenges encountered in segmentation of microstructure images. Each step provides users with guidance on selection and application of image processing functions best suited to resolve specific problems (e.g., pixel-level noise reduction, clean up incorrectly labelled features). This segmentation framework utilizes image processing functions that are widely available in popular software packages such as Python [86] and MATLAB [87], enabling potentially broad adoption by the material science community. This developed approach is described

next is demonstrated on a broad range of microstructures obtained from different microscopy techniques applied on different material systems.

### **3.1 Introduction**

Experimental microstructure characterization has been instrumental to the advancing of our understanding of the physics controlling the material response. Materials characterization techniques employ various forms of microscopy (e.g., optical microscopy, electron microscopy), which typically produce images of the material microstructure [65, 88-96]. Image segmentation is the process of labelling features of interest in microstructure images, and plays a key role in extracting reliable statistical information about the material microstructure [64, 66-68, 97-100]. However, raw microscopy images exhibit significant noise that can be attributed to multiple sample/equipment conditions. This noise usually hinders segmentation. The potential contributors to the image noise include improper sample preparation (e.g., surface roughness, surface residue), incorrect equipment use (e.g., focusing), and inadequate equipment capabilities (e.g., resolution limits) [64, 66, 68, 99, 101-105]. De-noising before actual segmentation of the images is an essential step to extract reliable statistical information about the material microstructure from the microscopy images [64, 66, 68, 99, 101]. Incorrect segmentation can influence strongly the quantification of microstructures, and lead to inaccurate understanding of the materials physics and formulation of erroneous physics-based composite models, including process-structure-property linkages (PSP) [56, 57, 106-109].

More specifically, segmentation in the application to material microstructures can be defined as a process of labelling each pixel (2D) or voxel (3D) with the elements of a

microstructure feature class that are also referred as local state descriptors. The local material state (at the level of a pixel or a voxel) is usually defined through a combination of multiple material attributes needed to uniquely identify the local properties of the material at the selected length scale (e.g., thermodynamic phase, grain of a specific orientation, grain boundary). For the example Ni-based superalloy micrograph shown in Figure 11b, the  $\gamma$  and  $\gamma'$  phases would serve as the local state descriptors. The central task in segmentation is the correct labelling of microstructural local states in microscopy images. Segmentation can be addressed using a wide range of image processing tools available in popular software packages such as Python [86] and MATLAB [87]. However, selecting and applying the appropriate tools in sequences designed to optimize the segmentation results can be a challenging task because of the large number of options in the available tools, algorithms, and approaches. The segmentation strategy can vary significantly depending on the image content (for example, prior reports on Ni-based superalloys [64, 67], steels [65, 66], and Ti alloys [68]). Typically, these strategies are tailored to produce best segmentation results for a specific material or for the specific imaging protocols employed in a study. Many of the main algorithms needed to design segmentation workflows are also accessible through materials-specific packages (e.g., Sosa et al. [110], EM/MPM [111], Campbell et al. [68]). However, the design of broadly applicable segmentation workflows following a systematic strategy continues to be an open challenge for many material science practitioners.

Current approaches employed in material image segmentation largely depend on the user's expertise and knowledge of available functions in the popular packages mentioned earlier. Since many factors can affect the segmentation process (e.g., image noise, features

of interest, available tools), the segmentation results are likely to vary significantly between different users. This dramatically impacts our ability to aggregate replicable and reproducible materials knowledge needed to objectively guide materials innovation efforts. Clearly, there is a critical need for a unified framework for addressing segmentation in a more consistent manner that could be broadly adopted by the materials researchers. In this work, one such framework is presented, and its flexibility and versatility in successfully segmenting a variety of microstructures obtained from very different material systems is demonstrated. The proposed framework comprises five sequential steps, with multiple options for each step. The first step addresses best practices in sample preparation, selection and set-up of the image acquisition equipment, and image collection protocols. The second step focuses on image preprocessing for the adjustment and enhancement of the acquired image in order to get it ready for segmentation. The third step then employs various algorithms for labelling each pixel in the image to an expected local state using segmentation algorithms. The fourth step is designed to post-process the segmented results to improve the segmentation results. The final step focuses on evaluation and validation of the segmented images. The five steps described above become the main components in the systematic design of the proposed microstructure segmentation workflow. The central considerations and the selection criterion for the available options for each of these components are discussed in each step of the framework. Case studies illustrating the application of various tools and whole workflows designed using the proposed framework are presented throughout the next sections.

### 3.2 Challenges in segmentation

As already mentioned, the goal of segmentation is to label each pixel with the correct microstructure local state. The application of a single segmentation algorithm on an image of the material structure is, in most cases, unlikely to produce the desired final segmented images. This is largely because the image noise is often highly heterogeneous even in a single image and can be present as global or local noise. Global noise refers to noise at an image-level, for instance, an intensity gradient of the image producing a shadow effect. On the other hand, local noise is undesired variation in intensity at a pixel-level and is usually scattered randomly throughout the image. Examples of the challenges encountered in segmentation are illustrated in Figure 11 through selected micrographs, where the top row shows the micrographs and the bottom row shows their segmented versions obtained using thresholding-based tools employed broadly in current literature [112-114]. Figure 11a shows a SEM (scanning electron microscope) micrograph obtained from a Ni-based superalloy sample with  $\gamma$  and  $\gamma'$  local states. Clearly, the two local states are visually discernable, but the lack of contrast between them leads to poor segmentation results. More specifically, the lack of a smooth contrast often results in pixel-level noise in the segmented images. This is significantly amplified in the segmentation of the micrograph in Figure 11b. In spite of the clear intensity difference between the two phases in this micrograph, the commonly used thresholding approach is unable to remove the pixel-level noise in the image. This is because the local pixel-level fluctuations in the image occur on both sides of the selected intensity threshold. Microscopy images may exhibit a global shadow with a gradient in its intensity over the image (e.g., caused by non-uniform illumination of the sample surface) as shown in Figure 11c, which can also cause a significant challenge in

segmentation. Removal of this type of global noise requires a completely different strategy compared to the removal of the pixel-level noise.

Multiple algorithms and strategies have already been discussed in literature for addressing the challenges identified above. For example, Gaussian filtering [68, 101, 115] is often employed to remove the pixel-level noise in the microstructure images. However, there is often no guidance for optimal filtering that achieves noise removal while not losing the important details in the microstructure image. Similarly, various image enhancement techniques [116, 117] can be utilized to increase the contrast between features to improve segmentation. The selection of the best segmentation algorithm for a given micrograph depends on the specific microstructure features being labelled. Microstructure features encountered in materials studies can be broadly classified as either regions or interfaces. Regions refer to contiguous areas (volumes in 3-D) of selected microstructure local states usually represented as foreground objects in the image (e.g., precipitates, embedded thermodynamic phases). Interfaces refer to boundaries separating the microstructure local states, and can include a variety of grain/phase boundaries. The features represented as regions cover a vast space of multiphase microstructures, as shown in Figure 11a-d, and will be the main focus of the work and examples described here.

It is likely that most segmentation algorithms will produce results that still contain some noise or inaccuracy. Some form of post-processing is generally required to clean up the incorrect results. Examples of these challenges, referred as undersegmentation and oversegmentation, are shown in

Figure 11a and Figure 11d, respectively. In other cases, post-processing using various morphological operations is desired for cleaning up incorrect results. The diverse challenges encountered in segmentation outlined above further reinforce the need for a systematic framework for the design of segmentation workflows.

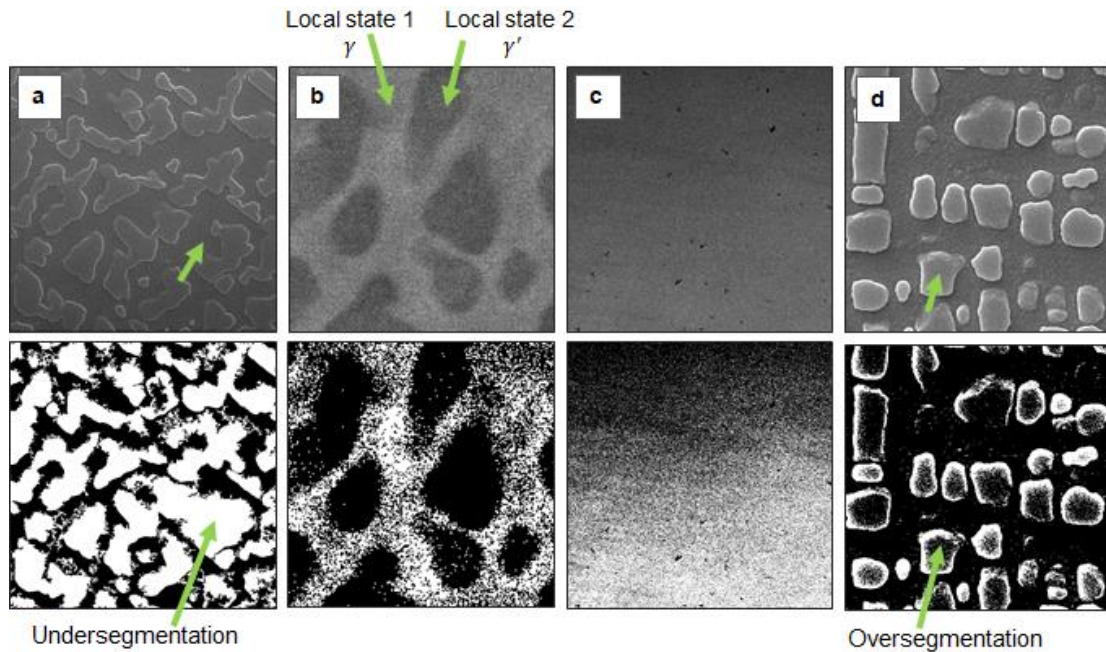


**Figure 11 – Examples of challenges encountered in the segmentation of feature regions in micrographs: a) Ni-based superalloy microstructure image showing clear features but of low contrast resulting in poor segmentation (see regions near the arrows in the top and bottom images), b) segmentation of an image with pixel-level noise, c) segmentation of image with global shadow gradient in its intensity, d) image with oversegmentation that requires post-processing (see regions near the arrows in the top and bottom images).**

### 3.3 Segmentation framework

We develop a systematic and versatile segmentation framework consisting of five sequential steps that are designed to address the challenges identified in the previous section, while being broadly applicable to a variety of microscopy images. These five steps will be referred as acquisition, preprocessing, segmentation, post-processing, and

validation, and are summarized in Table 3. These steps are specifically designed to produce consistent, reproducible, and reliable quantification of microstructure images. We describe next each of these steps in detail, and identify the relevant functions in MATLAB [87] and Python [86] environments that could help address the tasks involved in each step. The hierarchy of actions in each step in the suggested framework is the following: step  $\rightarrow$  task  $\rightarrow$  subtask  $\rightarrow$  option. The task and subtasks identify the main objectives addressed in each step, and the options provide available methods to accomplish these objectives.

**Table 3 – Summary of the five steps of the segmentation framework developed in this work. Within each step, tasks and subtasks are specified. Examples of available methods to be considered for addressing each subtask are also specified.**

1. Acquisition	2. Preprocessing	3. Segmentation	4. Post-processing	5. Validation
Setup experiments for microstructure image acquisition  <b>Task 1: Sample imaging parameters selection</b> <ul style="list-style-type: none"> <li>● Subtask 1: Feature spatial resolution selection</li> <li>● Subtask 2: Representative microstructure view field selection</li> </ul>	Preprocess acquired images for improved segmentation  <b>Task 1: Image noise reduction</b> <ul style="list-style-type: none"> <li>● Subtask 1: Spatial pattern noise reduction</li> <li>□ Intensity gradient reduction</li> <li>□ Frequency domain filter</li> <li>● Subtask 2: Random noise reduction</li> <li>□ Gaussian filter</li> <li>□ Bilateral filter</li> <li>□ Median filter</li> </ul> <b>Task 2: Contrast enhancement</b> <ul style="list-style-type: none"> <li>□ Histogram stretching</li> <li>□ Histogram equalization</li> <li>□ Local contrast enhancement</li> <li>□ Unsharp masking</li> </ul>	Segment image features into local states of interest  <b>Task 1: Local state region segmentation</b> <ul style="list-style-type: none"> <li>□ Thresholding</li> <li>□ Edge detection</li> </ul> <b>Task 2: Local state interface segmentation</b> <ul style="list-style-type: none"> <li>□ Edge detection</li> <li>□ Watershed segmentation</li> <li>□ Region growing</li> </ul>	Postprocess segmented images for desired results  <b>Task 1: Adjust segmentation results</b> <ul style="list-style-type: none"> <li>● Subtask 1: Morphological operations</li> <li>□ Dilatation/erosion</li> <li>□ Closing/opening</li> <li>● Subtask 2: Clean up segmented results</li> <li>□ Binary shape analysis and clean up</li> </ul>	Objectively validate segmentation results  <b>Task 1: Qualitative validation</b> <ul style="list-style-type: none"> <li>□ Visual inspection evaluation</li> </ul> <b>Task 2: Quantitative validation</b> <ul style="list-style-type: none"> <li>□ Volume fraction</li> <li>□ Grain size distributions</li> <li>□ Standard reported values</li> <li>□ Higher-order microstructure statistics</li> </ul>

Legend
<b>Step</b>
<b>Task</b>
● Subtask
□ Option

### 3.3.1 *Image acquisition*

The first step in designing the segmentation framework should pay attention to the details of the image acquisition, and wherever possible adjust the image acquisition parameters. Although this might come across as a trivial step, it often has the largest impact on the accuracy and utility of the segmentation results. This task consists of two main subtasks that can usually be adjusted across different types of microscopy techniques: (i) selecting a feature spatial resolution (i.e., setting the pixel or voxel size in the acquired image), and (ii) selecting a representative microstructure view field size (i.e., the image size). Although there are a number of other image acquisition parameters that can influence the subsequent processing of acquired images for segmentation, the vast number of possible tuning parameters depends on the microscopy technique and user's expertise. Selecting optimal acquisition parameters is also dependent on study-specific factors (e.g., sample preparation, equipment type, user's expertise).

Several microscopy techniques are commonly employed to capture the details of the material structure [65, 118-121], which spans a hierarchy of length scales ranging from  $10^{-3}$  to  $10^{-10}$  m. The widely used microscopy techniques include optical microscopy, electron microscopy, scanning probe microscopy (e.g., atomic force microscope), x-ray (e.g., micro computed tomography), among others. The images obtained by these different techniques often reveal different types of information about the material internal structure as they are produced as a consequence of different types of interactions with the sample. Optical microscopes detect sample topology through reflected light from the sample surface. Commercial optical microscopes require simple operation but are often limited in spatial resolution to about  $1 \mu\text{m}$ . However, recent advances in super-resolution optical

microscopy have pushed the capabilities to sub-micron resolution [122]. Higher resolution can be obtained using the scanning electron microscope (SEM), which utilizes an electron beam to probe and image the sample. Most common image modes are secondary electron (SE) and back scatter electron (BSE). SE is typically employed for topographic survey, whereas BSE is employed for both compositional and topographic survey [102]. Scanning probe microscopy (SPM) is another popular technique for topological surveying with reported sub-nanometer resolution [123]. The SPM imaging is performed by scanning the sample surface with a physical probe to record the sample topology. SPM is capable of high-resolution imaging without requiring a vacuum environment, but is limited by the smaller scan size and a slower scan speed (compared to SEM) [124]. Other types of microscopy include x-ray methods such as micro computed tomography (micro-CT). The rendered pixel intensity in micro-CT images corresponds to the radiodensity (relative inability of electromagnetic radiation to pass through a material) in the sample. Micro-CT allows non-destructive 3-dimensional scanning of the material structure. On the other hand, micro-CT data are limited in spatial resolution compared to SEM and may exhibit low contrast between local material states of similar densities.

Given the variety of available techniques, it is important to select the technique that provides the most contrast for the features of interest. As an example, Figure 12a shows two SEM images of the same sample location showing graphite particles (darker colored regions) in steel matrix (light background) using BSE and SE detectors. It is evident that SEM-BSE detector captured a foreign inclusion (shown with arrow) which appears dark and difficult to distinguish from graphite, whereas SE detector is able to clearly distinguish the inclusion based on topology difference with the ferrite matrix. Furthermore, it should

be noted that sample preparation steps (e.g., polishing, etching) can control the quality of the acquired images. As an example, Figure 12b demonstrates imaging results from the same Ni-based superalloy sample with different etching and SEM detectors. Notice that multiple precipitate edge segments of the SEM-SE image in Figure 12b exhibit low contrast due to shadowing effect (not directly in sight of SE detector), which will make segmentation more challenging. Previous studies improved areas of weak contrast due to shadowing by combining several images from orthogonal acquisition angles to expose edges previously in the shadow of SE detector [64]. In many cases, there may be a strong reciprocity between the experimental data acquisition approach and the subsequent effort in processing for segmentation. In general, users should attempt to collect microstructure data in a manner such that the required processing of the images for segmentation is minimized.

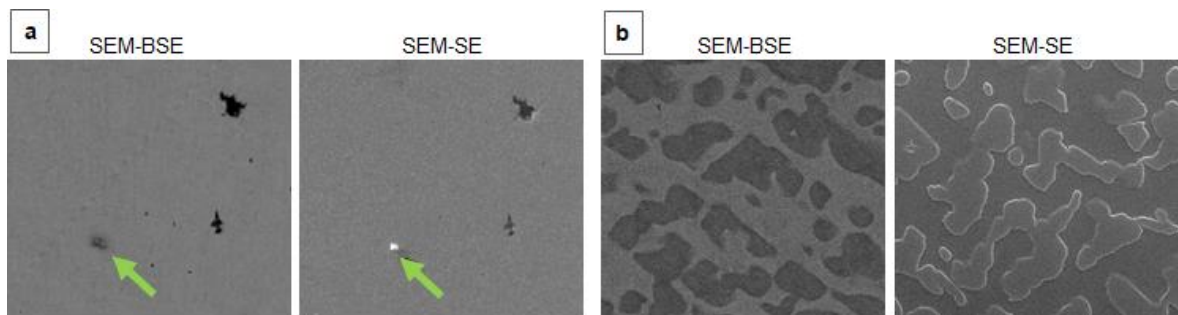


**Figure 12 – a) SEM images of the same location in steel microstructure using BSE detector (left) and SE detector (right). Foreign inclusion shows as a dark feature similar to graphite (darker colored regions) in SEM-BSE image, whereas it is clearly distinguishable in SEM-SE image on right. b) SEM images of the same Ni-based superalloy sample using BSE detector (left) and SE detector (right). The combination of etched  $\gamma'$  precipitates and SEM-BSE imaging (left) yields better contrast between  $\gamma$  and  $\gamma'$ , compared to etched  $\gamma$  matrix and SEM-SE imaging (right) .**

### 3.3.1.1 Sample imaging parameter selection

The first subtask of image acquisition is to select an adequate feature spatial resolution by adjusting the image pixel size. Pixel size is the physical length represented by a pixel in the image [103]. Here, we refer to feature spatial resolution as the number of pixels that represent the smallest feature of interest in the image. Higher resolution represents a feature with greater number of pixels compared to lower resolution. Users should select a spatial resolution such that the smallest microstructure features of interest are adequately detailed in the final segmented image. Since digital images represent pixelated versions of the actual features, the level of detail lost due to pixelization increases with decreasing resolution. We illustrate the effect of feature spatial resolutions using two micrographs of Ti-811 alloy from the same location in a sample, but one with a high resolution (Figure 13a), and the other with a low resolution (Figure 13b). It is clear that some of the smaller scale features are essentially lost in the low resolution image. Note that the ability to distinguish and accurately capture the feature shape is better in the higher resolution image, which will also result in a more accurate segmentation and quantification. The resolution is inherently limited by the equipment hardware, and will not likely provide a better detail if resolution is increased artificially (e.g., using interpolation to magnify features). The magnification and image acquisition controls may often be fixed or are only adjustable in large discrete steps, both of which limit our ability to get a high quality image from the equipment.

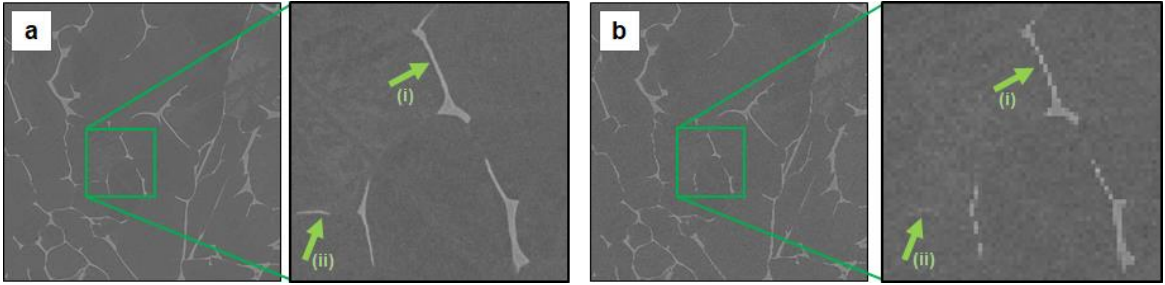


**Figure 13 – Images of a  $50\ \mu\text{m} \times 50\ \mu\text{m}$  area taken with different spatial resolutions: a) higher spatial resolution image ( $0.05\ \mu\text{m}/\text{px}$ ), and b) lower spatial resolution image ( $0.2\ \mu\text{m}/\text{px}$ ). Note the lower fidelity of the feature detail in (i) and nearly indistinguishable small feature in (ii) in the lower resolution image.**

The second subtask of imaging parameter selection is to set a view field that captures representative information about the microstructure features of interest. The view field is the area of the sample microstructure captured by an image. For example, the image in Figure 13a captures a  $50\ \mu\text{m} \times 50\ \mu\text{m}$  area. Ideally, one would determine the view field size using a formal framework for the statistical quantification of the microstructure features. As an example, one might define a view field using the coherence length computed from 2-point spatial correlations [125]. Coherence length is defined as the length beyond which the 2-point statistics of microstructure features are mostly uncorrelated [126]. Since the coherence length can only be ascertained after getting reliable segmented images, this approach would likely require some iterations before finalizing the view field size. Another approach would be to increase the window size until one gets robust measures of the desired microstructure statistics. For example, if one wishes to capture the precipitate volume fractions, one would systematically increase the scan size until the estimated value of volume fraction demonstrates insensitivity to scan size (i.e., the extracted values of the microstructure statistics lie within acceptable tolerance limits). Finally, it is also important

to obtain images from multiple locations in the sample so that one can document location to location variance in the microstructure statistics within a given sample. Moreover, acquiring multiple representative images from random sample locations will most likely result in better statistical representation of the microstructure, compared to one large view field image in a single location [125, 126].

It is important to note that a tradeoff between optimal spatial resolution (to resolve small features) and optimal view field size (to capture statistically representative features) may be required. This is because increasing spatial resolution requires microscopes to scan a smaller area/volume, which in many cases reduces the speed of imaging the desired view field size. To achieve desired spatial resolution over a large view field, image montage is often utilized, where high spatial resolution images can be efficiently stitched together [127, 128].

### *3.3.2 Image preprocessing for segmentation*

Image preprocessing should be performed to prepare the acquired image for subsequent segmentation. The main goals of preprocessing are image noise reduction and feature contrast enhancement. The first task focuses on removing as much of the undesired intensity variation (i.e., noise) in the image as possible, and can be further divided into two subtasks: (i) reduction of global noise, and (ii) reduction of local noise. As mentioned earlier, global noise refers to the image noise at an image-level, for instance, an intensity gradient of the image producing a shadow effect (Figure 11c). On the other hand, local noise is on a pixel-level and is usually scattered randomly throughout the image (see the segmented example with local noise in Figure 11b). After noise reduction, the second

preprocessing task is to perform contrast enhancement of microstructure features to prepare the image for segmentation.

### 3.3.2.1 Image noise reduction

We first focus on reducing the global noise, which is usually an artifact of image acquisition equipment setup or protocols (e.g., shadow across image). Global noise that is smoothly varying over the image can be efficiently reduced by subtracting the approximated global noise from the noisy image. Here, we demonstrate a readily accessible approach for fitting a polynomial function to approximate the global noise from the image [129]. Let  $I(i, j)$  with  $i = 1, \dots, m$  and  $j = 1, \dots, n$  denote the intensities in a 2D grayscale image. Further,  $I(i, j)$  is only allowed to take integer values in the range  $[0, 255]$ . The global noise is assumed to be adequately presented by a polynomial function  $f(i, j; \mathbf{B})$ , where  $\mathbf{B} = \{b_0, \dots, b_k\}$  denote the fitting parameters in the function. As an example, for a second-order polynomial, this implies  $f(i, j; \mathbf{B}) = b_0 + b_1i + b_2j + b_3i^2 + b_4j^2 + b_5ij$ . Standard least-squares regression is utilized to find the fitting parameters  $\mathbf{B}$ . If one has a large image, it might be computationally efficient to perform the regression on a uniformly selected subset of pixels in the image. The corrected image is obtained by simply subtracting the fitted noised function from the image as  $I_R = I - f$ . One consequence of this correction is that the intensity values of the corrected image are no longer in the original range  $[0, 255]$  and need to be rescaled. Figure 14 demonstrates the application of the above algorithm on an example image using a second-order global noise function. Another popular method is based on optimizing the parameters in estimating the global noise that minimizes the entropy of the corrected image [130]. In instances where a montage of

images is constructed, the above noise-reduction methods may be applied to individual images or the image montage.

The global noise reduction approach described above is limited to images with smooth global intensity variations over the image, which are frequently attributed to image acquisition conditions. These approaches may not be effective if multiple global noise sources are present, for example, noise due to sample topology, markings, defects, etc. Often, unwanted noise that exhibits a distinct spatial pattern can be reduced using Fast Fourier Transform (FFT) filtering techniques [110, 114]. Since FFT filtering operates in the frequency domain of the image, periodic noise can be reduced by suppressing frequencies that contain the noise patterns. This technique is frequently implemented in image processing, and can be adapted to reducing unwanted rings or other artifacts on the sample surface (e.g., induced in ion milling) [110].

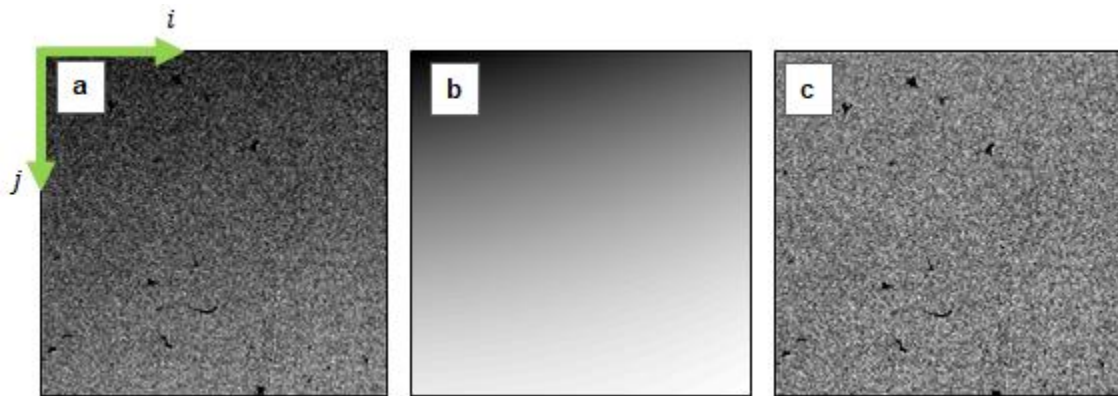


**Figure 14 – Example of intensity gradient noise reduction from an SEM image: a) input image  $I$  with intensity gradient, b) approximated intensity gradient  $f$ , and c) corrected image  $I_R$ .**

The second subtask in noise reduction is the mitigation of the local noise that is randomly scattered throughout the image. Reduction of this noise using filters is a topic of

high interest in image processing field with many proposed algorithms [131-134]. However, determining the optimal strength of these filters can be a significant challenge, since excessive filtering may remove valuable image detail while under-filtering may leave noise in the image. Our goal is therefore to eliminate the random noise while minimizing the loss of feature details. Let the input image be denoted by  $I$ , the filtered final image by  $I_F$ , and the difference between the input and filtered images by  $R = I - I_F$ . In other words,  $R$  denotes the local noise removed. Analysis of  $R$  can provide important guidance for the selection of the filters used in this subtask. In this work, we propose a novel approach for optimal selection of the strength of local noise reduction filter.

Let us consider the use of a Gaussian filter kernel,  $G_\sigma$ , which when applied to the noisy image, results in the filtered image  $I_F$ . Mathematically, this transformation can be expressed as

$$I_F = I * G_\sigma \quad (15)$$

$$G_\sigma(i, j) = \frac{1}{2\pi\sigma^2} \exp\left(-\frac{i^2+j^2}{2\sigma^2}\right)$$

where  $\sigma$  is the standard deviation (in pixels), and determines the strength of the Gaussian filtering applied to the image. Larger values of  $\sigma$  correspond to stronger filtering. One can then evaluate the similarity between the residual  $R$  and the filtered image  $I_F$  as

$$p = \frac{|R \cdot I_F|}{|I_F|} \quad (16)$$

where the dot in the numerator implies a full inner product. The value of  $p$  obtained from Eq. (16) should be expected to vary with the value of  $\sigma$ . We propose that one should identify the value of  $\sigma$  corresponding to the lowest value of  $p$  (i.e., lowest similarity between  $R$  and  $I_F$ ) and use it in the Gaussian filtering of the image for effective removal of the local noise in the image. The proposed approach is demonstrated in Figure 15 with an example image. In this figure, the images in columns (c) and (d) correspond to the lowest correlation of the residual  $R$  (top row images) and the filtered image  $I_F$  (middle row images). For convenience, the segmented images obtained by thresholding the filtered images are shown in the bottom row of Figure 15. Note the amount of image detail in the residual increases with increasing  $\sigma$ . However, with the optimal level of noise reduction, we can strike a balance between removed noise and retained detail for further segmentation.

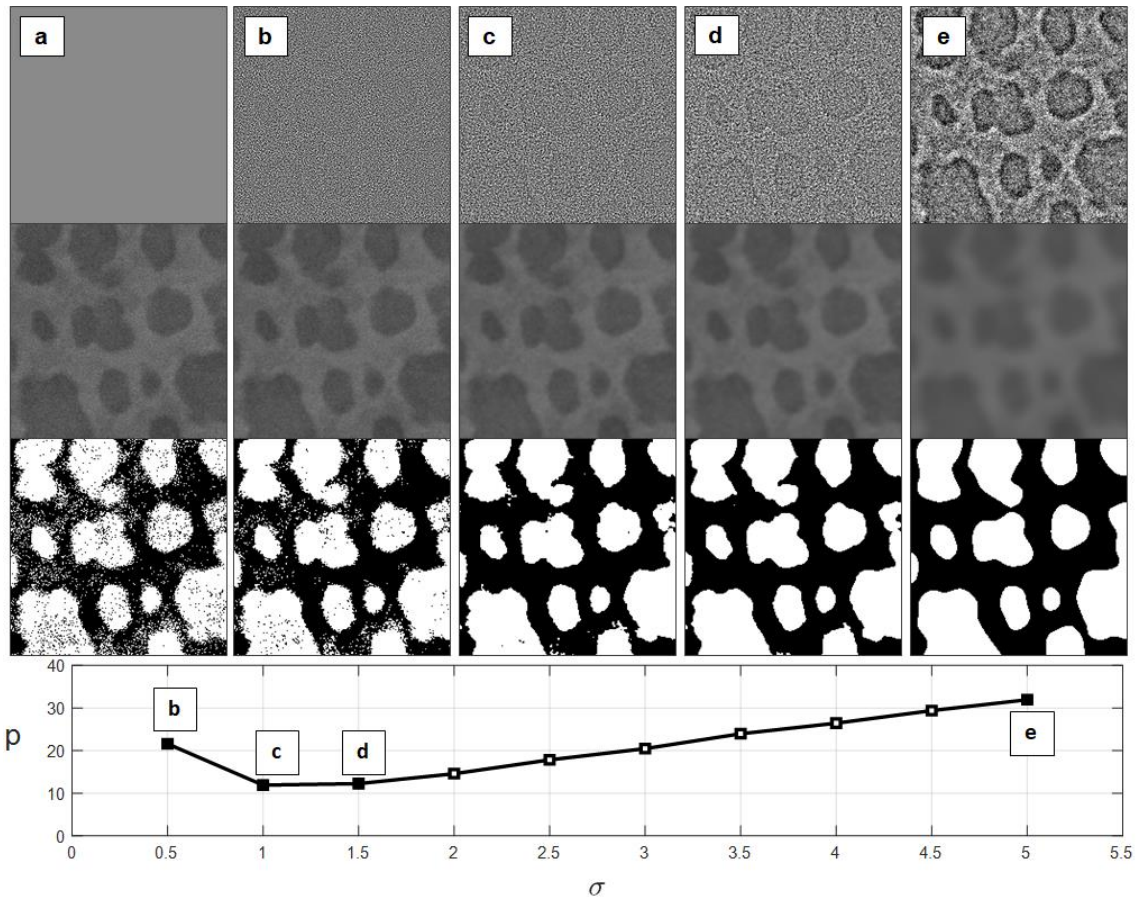


**Figure 15 – Random noise reduction using Gaussian filtering on input image in the middle row of a). Top row shows the removed noise,  $R$ , corresponding to different filter strengths. The middle row shows the associated filtered images  $I_F$ , and the bottom row shows segmented versions of the filtered images obtained by using simple thresholding. Higher values of  $\sigma$  results in loss of image detail, while lower values leave some of the local noise in the image. Optimal filtering is close to image c), between  $\sigma = 1$  and  $\sigma = 1.5$ .**

Other popular options for noise reduction methods include the bilateral filter [135] and median filter [136], listed in Table 4, along with other options in MATLAB [87] and Python [86]. Bilateral filter improves on the Gaussian filter described above by accounting for the sharp intensity transitions by incorporating a kernel that weighs effect of surrounding pixel intensities. In other words, bilateral filter tends to reduce the blurring of feature edges. The median filter computes the median intensity values in a small window (e.g.,  $5 \times 5$  kernel) in the image and assigns the median value to the center pixel of the

window. This method works well for adjusting pixels with unreasonably high levels of noise (e.g., salt-and-pepper noise) while also reducing the loss of feature edge details [114, 137].

Approaches mentioned so far (Gaussian, bilateral, median filters) modify the pixels based on their immediate surrounding neighborhood information and are usually called pixel-based filtering. Another popular approach to noise reduction is patch-based filtering [138]. Patch-based filters modify pixels within a patch (neighborhood of pixels) based on information in other patches of the same size within the noisy image. A popular patch-based method is non-local means (NLM) approach [139], listed in Table 4. Non-local means utilizes similarity (in intensity and distance) between a pixel's reference patch to other non-local patches in the image to determine the amount of noise reduction in the reference patch. This enables pixels that are far apart but with similar patches to be averaged together for noise reduction. Patch-based filters preserve feature edges while smoothing homogeneous regions. Advances in image processing field offer various other approaches of noise reduction using patch-based filtering [140-143], including an extension of non-local means filtering which treats the patch similarity measures in a statistical framework [144].

**Table 4 – Functions available for image noise reduction in MATLAB [87] and Python scikit-image [145].**

Method	MATLAB	scikit-image
Gaussian filter	<code>imgaussfilt</code>	<code>filters.gaussian</code>
Bilateral filter	<code>imbilatfilt</code>	<code>restoration.denoise_bilateral</code>
Median filter	<code>medfilt2</code>	<code>filters.median</code>
Non-local means filter	<code>imnlfilt</code>	<code>restoration.denoise_nl_means</code>

### 3.3.2.2 Contrast enhancement

The second task in the preprocessing step is contrast enhancement of the microstructural features of interest, and is aimed at preparing the image for the subsequent segmentation. Unlike conventional image processing used to enhance the perceived visual quality of the image [146], the goal here is to increase the contrast of features of interest to improve the segmentation results in the next step. The options for contrast enhancement discussed here fall into two categories: global methods and local methods. Global methods modify the whole image at once and do not consider the spatial relationship of the pixels (i.e., adjacent pixels do not affect each other more than pixels separated by some distance). Global transformations can be conveniently performed by adjusting the image histogram to achieve contrast enhancement. On the other hand, local methods account for both intensity and spatial context in the image while trying to improve the contrast in the image.

Popular global contrast enhancement methods are contrast stretching and histogram equalization [147]. Contrast stretching is performed in two steps: stretching the input image histogram range  $[r_{min}, r_{max}]$  to a wider range  $[r'_{min}, r'_{max}]$ , and saturating (i.e., absorbing a range of intensities into a narrower range) a specified percentage of bottom and top intensities of the new histogram range. The wider histogram range achieves higher contrast

by increasing the intensity differences between pixels. As an example, Figure 16a shows a SEM micrograph from a steel sample with a fairly narrow range of intensities,  $[r_{min} = 14, r_{max} = 94]$ . Figure 16b shows contrast stretching of the original image Figure 16a to the full range of the histogram  $[r'_{min} = 0, r'_{max} = 255]$ , and saturation of the top and bottom 1% intensities. In other words, the bottom 1% of original histogram intensities become 0 and the top 1% become 255. The amount of stretching controls the intensity range and amount of saturation adjusts the spread of intensities at the extremes of the new histogram range. Figure 16c shows less histogram stretching to  $[r'_{min} = 27, r'_{max} = 129]$ , and the top 15% of histogram intensities have been saturated to the maximum value  $r'_{max} = 129$ . Saturation of the top 15% intensity pixels artificially removes the higher intensity values, as shown in Figure 16c. The second contrast enhancement option is histogram equalization, which transforms the input image histogram to approximately match a target histogram (e.g., flat histogram). In the case of a flat target histogram, this method redistributes the input histogram peaks over a wider intensity range thus creating higher contrast, as shown in Figure 16d. Note that the global contrast enhancement does not account for differences in the image content in different areas of the image. For instance, it is evident that homogenous parts of the image in Figure 16b-d do not benefit from contrast enhancement due to visible amplification of noise.

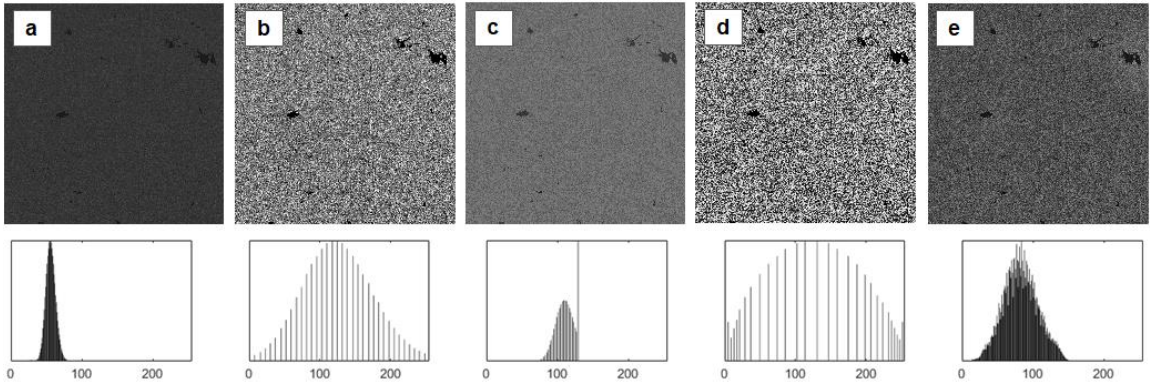


**Figure 16 – Examples of global and local contrast enhancement: a) input image with low contrast, b) contrast stretching with bottom and top 1% intensity saturation, c) bottom 0% and top 15% saturation, d) global histogram equalization, e) contrast-limited adaptive histogram equalization (CLAHE).**

To improve on the global histogram equalization, one can employ a local contrast enhancement approach such as the contrast-limited adaptive histogram equalization (CLAHE) [117]. CLAHE performs histogram equalization on subregions of the image, while limiting the amount of contrast enhancement in homogenous regions. As a result, one of the benefits of CLAHE is that undesired noise amplification of homogeneous areas of the image is reduced as compared to global methods, shown in Figure 16e. Another local contrast enhancement is the unsharp masking [147], which is an image filtering method. Image filtering, unlike histogram adjustments (modifying the whole image or a portion of the image at once), modifies one pixel at a time based on the neighborhood information and can be effectively used to enhance specific image features. For instance, contrast of weak edges may be improved with local contrast enhancement. Unsharp masking utilizes a sequence of filtering steps to increase the contrast of the input image. The unsharp algorithm is controlled by several filtering settings, such as the size of filter neighborhood, the threshold of filtering application, and the extent of image adjustment. Users should attempt to modify the input image to improve the segmentation results in the next step. As

an example, for the image in Figure 17a, the unsharp masking was utilized to produce increase in edge contrast, as shown in Figure 17b. Although the visual quality of the image may not improve, this subtask is only concerned with improving the contrast of the features of interest. Some of the popular contrast enhancement functions in MATLAB [87] and Python scikit-learn library [145] are listed in Table 5.

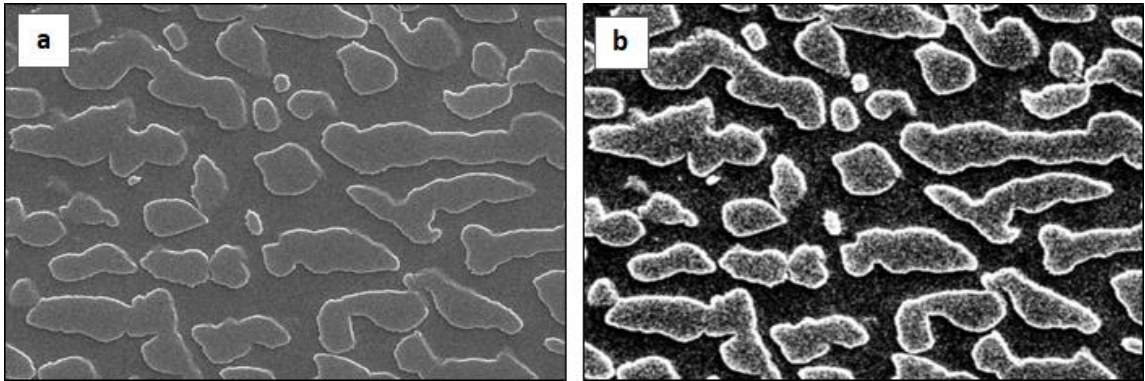


**Figure 17 – a) Input image and b) modified image using unsharp filtering. Note that the contrast is increased around feature edges, but the visual appearance is not necessarily enhanced.**

**Table 5 – Functions available for image contrast enhancement in MATLAB [87] and Python scikit-image [145].**

Method	MATLAB	scikit-image
Contrast stretching	<code>imadjust</code>	<code>exposure.rescale_intensity</code>
Histogram equalization	<code>histeq</code>	<code>exposure.equalize_hist</code>
CLAHE	<code>adapthisteq</code>	<code>exposure.equalize_adapthist</code>
Unsharp masking	<code>imsharpen</code>	<code>filters.unsharp_mask</code>

### 3.3.3 Segmentation

The main goal of the segmentation step is to label pixels based on the microstructure features that can be identified confidently in the given image. The tasks in segmentation are conveniently divided into two tasks focused on the segmentation of microstructure feature regions and interfaces, respectively. Although many different segmentation approaches are being explored in current literature [66, 97, 148-152], the focus in this work will be on methods that exhibit potential for broad application to a large variety of microstructure images. Several examples of the functions of interest to this step are listed in Table 6. It is important to note that multiple segmentation cycles may be required to achieve the desired results. For example, images where both local state regions and interfaces are present may require several methods be applied separately, and the results combined suitably.

**Table 6 – Functions available for image segmentation in MATLAB [87] and Python scikit-image [145].**

Method	MATLAB	scikit-image
Global threshold	<code>imbinarize</code>	<code>filters.threshold_otsu</code>
Local threshold	<code>imbinarize</code>	<code>filters.threshold_local</code>
Edge detection	<code>edge</code>	<code>filters.sobel*</code> <code>feature.canny*</code>

\*these represent examples of edge-detection algorithms in scikit-image among many alternatives

#### 3.3.3.1 Segmentation of regions

Regions are typically represented as spatial patterns of connected pixels with similar intensity values. The approaches for the segmentation of these regions mainly

utilize thresholding based on intensity values. This is illustrated in Figure 18a and Figure 18c using an example dual-phase microstructure in a TiMn sample. More generally, global threshold algorithms segment the entire image at once by defining  $k$  intensity thresholds, which classify the input image into  $k + 1$  classes. Thresholding algorithms commonly utilize various histogram properties to define the thresholds. Popular histogram thresholding algorithms currently used include the Otsu method [112], entropy thresholding [153], Gaussian mixture model [154], and k-means clustering [155]. The attractive aspect of thresholding is that these methods are automated and generally require simple inputs (e.g., number of feature classes). Furthermore, local adaptive thresholding algorithms improve on global methods by thresholding based on the pixel's neighborhood information (image details around each pixel) or thresholding smaller sub-images within the entire input image [113, 114]. Adaptive algorithms dynamically vary the threshold, and can perform better than global thresholding in cases where undesired local intensity variation (e.g., noise) is present in the image [114].

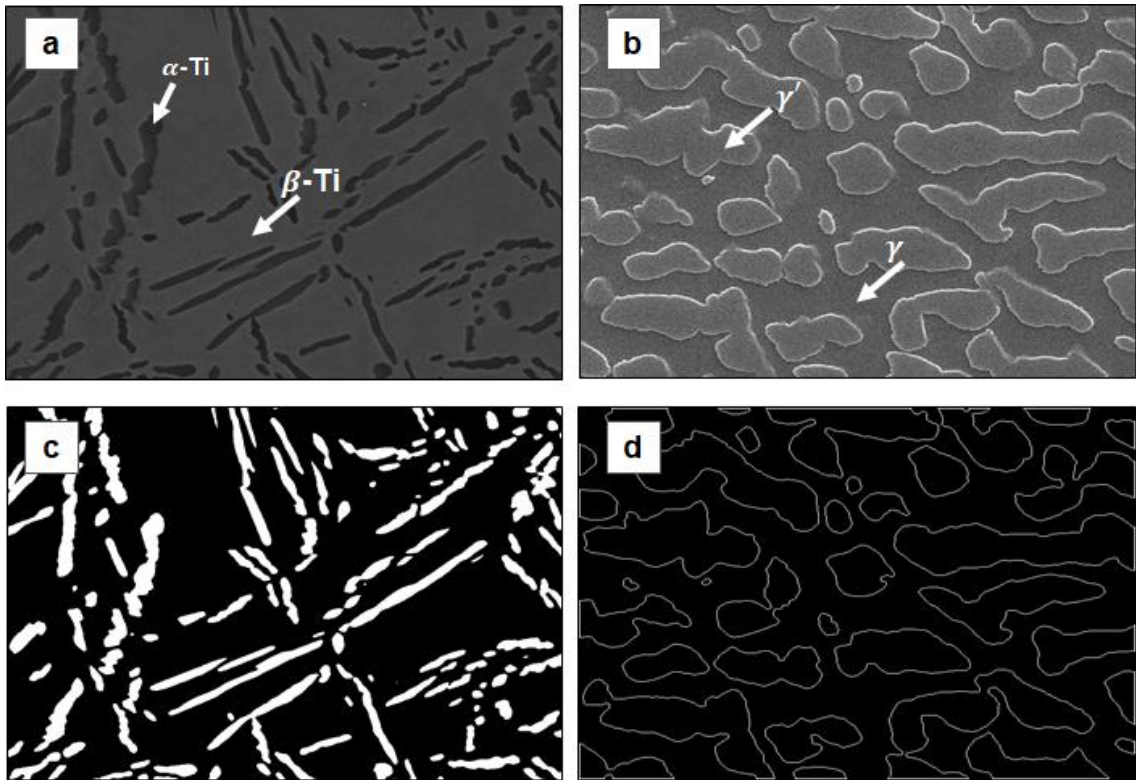


**Figure 18 – Segmentation examples: a) TiMn alloy, where the dark regions are the  $\alpha$ -Ti and light regions are  $\beta$ -Ti, and c) segmented result of a) using intensity thresholding. b) Ni-based superalloy microstructure with  $\gamma'$  precipitates and  $\gamma$  matrix, and d) segmented result of b) using edge detection.**

As an alternative, one can also use edge detection algorithms to identify the feature boundaries and fill in the features. Edge detection is based on labelling a pixel as an edge if the intensity difference between adjacent pixels is above a certain threshold [156] (see the example shown in Figure 18b and Figure 18d). Features that exhibit partially low contrast edges may not be identified easily using simple edge detection algorithms based on a single threshold. In such cases, more advanced algorithms such as the Canny method [157] may be required that can segment continuous edges with fluctuating contrast levels. Since edge detection only identifies boundaries of regions (see Figure 18d), a post-processing step is needed to fill in the interiors of the regions.

### 3.3.4 Post-processing

Post-processing is often needed to improve the segmentation results, as the segmentation step might leave a number of undesired features in the image that need to be adjusted (e.g., remnants of noise). Post-processing can be performed in two subtasks: (i) morphological operations, and (ii) segmentation result cleanup. Several examples post-processing functions to this step are listed in Table 7. The extent of post-processing may vary based on the quality of the results obtained in the segmentation step. For instance, some images may require few post-processing operations, while others may require extensive clean-up.

**Table 7 – Functions available for post-processing in MATLAB [87] and Python scikit-image [145].**

Method	MATLAB	scikit-image
Dilation	<code>imdilate</code>	<code>morphology.binary_dilation</code>
Erosion	<code>imerode</code>	<code>morphology.binary_erosion</code>
Fill image regions and holes	<code>imfill</code>	<code>morphology.flood_fill</code>
Binary shape properties	<code>regionprops</code>	<code>measure.regionprops</code>

The first subtask performs morphological operations in order to adjust the morphology of the features in the segmented image. Mainly the operations include dilation and erosion, which expand and contract the segmented object boundaries, respectively [158]. Dilation and erosion may be sequenced in different order to achieve desired feature modifications [115]. For example, image closing is a sequential process of erosion after dilation, and can be used to close small gaps between objects in the images (see Figure 19a). On the other hand, image opening is accomplished through dilation after erosion, and

can be used to disconnect objects connected with thin boundaries and remove unwanted small objects (see Figure 19b). The extent of dilation and erosion is controlled by a user-defined kernel. The common choices for kernels are based on basic shapes (e.g., circle, rectangle).

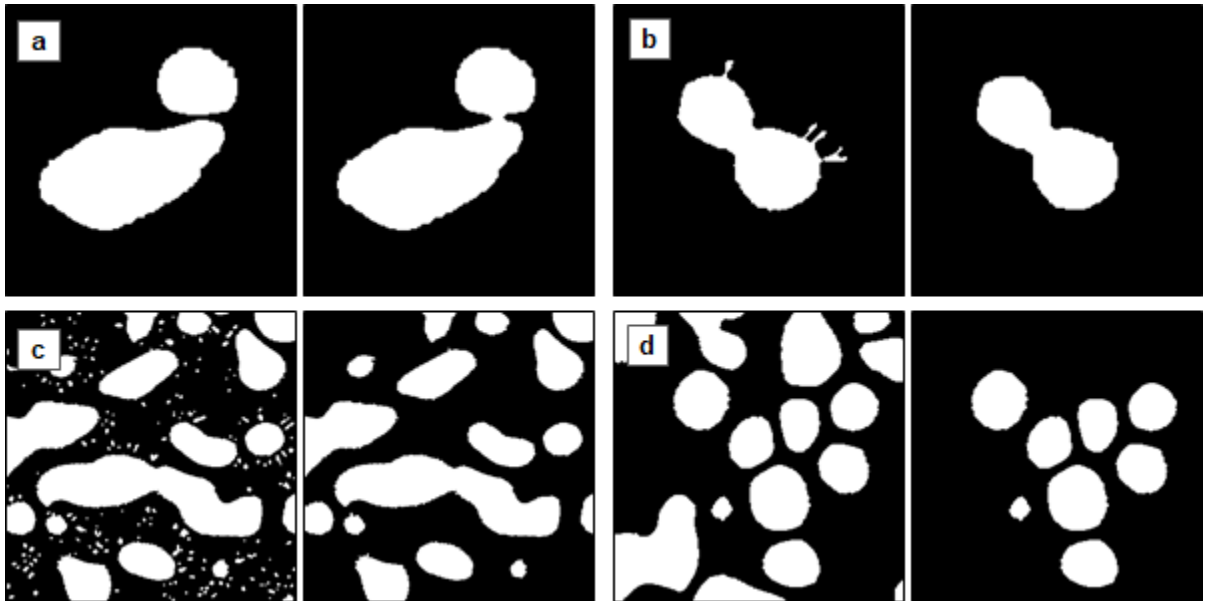


**Figure 19 – Examples of post-processing on segmented images: a) image closing to connect objects that are close to each other, b) image opening to disconnect objects with thin bridges, c) removal of small objects, d) removal of objects cut by the image boundaries.**

The second subtask is aimed at cleaning up the segmentation results. This can be performed using binary shape analysis to exclude or retain objects from the segmented image based on their geometric features (e.g., object area, aspect ratio, geometric moment) or location. For instance, a user may want to remove segmented objects below a certain size (e.g., quantified as the number of connected pixels in each object), as shown in Figure 19c, or retain objects meeting specific geometric attributes (e.g., aspect ratio of an ellipse fitted to the object). In some cases, objects may be removed from the boundaries of the

image to retain only whole objects, as shown in Figure 19d. This step is needed if one aims to extract statistics based on geometric analyses of each full object in the image.

### 3.3.5 *Segmentation validation*

Validation is needed to gain confidence in the segmentation results and provide guidance for further improvement of the segmented workflows. Validation can be a challenging process since we often lack the ground truth for most of the microstructures being studied. Segmentation validation can be approached in two ways: qualitative and quantitative segmentation validations. Qualitative validation is typically performed using inspection and/or expert opinion to visually assess the results. Visual inspection may be a practical first approach in segmentation validation because it may be easily used to detect segmentation errors. On the other hand, quantitative validation is performed using microstructure statistical information. This statistical information varies from basic statistical measures (e.g., volume fraction) to comprehensive microstructure statistics. Although quantitative validation is preferred, it is more challenging to implement in practice.

#### 3.3.5.1 Qualitative validation

Qualitative validation is commonly performed using visual inspection to ensure accuracy of segmentation results. This task may often be performed by a domain expert, as is the case in many studies involving materials images [67, 97, 99]. Figure 20c-Figure 20e show common visualization methods, where the segmented result is shown with the original image using three different techniques: outline, overlay, and labelling [68, 159, 160]. As mentioned earlier, visual inspection may be used to detect obvious errors in

segmentation. For instance, object labelling may be useful to visually identify separated contiguous features, as shown in Figure 20e. In some cases, visual inspection can serve as a main validation method due to ease of validation or unavailability of other means. However, in large datasets these methods may incur significant time and cost investment, and rely on subjective decision from the inspector. Ideally, visual inspection should be limited for purposes of detecting obvious segmentation errors.

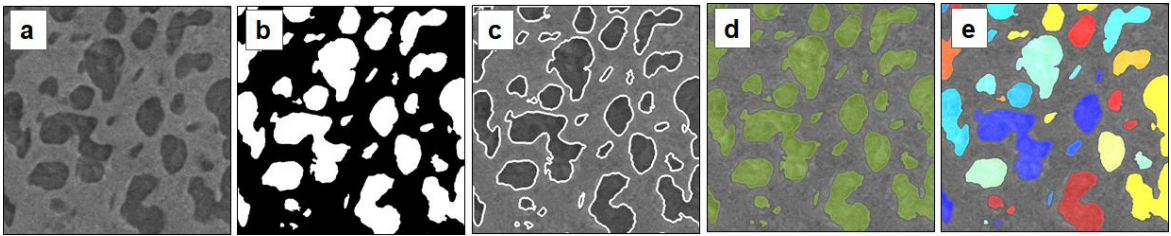


**Figure 20 – Qualitative segmentation validation examples. a) original image, b) segmented image, c) outline of segmented features, d) overlay of segmented features, e) labelled contiguous features.**

### 3.3.5.2 Quantitative validation

Quantitative validation of segmentation results may be accomplished using various microstructure statistics such as volume fractions, grain size distributions, and other higher-order statistics. Volume fraction of local state of interest (e.g., phase precipitates) is a common validation statistic utilized in microstructure segmentation. Volume fraction measurements are generally reported through image analysis-based methods following ASTM E562 [161] or using non-image based characterization techniques such as XRD (x-ray diffraction) [162, 163]. Alternatively, numerical simulations may also be utilized; for example, the equilibrium volume fraction of Ni-based superalloy  $\gamma'$  phase is computed using thermodynamic equilibrium calculation software [164]. In some cases, volume

fraction information may be obtained using analytical calculations, for instance, the expected range of fiber volume fraction in woven carbon fiber composite microstructures [165].

Another option is to validate segmentation using previously established standards in literature. For example, standard methods are widely adopted for reporting the average grain size in metals [166], and nodularity and nodule count in ductile iron [167]. However, it must be noted that standardized methods may be subjective in nature because they often rely on manual techniques (i.e., human evaluation).

Higher-order microstructure statistics may also be utilized for validation. These methods may involve various measures of spatial statistics, such as 2-point spatial correlations [168-170], chord length distributions (CLD) [170-172], and pair correlation functions [173, 174]; these provide higher-order measures of microstructure morphology. However, validation through higher-order microstructure statistics relies on prior knowledge of these statistics for the microstructures being studied.

### **3.4 Segmentation workflows**

A segmentation workflow is defined here as a selection of sequential tasks covering all steps of the segmentation framework described above. The selection of the suitable algorithms in building a robust segmentation workflow that can address a wide variety of microstructures can be quite challenging. In this work, we have focused on two broad classes of segmentation workflows. The first approach utilized all five steps of the segmentation framework to customize a workflow. In such workflows, users control all steps and may design the most favorable segmentation workflow for specific material

microstructures. The second approach is to utilize templated (pre-built) workflows that were designed to be broadly usable for selected classes of microstructure images. We demonstrate these two approaches with different case studies: (i) a custom-built workflow for Ni-based superalloy microstructures, and (ii) templated workflows for a large collection of previously acquired microstructure images from a variety of different material systems.

#### *3.4.1 Custom-built workflow for Ni-based superalloy microstructures*

As an example case study, we undertake the segmentation of  $\gamma'$  precipitates in Ni-based superalloy microstructure images of the type shown in Figure 21a. The shape and size distributions of the  $\gamma'$  precipitates in the  $\gamma$  matrix are known to control the excellent mechanical properties exhibited by superalloys in high-temperature applications [175-177]. The image segmentation workflow for the thermally aged Ni-based superalloy sample is shown in Table 8. Prior to the image acquisition step, the samples were polished and the  $\gamma'$  precipitate phase was chemically etched using Kalling's reagent such that the precipitates are clearly visible using microscopy (see Figure 21a). Due to the size of precipitates (about 1-3  $\mu\text{m}$  in length), the samples were imaged using SEM, which provided sufficient feature spatial resolution and representative microstructure information using a  $22 \mu\text{m} \times 22 \mu\text{m}$  view field. The SEM-BSE mode was chosen for imaging due to good contrast between the  $\gamma$  matrix and  $\gamma'$  precipitates (see Figure 21a). The acquired images exhibited pixel-level noise which was visible after threshold segmentation was applied without noise reduction. Figure 21b shows the image after the preprocessing step, where first, the intensity gradient (global) noise reduction was applied, and second, random (local) pixel-level noise reduction was performed using a Gaussian filter with  $\sigma = 2$  (see Figure

15 for an illustration of how this value was determined). After noise reduction, histogram stretching was performed to increase feature contrast in the image. The image histogram reflected a bimodal distribution, and was then segmented into two local states based on intensity values using global thresholding, as shown in Figure 21c. The segmented images exhibited some residual noise. To finalize the segmentation, the image was post-processed to fill in small holes and remove the remaining small size noise artifacts (see Figure 21d). The segmentation results were validated using two methods: qualitative visual inspection of segmented  $\gamma'$  precipitates and quantitative validation of  $\gamma'$  precipitate volume fraction. The pronounced contrast of the  $\gamma'$  precipitates allowed a visual validation by overlaying the outline of the segmented  $\gamma'$  phase on the original microstructure (see Figure 21e). The average volume fraction of the  $\gamma'$  phase in the segmented images was found to be 0.47, which is within the values estimated using phase-equilibrium thermodynamic simulations. Note that the custom-built segmentation workflow utilized in this example used widely available functions/methods. An advantage to creating such customized workflows is that each step can be carefully tweaked for maximizing the performance of the overall workflow.

**Table 8 – Custom-built segmentation workflow for segmentation of Ni-based superalloy microstructures.**

1. Acquisition	2. Preprocessing	3. Segmentation	4. Post-processing	5. Validation
<ul style="list-style-type: none"> <li>• SEM-BSE microscopy</li> <li>• 22x22 <math>\mu\text{m}</math> view field</li> </ul>	<ul style="list-style-type: none"> <li>• Intensity gradient removal</li> <li>• Random noise removal</li> <li>• Contrast stretching</li> </ul>	<ul style="list-style-type: none"> <li>• Thresholding</li> </ul>	<ul style="list-style-type: none"> <li>• Fill holes</li> <li>• Cleanup (remove small particles)</li> </ul>	<ul style="list-style-type: none"> <li>• Visual inspection</li> <li>• Volume fraction validation</li> </ul>

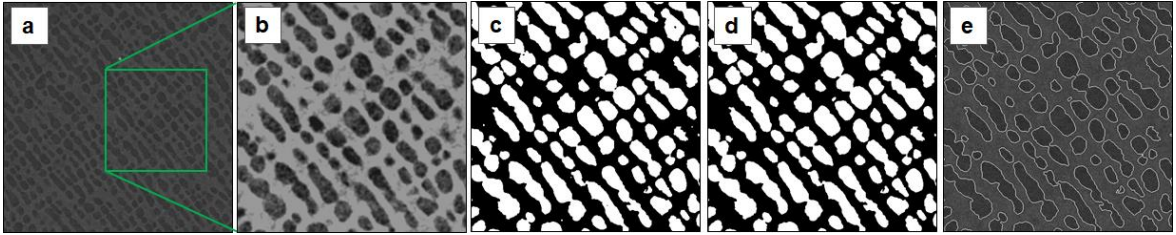


**Figure 21 – Ni-based microstructure images at each of the five steps (images a-e)) of the custom-built segmentation workflow.**

### 3.4.2 *Templated segmentation workflows*

As an alternative approach, one can consider building template segmentation workflows that can be broadly deployed on large collections of microstructure images, potentially acquired by different users and in different material systems. In designing such workflows, one needs to target robustness of the selected options for the different steps in the workflow. It is important to recognize that a single segmentation workflow is unlikely to provide good results for all microstructures. Therefore, one might consider building a limited number of templated (pre-built) workflows that address many of the commonly encountered challenges in segmentation, where each workflow addresses a class of microstructure images. In the present work, we have designed three such templated workflows. These are summarized in Table 9; note that the acquisition and validation steps have been omitted because these steps vary with each image. Workflow 1 was aimed at images that already exhibit a significant contrast in the intensity values for the features of interest. This workflow utilizes global histogram-based thresholding and may require histogram-based preprocessing adjustment to achieve good segmentation results. Workflow 2 was aimed at images exhibiting undesired intensity variations in the image,

which essentially require segmentation using a local threshold method. This workflow typically requires tuning of the segmentation function (e.g., neighborhood size for local thresholding) to achieve the best results. Workflow 3 was aimed at images that exhibit a strong edge contrast for the features of interest. Therefore, for this workflow, segmentation will be pursued by identifying the edges first and then filling the edges to identify the features of interest. In this workflow, contrast enhancement and adjustment of edge detection algorithm need to be tuned properly to achieve good segmentation results. In all workflows, the post-processing methods are chosen that are most likely to improve the final segmentation results. For instance, in Workflows 1 and 2, cleanup is performed based on object size or shape to remove remaining noise and unwanted incorrectly segmented regions. Alternatively, in Workflow 3, the feature outlines (edges) are filled in and image opening is performed to remove remaining noise or unwanted segmented edges.

The images for this case study were selected from six different material systems to represent a variety of features; example micrographs from each material system are shown in the left column in Figure 22. The Ni-based superalloy microstructure in Figure 22a shows etched  $\gamma'$  precipitates. The acquired image exhibits significant overlap in the intensity values for the  $\gamma$  and  $\gamma'$  regions, and therefore poses challenges in segmentation. Images shown in Figure 22b and Figure 22c are acquired from additively manufactured samples from Ti-Ni and TiMn alloys, respectively. In these images large  $\alpha$ -Ti needle features are clearly visible. Even though these features appear similarly in both images, the features in Figure 22c exhibit rougher edges, which adds challenges to segmentation. Figure 22d shows a Ti64 microstructure with sufficient contrast between the  $\alpha$ -Ti and  $\beta$ -Ti phases. However, the lamellar morphology in some of the grains adds challenges to the

segmentation. Figure 22e shows a steel microstructure with small embedded graphite particles (dark features) in the matrix. This image is mostly homogenous due to a low fraction of graphite and exhibits unwanted streak artifacts due to sample preparation that are frequently encountered in such images. Lastly, Figure 22f shows a polymer composite microstructure where there is adequate contrast between the features of interest. However, this image exhibits low feature spatial resolution and high pixel-level noise, adding challenges to the segmentation.

The segmented versions of the input image obtained using each of the three template workflows (see Table 9) are shown in Figure 22. All of the segmentation results were evaluated using visual inspection since the features could be visually distinguished, and quantitative validation options were not readily available for these microstructure images. Workflow 1 is the simplest segmentation approach among the three workflows as it utilizes a global thresholding strategy. As such, one should expect this workflow to work well only on images with a significant contrast in the features of interest. In the present case study, it is seen that Workflow 1 performed well on Figure 22b and Figure 22f, where the features are indeed well-separated by intensity values. The images in Figure 22d and Figure 22e were also well segmented by Workflow 1, but only after tuning of the contrast enhancement steps described earlier in this work. Similarly, the image in Figure 22c also showed good segmentation results with Workflow 1 after the implementation of additional post-processing steps to isolate the needle shapes. Workflow 1 is therefore well suited for microstructures where the features throughout the whole image can be reliably segmented largely based on intensity values. For instance, the image in Figure 22a is not well

segmented by Workflow 1 because of the overlap in the intensity values in the matrix and precipitate features.

**Table 9 – Templated workflows that can be used in the segmentation of most microstructure images.**

	Preprocessing	Segmentation	Post-processing
Workflow 1	<ul style="list-style-type: none"> <li>Noise removal</li> <li>Contrast stretching</li> </ul>	<ul style="list-style-type: none"> <li>Global thresholding</li> </ul>	<ul style="list-style-type: none"> <li>Result cleanup (size and shape-based)</li> </ul>
Workflow 2	<ul style="list-style-type: none"> <li>Noise removal</li> <li>Contrast stretching</li> </ul>	<ul style="list-style-type: none"> <li>Local adaptive thresholding</li> </ul>	<ul style="list-style-type: none"> <li>Result cleanup (size and shape-based)</li> </ul>
Workflow 3	<ul style="list-style-type: none"> <li>Noise removal</li> <li>Contrast enhancement</li> </ul>	<ul style="list-style-type: none"> <li>Edge detection</li> </ul>	<ul style="list-style-type: none"> <li>Fill in features</li> <li>Image opening</li> </ul>

Workflow 2 utilized a local thresholding as a segmentation step and performed well on most images with less tuning required in the preprocessing step compared to Workflow 1. In addition, this workflow performed well for the image in Figure 22a in segmenting features exhibiting similar intensity values. However, Workflow 2 tended to oversegment the image in Figure 22d. Workflow 2 is well suited for applications with contiguous features (e.g., precipitates), and typically requires careful tuning of the segmentation function for best results. An important factor in achieving good segmentation of microstructure features is selection of optimal neighborhood size in the segmentation function (as described in the segmentation step). The neighborhood should be sized to contain different local states yet small enough to avoid large intensity overlap with unwanted objects. For instance, the neighborhood size was 21 pixels for the image (400 px × 400 px) in Figure 22a and 51 pixels for the image (1024 px × 1024 px) in Figure 22e, which allowed good segmentation with few errors due to intensity overlap between two different feature classes.

Workflow 3 is based on detecting feature outlines in images and performs well on images in Figure 22a and Figure 22e. However, this approach undersegments features on the image boundaries in Figure 22a. In particular, it appears to perform well when the features in the image are not cut off by the image border. This workflow performs poorly on the rest on the images due to the insufficient contrast that prevents reliable continuous edge detection. This approach, coupled with suitable preprocessing and post-processing operations, may perform well in cases where different classes of features are separated by feature outlines rather than intensity values.

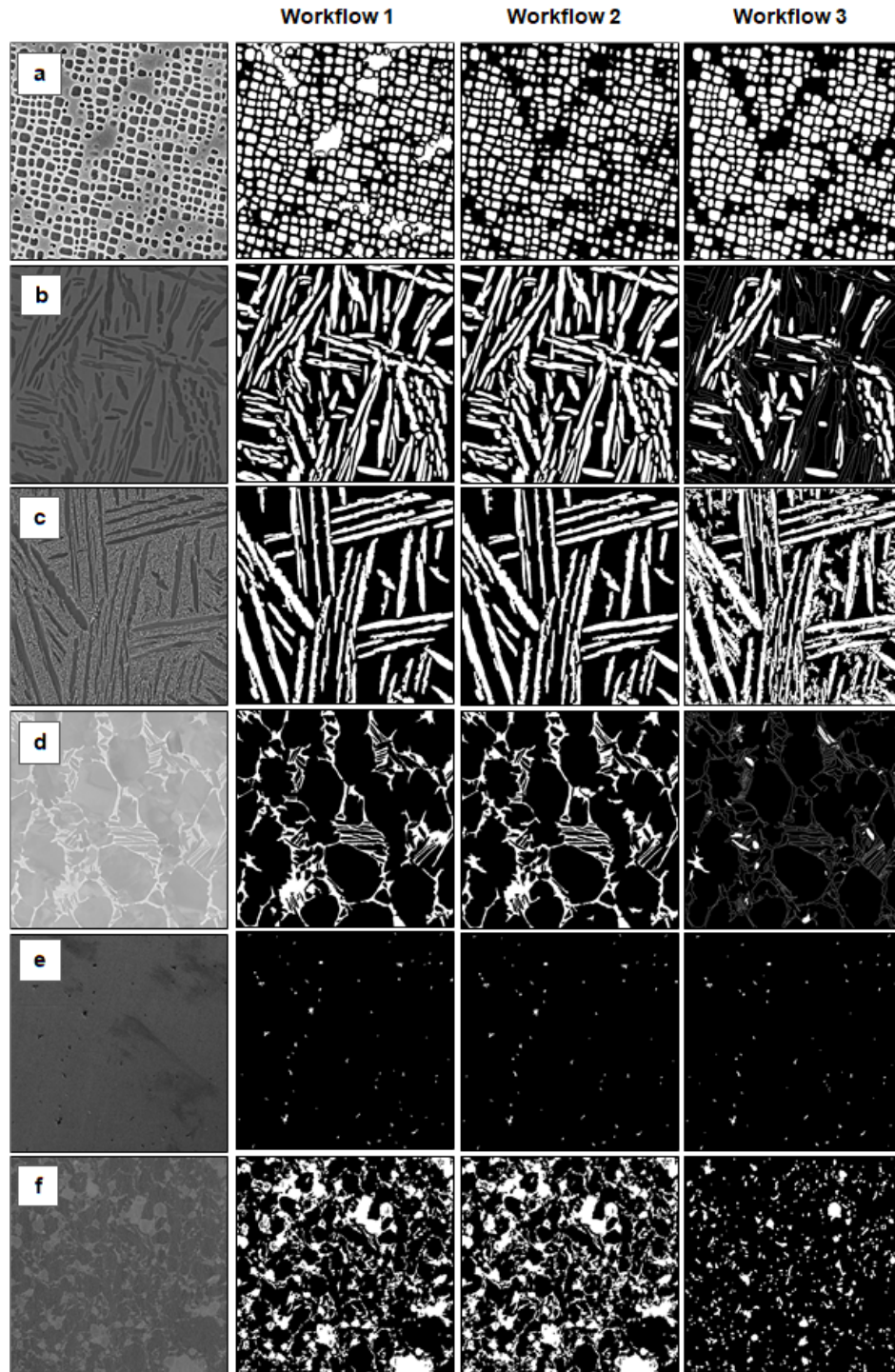


Figure 22 – Previously acquired microstructure raw images (left column) and their segmented results utilizing the three templated workflows (right three columns) identified in Table 9.

This case study demonstrated that various types of microstructure images may be segmented sufficiently well using a limited number of templated workflows created using the segmentation framework presented in this work. It is hoped that the approach outlined here may open new avenues for automated or semi-automated segmentation of the very large number of microstructures images contained in legacy collections of micrographs in many research laboratories.

### **3.5 Conclusions**

In this work, we develop a systematic framework designed to segment a wide variety of microstructure images. The framework consists of five important sequential steps that include image acquisition, preprocessing, segmentation, post-processing, and validation. Each step is further designed to include necessary tasks, subtasks, and options that must be taken to reliably segment images. Furthermore, the tools and algorithms in the framework employ functions that are widely available in popular software tools such as MATLAB and Python. The developed framework leads naturally to design and implementation of segmentation workflows. The application of the developed framework was illustrated through the design and implementation of two types of segmentation workflows. The first workflow produced was a custom-built workflow utilizing all five framework steps to segment Ni-based superalloy images. In the second case, templated workflows were constructed and applied to previously acquired images of six different material systems. Although the examples in this work illustrate segmentation of microstructure images into two local states (i.e., black and white), it is important to point out that the developed framework can be directly applied to segmentation of an arbitrary number of local states. This mostly entails considerations in the segmentation and post-processing steps. In the

segmentation step, the number of microstructure local states should be specified in suitable segmentation functions/algorithms. In post-processing, the different segmented local states can be processed individually (i.e., by specifying the local state on which to perform specific post-processing functions).

## CHAPTER 4.

### APPLICATION OF PROTOCOLS TO MULTIREOLUTION STUDY OF THERMALLY AGED FERRITE-PEARLITE STEELS

#### 4.1 Introduction

The protocols for multiresolution spherical indentation and image segmentation described in previous chapters have now set the stage for systematic investigations of the microstructure and mechanical responses of heterogeneous material systems and the critical evaluation of available composite theories. In this study, we conduct such an investigation into the mechanical response of thermally aged ferrite-pearlite steel samples. The prolonged thermal exposures (up to 500 °C and 91,000 hours) in these steel samples contribute to significant changes in the microstructures that typically translate to reduction in yield strength [69-73].

In this study, the spherical ISS protocols were employed on the individual microscale constituents (i.e., ferrite, pearlite) using nanoindentation as well as at the macroscale using microindentation. The respective yield strengths of the microscale constituents and the bulk yield strength of the sample were estimated from these measurements. The microstructures of these samples were documented using optical microscopy (OM), where images were segmented and the relevant microstructure statistics were extracted. All of this information was used to evaluate the composite theory estimates based on simple composite theories for mechanical property homogenization. It is shown that the multiresolution spherical indentation and image segmentation protocols employed in this study produce results that

are highly consistent with the bounds estimated for these material systems from the simplest of the composite theories. This work validates the developed protocols, which can dramatically reduce the cost and effort needed for the multiresolution mechanical evaluation of heterogeneous material systems.

## **4.2 Thermally aged ferrite-pearlite steels**

In this work, multiresolution mechanical evaluation is performed on 0.3% C steel samples with three different levels of thermal exposure histories, shown in Table 10. The samples in this study were selected from a library of samples from the study in Section 2.1.3, which were excised from in-service gas turbine components. The sample names in Table 10 indicate the level of thermal exposure based on the service time and temperature (note that baseline material is labelled as Unexposed). The service temperature code in Table 10 represents a normalized value of temperatures recorded during service, where 1.00ST corresponds to the maximum temperature between all samples.

The ferrite-pearlite steels exhibit a hierarchical microstructure that initially consists (i.e., in Unexposed sample) of two main grain-scale constituents, ferrite and pearlite, as shown in Figure 23a. The ferrite constituent is made up of  $\alpha$ -ferrite, and the pearlite constituent is comprised of lamellar arrangement of  $\alpha$ -ferrite and cementite ( $\text{Fe}_3\text{C}$ ) phases. The  $\alpha$ -ferrite phase consists mainly of iron with small amounts of interstitial carbon, and is the softer microscale constituent in the samples. On the other hand, the pearlite grains represent the harder microstructure constituent that exhibits a lamellar arrangement of soft ferrite and hard cementite phases in the baseline (no thermal exposure) material. Thermal exposure of these steels generally leads to significant changes in the microstructure and

substantial reduction of the effective mechanical properties, such as yield strength [12, 71, 72, 80]. At moderate levels of thermal exposure, the lamellar pearlite structure undergoes spheroidization in the temperature ranges of 454-760 °C [70, 72, 178]. An example of this microstructural change can be seen in the optical micrograph in Figure 23b. At higher levels of exposure, one observes spheroidization and graphitization, as seen in the optical micrograph in Figure 23c. Graphitization results from the diffusion of carbon from  $\alpha$ -ferrite and cementite phases to form secondary graphite particles in temperature ranges of 427-593 °C [69-73]. It should be noted that there is significant overlap in temperature for which the graphitization and spheroidization processes occur, therefore one can expect to observe both graphitization and spheroidization phenomena in the steel samples.

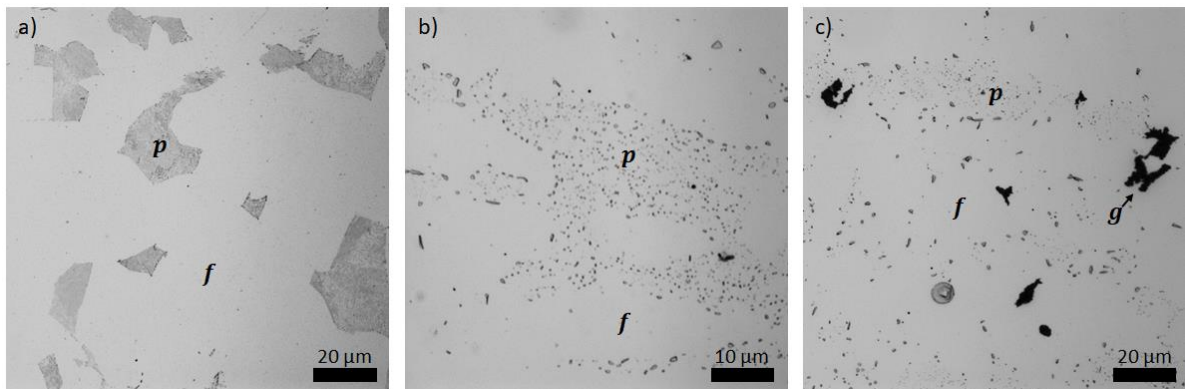


**Figure 23 – Example optical microscopy (OM) microstructure images at different magnifications for different levels of thermal exposure. a) unexposed sample with ferrite (*f*) and lamellar pearlite (*p*), b) moderate exposure sample with pearlite spheroidization (at higher magnification than a) and c), c) high exposure sample with pearlite spheroidization and graphitization (*g*). The details of exposure times and temperature are provided in Table 10.**

### 4.3 Sample Preparation

Samples studied in this work were mounted in standard epoxy resin such that the sample surface is exposed on both opposing sides. The samples were ground on both sides to ensure parallel surfaces needed for the indentation tests. For microindentation and microstructure image acquisition, the sample surfaces were polished up to 0.02  $\mu\text{m}$  colloidal alumina suspension and vibropolished in a 4:1 ratio of water to colloidal silica mixture as the final step, which resulted in the slightly etched surfaces shown in Figure 23. The slight etching of the sample surface enabled clear identification of lamellar and spheroidized pearlite grains, as well as the graphite particles. For nanoindentation, the samples were further electropolished, in an electrolyte consisting of 6% perchloric acid (60%), 14% distilled water, and 80% ethanol [179], to minimize any remaining scratches from mechanical polishing and to ensure a flat surface within each grain. The electropolishing process tends to remove material at different rates based on the orientation of the grains which leaves an uneven surface between grains with different orientations and therefore may not be well suited for indentation tests multiple grains at once (e.g., microindentation). It is important to note that the electropolishing process clearly revealed grain boundaries, which enabled confident identification of ferrite and pearlite constituents for indentation.

**Table 10 – Specimens received for study with different exposure conditions. Superscript \* indicates samples where tensile test specimen were made in addition to microstructure and indentation measurements.**

Sample name	Approximate service hours	Service temperature code
Unexposed*	--	--
Moderate exposure	22,000	0.98 ST
High exposure*	91,000	0.85 ST

#### 4.4 Image Segmentation

As mentioned in Chapter 3, in the context of microstructure images, segmentation can be defined as the process of labelling each pixel (or voxel in 3D) with the correct local microstructural feature (e.g., thermodynamic phase, microconstituent structures, grain boundary). For the microstructure of the steels samples shown in Figure 23, the three local microstructural states of interest are ferrite, pearlite, and graphite. Segmentation of the microscopy images obtained in this work was conducted following the framework developed in Chapter 3 for designing segmentation workflows. The sequence of the five framework steps to accomplish segmentation for the microstructures in this study are described in detail next.

##### *Step 1 – Image acquisition*

In the present study, images were captured using a Zeiss Observer A1.m light optical microscope. To strike a balance between capturing sufficient details of pearlite spheroidization and a representative distribution of ferrite-pearlite grains in each image, a magnification corresponding to a view field of  $312 \times 312 \mu\text{m}$  was chosen, which corresponds to a spatial resolution of  $0.3 \mu\text{m}/\text{pixel}$  in  $1040 \times 1040$  pixel images. A

magnified portion of a typical acquired image for high exposure sample is shown in Figure 24a (magnified for improved feature visualization; non-magnified images are shown in Figure 25). Optimal microscope image acquisition parameters were adjusted to provide as much contrast as possible for spheroidized pearlite grains without affecting details of other features.

### *Step 2 – Image preprocessing*

The next step in the segmentation workflow addressed image noise reduction and contrast enhancement of the features of interest. Image noise reduction was tackled both on the image-scale (e.g., reducing unwanted intensity gradient over the image) and pixel-scale (i.e., reducing random variation of individual pixel intensities). A shadow gradient (i.e., intensity gradient) over the raw images was reduced by subtracting an approximated shadow profile from the noisy image. Random pixel-scale noise throughout the image was removed using Gaussian filtering [115]. It is important to note that optimal filtering of random noise requires a balance between noise reduction and retention of feature details (e.g., details of feature edges). In this study, an optimal Gaussian filtering strength was chosen based on the lowest similarity between the removed random noise and the filtered image using the methodology described in Section 3.3.2.1. Following noise reduction, contrast enhancement was performed on the whole image using contrast stretching [147], which increases the difference in intensity values throughout the image. The consequence of this step can be seen by comparing the raw image in Figure 24a and the preprocessed image Figure 24b.

### *Step 3 – Segmentation*

Next, the segmentation step is performed to label each image pixel with a microstructure local state of interest. In this step, the goal is to label each pixel in the image as the ferrite or pearlite (lamellar or spheroidized) or graphite. An intensity thresholding approach was utilized, which separates the image intensities into  $k + 1$  classes using  $k$  thresholds based on grayscale intensities. In the present work, the pixels in each image are separated into three classes using the multi-Otsu threshold approach [112]. This thresholding segmentation resulted in labelling the image pixels into three classes corresponding to graphite, pearlite, and ferrite. An example outcome from this procedure is shown in Figure 24c, where the three different microstructural states are colored differently. Note that the segmented image in Figure 24c is for the High exposure sample with spheroidization and graphitization. In this image, the pearlite components appear as clusters. These clusters will be coalesced, and other clean-up tasks are performed in the post-processing step.

### *Step 4 – Post-processing*

The main goal of the post-processing step is to reassign incorrectly labeled pixel values to their correct microstructural feature labels or filter out unwanted objects from further analysis. For current segmented images, image closing [115] was first performed to connect the clustered pearlite particles seen in Figure 24c. Image closing is a sequence of dilation (expansion of object boundaries) and erosion (shrinking of object boundaries). The resulting connected clusters represent the regions of the pearlite constituents (lamellar or spheroidized) in the micrographs. Next, several types of incorrectly labelled features were cleaned up in the ferrite matrix. First, small round features with lower intensities (i.e.,

darker in grayscale) that were labelled as graphite were relabeled as part of ferrite matrix because they likely correspond to material inclusions and/or pitting during the polishing process. Then, pixels directly surrounding graphite particles were reassigned to ferrite if they were incorrectly labelled as pearlite. This incorrect labelling was observed in ferrite matrix that surrounded graphite particles, where the ferrite was noticeably darker (lower intensity) and therefore was incorrectly labelled as pearlite. Finally, pixel-scale particles that belonged to other microstructure states throughout the ferrite matrix were relabeled to ferrite. This likely resulted from the few highly noisy pixels that remained after the preprocessing step. As mentioned earlier, noise reduction requires a balance between elimination of noise and retention of detail, which typically leaves few noisy pixels that are then labelled incorrectly during the segmentation step. An example of the final post-processed image for an exposed sample is shown in Figure 24d.

#### *Step 5 – Segmentation validation*

The final step of the segmentation workflow focuses on the validation of the post-processed segmentation results to assess the confidence in the segmentation results. In practice, segmentation validation can be a challenging process because the ground truth for most studied microstructures is not available. As mentioned earlier, studies involving materials images often rely on qualitative visual inspection [67, 97, 99] due to ease of validation or unavailability of other means. In this work, the validation was performed visually by overlaying the outlines of segmented features over the grayscale images to check the accuracy with which the different constituent boundaries are captured. This is illustrated in Figure 24e. In this work, visual inspection provided reasonable validation since the constituents were clearly distinguished from each other. Furthermore, a relative

quantitative validation was performed by comparing the fraction of pixels labelled as pearlite in each image. Although the expected pearlite fraction for these samples is not precisely known, the level of consistency of identified pearlite fraction between images can serve as a guide to identify potential issues in the segmentation process.

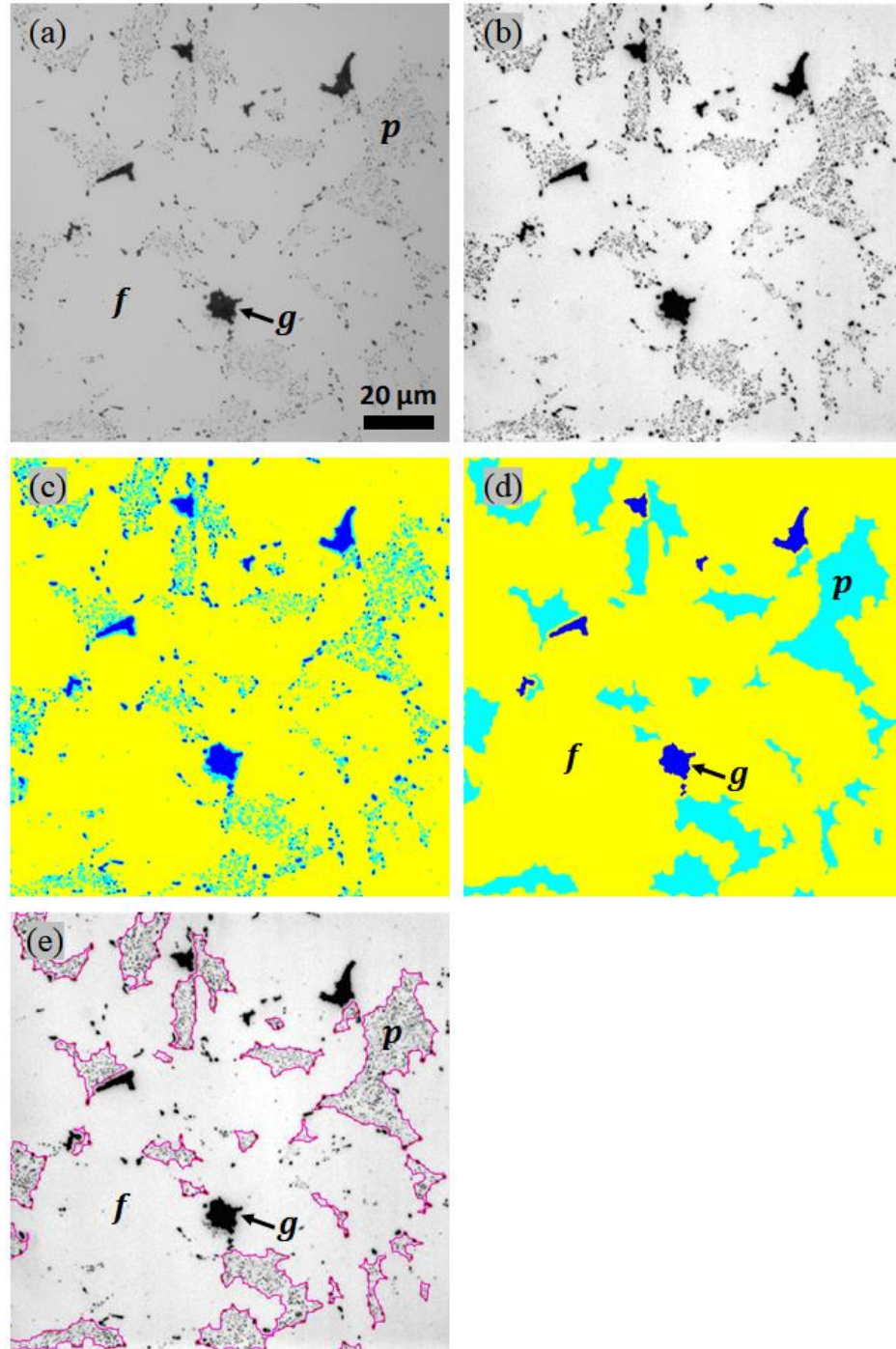
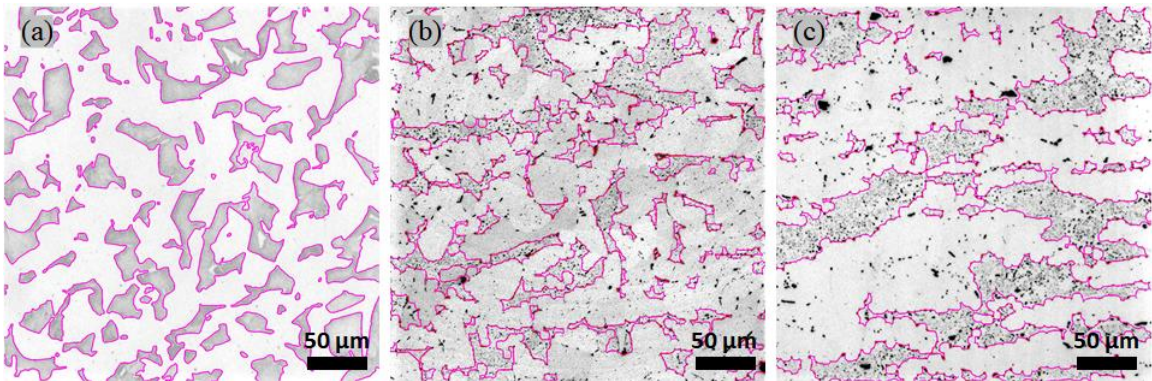


Figure 24 – Illustration of the individual steps in the segmentation workflow developed and implemented on the images studied in this work. Note that these images show a magnified region of the original image to display the microstructure details. a) Acquired raw image from optical microscopy, b) preprocessed image with removed noise and increased contrast, c) segmented image showing three microstructural states, d) post-processed image, and e) visualization of segmented pearlite (outlined in magenta) on the preprocessed image.

All of the images were segmented following the developed segmentation workflow. An example of a representative segmented image for each sample is shown in Figure 25. Each sample contained 10 images. The volume fraction of pearlite,  $v_p$ , was determined for each image as the fraction of the total pixels labelled as pearlite and is reported in Table 11. Note that the ferrite volume fraction was calculated as  $v_f = 1 - v_p$ . This means that the graphite particles were counted as part of the ferrite matrix. This is a reasonable assumption, as the graphite fraction tends to be low (less than 2% on average in most samples). Furthermore, the graphite particles are highly scattered throughout the samples (no graphite clusters were observed) and likely do not affect the bulk material yield strength significantly.



**Figure 25 - Example of visualization of segmented images for the thermally aged samples.,(a) Unexposed sample, (b) moderate exposure, (c) high exposure.**

#### **4.5 Mechanical characterization results**

The main objective in this section is to demonstrate multiresolution mechanical evaluation of the thermally aged steels using the ISS protocols developed in Chapter 2. This is achieved by using different radius indenter tips to probe different indentation zone

volumes within the sample material. The microindentation protocol with a large indenter tip ( $R_i=6.35$  mm) was utilized to probe an indentation zone with a sufficiently large number of all microscale constituents (i.e., ferrite and pearlite grains) for an estimation of the bulk material response. On the other hand, the ferrite and pearlite constituents were evaluated using nanoindentation protocols with a smaller indenter tip ( $R_i=100$   $\mu\text{m}$ ) to contain the indentation zone within each constituent.

#### *4.5.1 Evaluation of bulk properties with microindentation*

Microindentation tests were performed using a 6.35 mm radius indenter tip to estimate the bulk mechanical response of the samples. Figure 26a shows an example of an estimated contact radius,  $a$ , at yield for the Unexposed sample, which corresponds to primary indentation zone of a cylinder of radius  $a$  and height  $2.4a$ . In Figure 26a, it can be seen that for a contact radius of about 100  $\mu\text{m}$ , a large number of grains are activated within the indentation zone and it is reasonable to assume that these tests estimate the bulk material response. Using this reasoning, each sample was evaluated in random locations throughout each sample with at least seven indentation tests. The microindentation tests for all three samples are summarized in Table 11, where a trend of decreasing yield strength with thermal aging is observed.

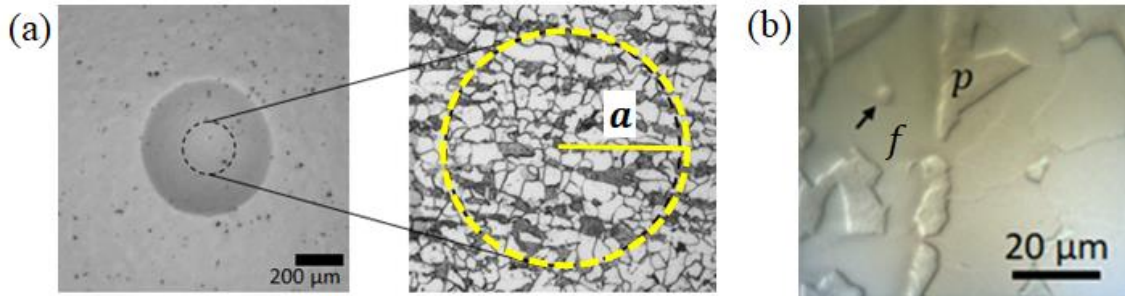


**Figure 26 – a) Top view of residual indentation impression after a microindentation test, where the yellow outline corresponds to the contact area at indentation yield stress displayed on an etched sample, b) top view of residual indentation impression (arrow) after a nanoindentation test within a ferrite grain.**

Tensile measurements were also performed on the Unexposed and High exposure samples (Section 2.1.3), which showed that 0.2% strain offset yield strength ratio between the microindentation and tension tests is about 2. This ratio is in close agreement with experimental studies [50, 58] and FE simulations [61] using the current ISS protocols, which provides confidence in estimation of bulk properties corresponding to uniaxial tests using current microindentation tests. Figure 27 summarizes the average microindentation yield strength and one standard deviation for all three samples.

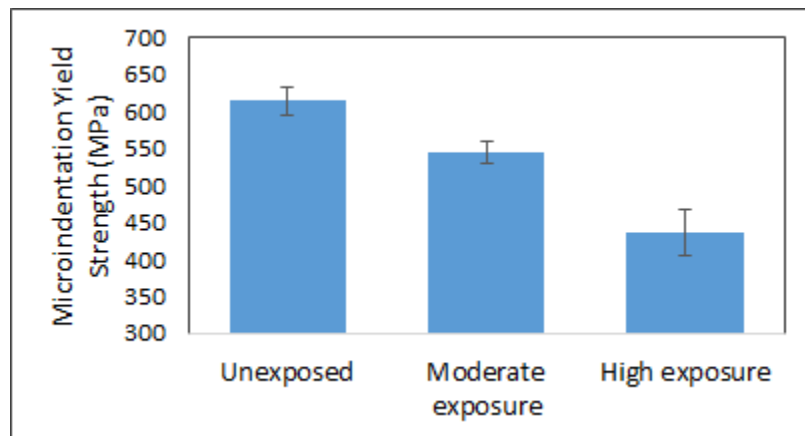


**Figure 27 – Microindentation yield strength measured for the thermally exposed samples in this study.**

#### 4.5.2 *Evaluation of ferrite and pearlite constituents with nanoindentation*

The evaluation of ferrite and pearlite constituents was performed with 100  $\mu\text{m}$  radius indenter tip, where each indentation was performed close to the center of a single constituent grain. An example of a post-indentation impression in a ferrite grain is shown in Figure 26b. The tip size was chosen to ensure that the indentation zone was contained well within a single constituent grain in each test. In addition, the 100  $\mu\text{m}$  tip ensured a large enough contact radius and indentation zone to activate multiple cementite laths in lamellar pearlite and also multiple spheroidized cementite particles in thermally aged samples. Representative nanoindentation load-displacement curves and corresponding indentation stress-strain curves for ferrite and pearlite constituents for all three samples are shown in Figure 28a and Figure 28b, respectively. For each sample, at least eight measurements within each ferrite and pearlite constituents were made. The elastic modulus and the 0.2% plastic strain offset yield strength for ferrite and pearlite constituents in each sample are summarized in Table 11. Nanoindentation measurements of both ferrite and pearlite constituents reveal a trend the of decreasing yield strength with increasing thermal exposure. This trend is consistent with the bulk material yield strength measurements estimated with microindentation tests.

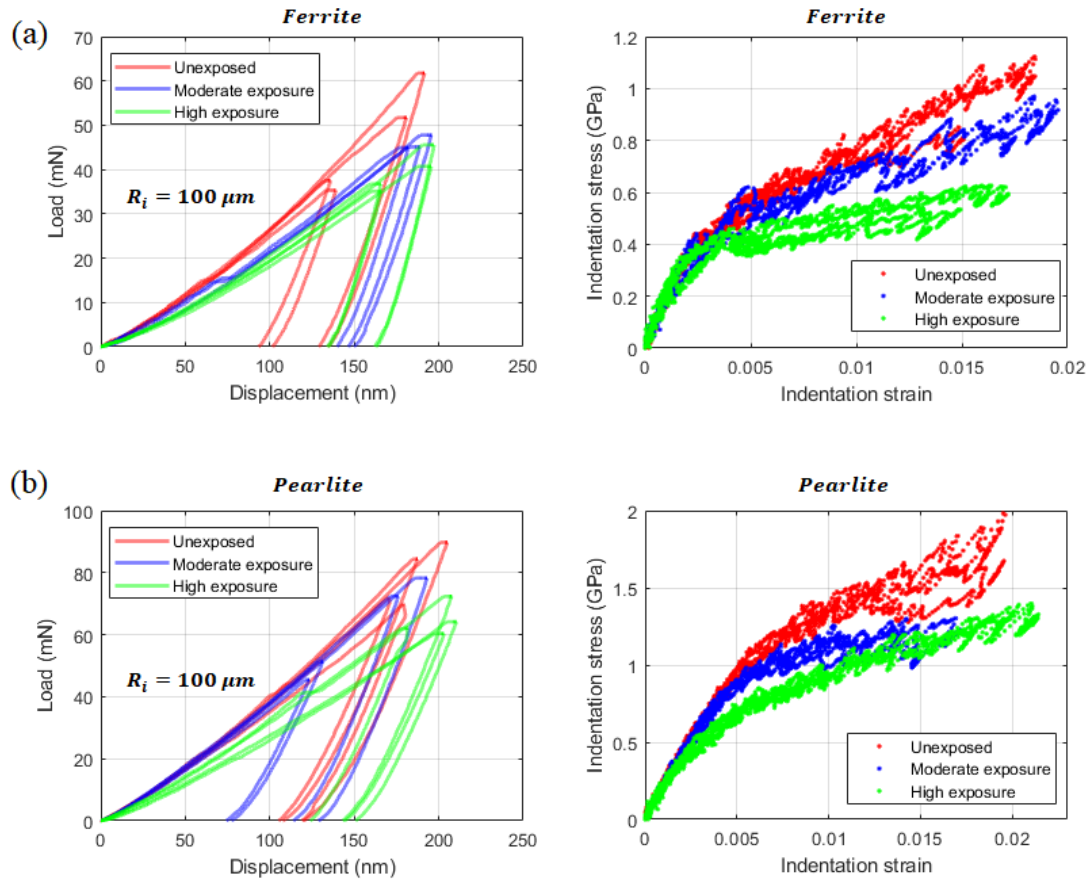


**Figure 28 – Examples of nanoindentation load-displacement (left column) and corresponding indentation stress-strain curves (right column) for (a) ferrite and (b) pearlite constituents for all samples.**

**Table 11 – Summary of microstructure statistics and indentation measurements on the thermally aged steels samples.**

Sample	Microstructure statistics (segmented OM images)		Nanoindentation measurements				Microindentation measurements	
	Ferrite %	Pearlite %	Ferrite		Pearlite		Bulk properties	
	$V_f$	$V_p$	$E_s$ (GPa)	$\sigma_{y,f}$ (MPa)	$E_s$ (GPa)	$\sigma_{y,p}$ (MPa)	$E_s$ (GPa)	$\sigma_{y,ind}$ (MPa)
Unexposed	71.1%	28.9 ± 2.1%	173 ± 2.0	515 ± 29.5	203 ± 3.5	1047 ± 136.4	186 ± 9.6	615 ± 18.6
Moderate exposure	74.3%	25.7 ± 5.7%	173 ± 2.8	491 ± 25.3	190 ± 7.0	995 ± 40.2	187 ± 9.1	544 ± 14.9
High exposure	75.0%	25.0 ± 3.9%	177 ± 8.2	413 ± 24.2	191 ± 3.6	715 ± 26.2	187 ± 11.6	436 ± 32.2

#### 4.6 Correlation of yield strength at multiple scales

For many engineering applications, the effective mechanical properties controlling the performance characteristics can be modeled as a function of the material microstructure and the properties of the microscale constituents using established composite theories. Such theories are based on various approaches, including mean-field theories [180-183], statistical continuum theories [18, 184-192], and computational homogenization [193-200]. One of the main distinguishing factors between the different approaches lies in the level of the microstructure details taken into account in estimating the homogenized properties of interest. The simplest of these theories for estimating the effective yield strength of the composite material may be formulated as well-known “rules of mixtures” [201-203]. These estimates generally provide upper and lower bounds for the effective yield strength of the material based on the volume fractions of the microscale constituents and their respective yield strengths. Other approaches incorporate higher-order microstructure statistics (e.g., statistical continuum theories [185, 186]) and computational

strategies (e.g., finite element models [23, 193, 194, 196, 198]). Although the more sophisticated approaches can provide higher fidelity estimates, they often also require significantly higher computational effort. A significant hurdle in the advancement of composite theories has been the lack of a sufficiently large experimentally measured datasets of microstructures and their effective properties, which can be used to critically validate and/or refine the different composite theories. The protocols developed in this work aim to bridge this gap. To demonstrate this, the collected microstructure and multiresolution indentation measurements in previous sections were used to evaluate composite theory estimates based on the simple rules of mixtures and self-consistent models.

#### 4.6.1 Rule of mixtures

A frequently used rule of mixtures (ROM) model is based on Voigt model [204] for estimation of elastic properties of a multi-constituent composite based on the contribution of each constituent by volume fraction. This approach attractive for its simplicity and is broadly adapted as a linear ROM model to estimate yield strength in multiphase composites [202]. The following is an adaptation of the linear ROM for the current study:

$$\sigma_{yc} = v_f \sigma_{yf} + v_p \sigma_{yp} \quad (17)$$

where  $\sigma_{yc}$  is the yield stress of the composite material,  $\sigma_y$  is the yield stress, and  $v$  is the volume fraction of a constituent. The subscripts  $f$  and  $p$  correspond to ferrite and pearlite constituents, respectively.

The Voigt ROM corresponds to the case when an applied load on the composite causes equal strains in all constituents (isostrain). Therefore, the overall composite stress on the composite is the sum of stresses carried by each constituent, which is weighted by the volume fraction of each constituent. On the other hand, a ROM by Reuss [205] corresponds to the case when all constituents carry equal stress (isostress). Therefore, the corresponding strain of the composite is the sum of strains experienced by all constituents. The Voigt and Reuss mixture models correspond to the upper and lower bounds of effective properties, respectively. However, the composite behavior in most cases typically falls between the two bounds. Consequently, a modified rule of mixtures model has been proposed by Tamura et al. [206] for yield strength estimation of composites. which is based on modeling the harder phase as elastic and the softer matrix phase as elastic-plastic. This is a reasonable assumption for many multiphase metals as shown on a study on dual-phase steels [207]. In this study, the modified ROM is adapted to model the ferrite-pearlite composite yield strength,  $\sigma_{yc}$ , by treating the pearlite constituents as the hard phase:

$$\sigma_{yc} = \sigma_{yf} \left( v_f + \frac{E_p v_c}{E_f R} \right) \quad (18)$$

$$R = \frac{q + 1}{q + E_f/E_p} \quad q = \frac{\sigma_p - \sigma_f}{E_p \varepsilon_p - \varepsilon_f} \quad (19)$$

where  $E_f$  and  $E_p$  correspond to the Young's modulus of ferrite and pearlite constituents, respectively. A dimensionless parameter,  $q$ , corresponds to the normalized ratio of the stress to strain transfer ( $0 \leq q \leq \infty$ ). In general, the value  $q$  is an empirical parameter and depends on many factors such as composition, microstructural arrangement, flow stress

ratio, and strain hardening of constituent phases. However, the exact nature of this dependence is not yet well known. The choice of  $q \rightarrow 0$  refers to Reuss model and  $q \rightarrow \infty$  refers to Voigt model. In a study on dual-phase steels, the value of  $q$  of about 4.5 has shown reasonable comparison to experimental results [207] and is used in this case.

#### 4.6.2 *Self-consistent model*

Self-consistent models account for the deformation heterogeneity of different constituents without the assumption of either equal stress or equal strain throughout the composite material, and have been extensively used to model plasticity of two-phase metals [180, 208-210]. In this study, we use the self-consistent model developed by Stringfellow and Parks [209].

In the current approach, the composite material is modeled by considering  $N$  distinct local phases of spherical incompressible inclusions embedded in a homogeneous equivalent medium. The behavior and the distribution of the inclusions is assumed to be isotropic, leading to an overall isotropic behavior of the composite material. These idealizations allow the model to be formulated in terms of equivalent shear strain rate, and equivalent shear stress. Given these assumptions, relations between the macroscopic and the local volume averaged strain and stress fields can be derived from Eshelby solutions [17] for isotropic incompressible spherical inclusions in an incompressible matrix [209, 211]. The ratio of the average equivalent strain rate in each phase to the equivalent strain rate of the composite is expressed as

$$\chi_i = \frac{\dot{\gamma}_i}{\dot{\gamma}^*}, \quad (20)$$

where  $\dot{\gamma}_i$  and  $\dot{\gamma}^*$  are the equivalent shear strain rate in the  $i$ -th phase and the composite, respectively. A requirement that macroscopic fields are equal to the volume averages of the local fields leads to the self-consistency condition

$$\sum_{i=1}^N f_i \chi_i = 1, \quad (21)$$

where  $f_i = V_i/V$  is the volume fraction of  $i$ -th phase. The viscoplastic constitutive equations for each phase described by Stringfellow and Parks [209] lead to the set of equations

$$\chi_i = \frac{5}{3} + \frac{2s_i}{3s^*} \chi_i^{1/m}, \quad (22)$$

where  $s$  and  $s^*$  correspond to the reference shear strength of each phase and the composite.

The expressions in Eq. (22) together with the self-consistency condition in Eq. (21) yield a closed system of equations that needs to be solved for the unknowns  $\chi_i$  and  $s^*$ . In the current case,  $N=2$ , and the values for  $s_i$  correspond to the indentation yield strength of ferrite and pearlite constituents,  $\sigma_f$  and  $\sigma_p$ . A value of 0.01 was used for strain rate sensitivity,  $m$ . The values of  $f_p$  and  $f_f$  for Eq. (21) corresponded to values extracted in segmented images,  $v_p$  and  $v_f$ . Using the above information, we are interested in the unknown value of  $s^*$ , which, following the established notation, corresponds to the

composite yield strength,  $\sigma_{yc}$ . This value was recovered for each sample by solving the system of equations using a custom code in MATLAB [87].

#### 4.6.3 Results of composite model evaluation

All of the models described above were used to estimate the composite indentation yield strength based on the indentation yield strengths and volume fractions of the ferrite and pearlite constituents (these values are summarized in Table 11). To estimate the uncertainty in the composite yield strength predictions, the inputs (e.g., ferrite yield strength) to each model were randomly sampled from an assumed normal distribution of the experimental measurements. The resulting distribution of composite model predictions from 10,000 random samples was obtained and also assumed to follow a normal distribution. The results of the average and one standard deviation of estimated composite yield strength along with the actual yield strength from microindentation for each sample are summarized in Table 12.

**Table 12 – Indentation yield strength of pearlite-ferrite steel samples from microindentation measurements and the predicted indentation from composite models (average and one standard deviation). An average MAPE (mean absolute percentage error) between the indentation yield strength estimated by each composite model is displayed at the bottom.**

Sample	Microindentation $\sigma_{ind}$ (MPa)	ROM $\sigma_{yc}$ (MPa)	Modified ROM $\sigma_{yc}$ (MPa)	Stringfellow-Parks $\sigma_{yc}$ (MPa)
Unexposed	<b>614.5</b> ±18.6	673.3 ±45.5	536.6 ±30.9	640.4 ±36.7
Moderate exposure	<b>543.9</b> ±14.9	620.0 ±36.2	501.5 ±26.2	593.4 ±33.9
High exposure	<b>436.1</b> ±32.2	488.8 ±27.7	420.3 ±25.3	476.1 ±23.3
Average MAPE for each model		11.9%	8.0%	7.5%

The results of the composite models are evaluated against the experimentally measured microindentation yield strength. To evaluate the accuracy of the composite model, we define an error between average model estimates and the average experimental measurements, as

$$E(\sigma_{yc}, \sigma_{ind}) = \frac{100\%}{\sigma_{ind}} |\sigma_{yc} - \sigma_{ind}|, \quad (23)$$

where  $E(\sigma_{yc}, \sigma_{ind})$  denotes the mean absolute percentage error (MAPE) between the average indentation yield strength estimated by composite models,  $\sigma_{yc}$ , and the average yield strength measure with microindentation,  $\sigma_{ind}$ . The goal is to compare the relative percentage difference between the microindentation measurements and the model predictions.

The linear ROM model shows consistent overestimation of the composite yield strength compared with microindentation measurements, with an average MAPE of 11.9% for all samples estimates. This overestimation is somewhat expected because the linear ROM model theoretically provides an upper bound of composite properties. On the other hand, the modified ROM consistently underestimates the microindentation yield strength, with an average MAPE of 8.0%. On the average, the modified ROM provide estimates closer to the microindentation measurements than the linear ROM model. Finally, the estimates based on Stringfellow-Parks self-consistent model consistently overestimate the indentation yield strength. However, the average MAPE of 7.5% for this approach is lower than both rule of mixtures models.

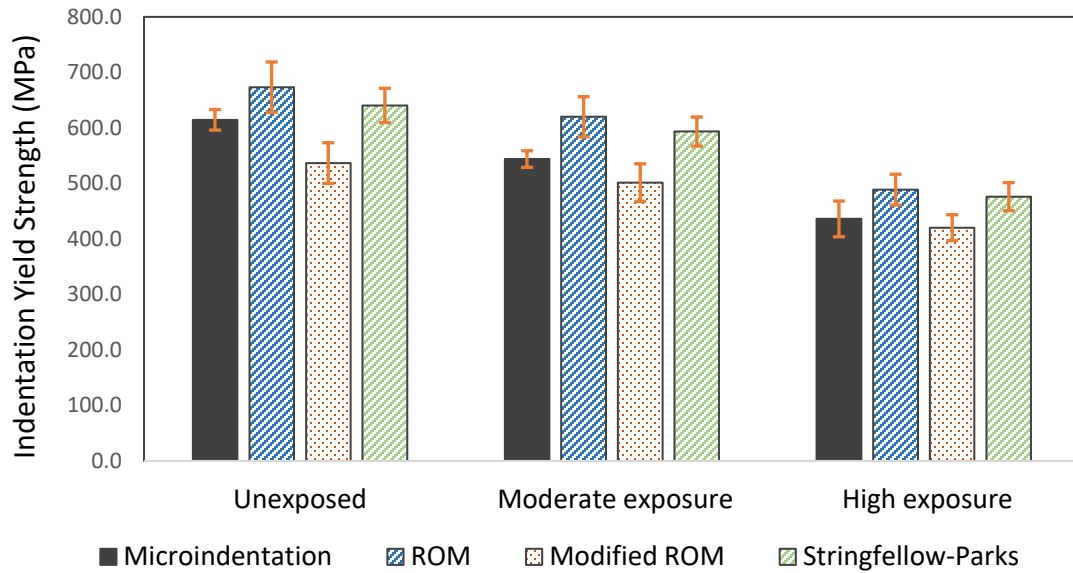


**Figure 29 – Comparison of indentation yield strength from evaluated composite models to the microindentation measurements.**

Overall, the estimates from the different approaches in this study envelop the actual composite yield strength measured with microindentation, as shown in a chart in Figure 29. The linear ROM model represents the simplest of the approaches and experiences the highest deviation from the experimental measurements. As more considerations are taken into account, the modified ROM and self-consistent models reduce the average error to experimental measurements. It is important to reiterate that these approaches utilize only the constituent volume fractions as a microstructure statistics input, yet it is remarkable that these models produce yield strength estimates close to the experimental measurements.

#### 4.7 Conclusions

This case study demonstrates an application of the developed protocols to evaluate microstructure and mechanical properties at multiple resolutions on thermally aged ferrite-

pearlite steels. The indentation yield strength of the ferrite and pearlite constituents, as well as the bulk yield strength of the samples was evaluated using indentation stress-strain protocols. On the other hand, image segmentation protocols were used to segment the ferrite and pearlite constituents in the sample microstructures images. All of the collected information was used to critically evaluate rule of mixture and self-consistent composite models to estimate the bulk indentation yield strength. These estimates produced good estimates, provided only volume fraction of constituents was used as the microstructure information input. Furthermore, the good estimates from the composite models validated that the developed protocols in this work can potentially be applied to collect large experimental datasets of microstructures and their properties to critically validate and/or refine the different composite theories. Although this study utilized composite models based on simple microstructure measures, the developed experimental protocols can be readily expanded to more elaborate composite models with higher fidelity predictions. For instance, the segmented images (of 2D and 3D image data) can be quantified using higher-order statistics (e.g., n-point statistics [187]) that are necessary in more detailed composite modeling approaches [191].

## CHAPTER 5. CONCLUSIONS

This dissertation develops and validates new protocols for systematic investigations of heterogeneous material microstructures and their mechanical responses at multiple resolutions. These protocols were demonstrated on a case study of ferrite-pearlite steels and have shown the potential to dramatically reduce the cost and effort needed for the multiresolution mechanical evaluation of heterogeneous material systems. The main conclusions of this work are summarized as follows:

- i. For the first time, microindentation was employed to mechanically evaluate scoop samples excised from operating industrial turbines components with various degrees of service exposure at elevated temperatures (up to 99,000 h of thermal aging). The indentations were performed on large number of grains to estimate the bulk material response. Indentation measurements revealed a trend of decreasing yield strength with increasing service time. It is also seen that the developed indentation protocols are able to provide reliable measurements in a high throughput manner. It is emphasized that there is no other practical alternative for extracting this critically needed information from scoop samples using conventional testing methods.
- ii. The elastic modulus and yield strength extracted using microindentation were in good agreement with available tensile tests on the same sample material. The yield strength ratio between the microindentation and tensile tests was observed to be about 2. This value is in excellent agreement with corresponding values reported in recent measurements on Al-6061 [50] as well as FE simulations [61].

- iii. Nanoindentation was used to locally evaluate yield strength within microscale ferrite and pearlite constituents in thermally aged ferrite-pearlite steels with significant amount of microstructural evolution (spheroidization and graphitization). These measurements revealed a trend of decreasing yield strength with increasing service time for both ferrite and pearlite, consistent to microindentation measurements on the same samples.
- iv. The developed segmentation framework addresses the challenges encountered in segmentation of raw microscopy images that are used for evaluation of microstructure statistics. In this work, a systematic framework was developed designed to segment a wide variety of microstructure images. The framework consists of five important sequential steps employing functions and tools that are widely available in popular software tools such as MATLAB and Python. The developed framework leads naturally to design and implementation of segmentation workflows (sequence of image processing functions/processes).
- v. The application of the developed framework was illustrated through the design and implementation of two types of segmentation workflows. The first workflow produced was a custom-built workflow utilizing all five framework steps to segment Ni-based superalloy images. In the second case, templated workflows were constructed and applied to previously acquired images of different material systems. Although the examples in this work illustrate segmentation of microstructure images with two local states (i.e., black and white), it is important to point out that the developed framework can be directly applied to segmentation of an arbitrary number of local states.

- vi. Following the framework, segmentation workflows were designed for the case study of ferrite-pearlite steel samples. Microstructure images were acquired using optical microscopy (OM) and from which ferrite, pearlite, and graphite constituents were segmented.
- vii. The bulk yield strengths of the samples from (i), the yield strengths of the microscale constituents from (iii), and the microstructure statistics of segmented images from (vi) were used to evaluate the composite theory estimates based on the simple rules of mixtures. It was shown that the multiresolution spherical indentation and image segmentation protocols employed in this work produce results that are highly consistent with the bounds estimated from the simplest of the composite theories.

## **5.1 Future Work**

The challenges in experimental multiresolution evaluation of microstructures and their properties present significant obstacles in the investigation of heterogeneous materials. This work provides a crucial step to overcome these challenges by developing protocols for evaluation of mechanical properties at multiple resolutions and a framework for microstructure image segmentation. One of the critical areas for future development is the automation of image segmentation. Modern characterization capabilities enable researchers to collect large amounts of raw microstructure images, which will demand segmentation automation. This can be approached by optimization of image processing functions and/or the set of functions within segmentation workflows. However, such optimization efforts remain a challenge due to the limited availability/access of calibration

data (e.g., segmentation ground truth, training data) in the materials science domain. Therefore, segmentation automation efforts largely rely on adoption/advancement of structured image segmentation frameworks, such as the one developed in this work, and broad collaboration in the material science community.

## REFERENCES

- [1] D. Gerbig, A. Srivastava, S. Osovski, L.G. Hector, A. Bower, Analysis and design of dual-phase steel microstructure for enhanced ductile fracture resistance, *International Journal of Fracture* 209(1-2) (2018) 3-26.
- [2] J. Allison, M. Li, C. Wolverson, X. Su, Virtual aluminum castings: an industrial application of ICME, *Jom* 58(11) (2006) 28-35.
- [3] X. Wu, M. Yang, F. Yuan, G. Wu, Y. Wei, X. Huang, Y. Zhu, Heterogeneous lamella structure unites ultrafine-grain strength with coarse-grain ductility, *Proceedings of the National Academy of Sciences* 112(47) (2015) 14501-14505.
- [4] W. Zhu, J. Lei, C. Tan, Q. Sun, W. Chen, L. Xiao, J. Sun, A novel high-strength  $\beta$ -Ti alloy with hierarchical distribution of  $\alpha$ -phase: the superior combination of strength and ductility, *Materials & Design* 168 (2019) 107640.
- [5] C.C. Tasan, M. Diehl, D. Yan, M. Bechtold, F. Roters, L. Schemmann, C. Zheng, N. Peranio, D. Ponge, M. Koyama, An overview of dual-phase steels: advances in microstructure-oriented processing and micromechanically guided design, *Annual Review of Materials Research* 45 (2015) 391-431.
- [6] G. Lütjering, Influence of processing on microstructure and mechanical properties of ( $\alpha$ +  $\beta$ ) titanium alloys, *Materials Science and Engineering: A* 243(1-2) (1998) 32-45.
- [7] Y. Murayama, S. Hanada, High temperature strength, fracture toughness and oxidation resistance of Nb–Si–Al–Ti multiphase alloys, *Science and Technology of Advanced Materials* 3(2) (2002) 145-156.
- [8] M.I. Latypov, S. Shin, B.C. De Cooman, H.S. Kim, Micromechanical finite element analysis of strain partitioning in multiphase medium manganese TWIP+ TRIP steel, *Acta Materialia* 108 (2016) 219-228.
- [9] J. Bian, H. Mohrbacher, J.-S. Zhang, Y.-T. Zhao, H.-Z. Lu, H. Dong, Application potential of high performance steels for weight reduction and efficiency increase in commercial vehicles, *Advances in Manufacturing* 3(1) (2015) 27-36.

- [10] W.J. Joost, Reducing vehicle weight and improving US energy efficiency using integrated computational materials engineering, *Jom* 64(9) (2012) 1032-1038.
- [11] M. Javidani, D. Larouche, Application of cast Al–Si alloys in internal combustion engine components, *International Materials Reviews* 59(3) (2014) 132-158.
- [12] C. Syn, D. Lesuer, O. Sherby, Influence of microstructure on tensile properties of spheroidized ultrahigh-carbon (1.8 Pct C steel, *Metallurgical and materials transactions A* 25(7) (1994) 1481-1493.
- [13] L. Schemmann, S. Zaeferrer, D. Raabe, F. Friedel, D. Mattissen, Alloying effects on microstructure formation of dual phase steels, *Acta Materialia* 95 (2015) 386-398.
- [14] A. Hüseyin, K.Z. Havva, K. Ceylan, Effect of intercritical annealing parameters on dual phase behavior of commercial low-alloyed steels, *Journal of Iron and Steel Research International* 17(4) (2010) 73-78.
- [15] Z. Pan, B. Gao, Q. Lai, X. Chen, Y. Cao, M. Liu, H. Zhou, Microstructure and mechanical properties of a cold-rolled ultrafine-grained dual-phase steel, *Materials* 11(8) (2018) 1399.
- [16] R. Hill, The elastic behaviour of a crystalline aggregate, *Proceedings of the Physical Society. Section A* 65(5) (1952) 349.
- [17] J.D. Eshelby, The determination of the elastic field of an ellipsoidal inclusion, and related problems, *Proceedings of the royal society of London. Series A. Mathematical and physical sciences* 241(1226) (1957) 376-396.
- [18] E. Kröner, Bounds for effective elastic moduli of disordered materials, *Journal of the Mechanics and Physics of Solids* 25(2) (1977) 137-155.
- [19] T. Mori, K. Tanaka, Average stress in matrix and average elastic energy of materials with misfitting inclusions, *Acta metallurgica* 21(5) (1973) 571-574.
- [20] S. Torquato, *Random heterogeneous materials: microstructure and macroscopic properties*, Springer 2002.
- [21] J. LLorca, C. González, J.M. Molina-Aldareguía, J. Segurado, R. Seltzer, F. Sket, M. Rodríguez, S. Sádaba, R. Muñoz, L.P. Canal, Multiscale modeling of composite materials: a roadmap towards virtual testing, *Advanced materials* 23(44) (2011) 5130-5147.
- [22] C. González, J. Vilatela, J. Molina-Aldareguía, C. Lopes, J. LLorca, Structural composites for multifunctional applications: Current challenges and future trends, *Progress in Materials Science* 89 (2017) 194-251.
- [23] J. Segurado, C. Gonzalez, J. Llorca, A numerical investigation of the effect of particle clustering on the mechanical properties of composites, *Acta materialia* 51(8) (2003) 2355-2369.

- [24] P.M. Suquet, Elements of homogenization for inelastic solid mechanics, Homogenization Techniques for Composite Media, Lecture notes in physics 272 (1985) 193.
- [25] S. Nemat-Nasser, M. Hori, Micromechanics: overall properties of heterogeneous materials, Elsevier 2013.
- [26] J. Segurado, J. Llorca, Simulation of the deformation of polycrystalline nanostructured Ti by computational homogenization, Computational Materials Science 76 (2013) 3-11.
- [27] K. Matouš, M.G. Geers, V.G. Kouznetsova, A. Gillman, A review of predictive nonlinear theories for multiscale modeling of heterogeneous materials, Journal of Computational Physics 330 (2017) 192-220.
- [28] S.R. Kalidindi, S. Pathak, Determination of the effective zero-point and the extraction of spherical nanoindentation stress-strain curves, Acta Materialia 56(14) (2008) 3523-3532.
- [29] H. Ghassemi-Armaki, R. Maaß, S. Bhat, S. Sriram, J. Greer, K. Kumar, Deformation response of ferrite and martensite in a dual-phase steel, Acta materialia 62 (2014) 197-211.
- [30] K. Kumar, K. Madhusoodanan, B. Rupani, Miniature specimen technique as an NDT tool for estimation of service life of operating pressure equipment, International Conference & Exhibition on Pressure Vessel and Piping, Citeseer, 2006.
- [31] K. Kumar, A. Pooleery, K. Madhusoodanan, R. Singh, J. Chakravartty, B. Dutta, R. Sinha, Use of miniature tensile specimen for measurement of mechanical properties, Procedia Engineering 86 (2014) 899-909.
- [32] E. ASTM, 8M. Standard test methods of tension testing of metallic materials [metric], Annual book of ASTM standards, 2003.
- [33] E. ASTM, E9-89a, standard test methods of compression testing of metallic materials at room temperature, Annual Book of ASTM Standards 3 (2000) 1-9.
- [34] H. Bei, S. Shim, G.M. Pharr, E.P. George, Effects of pre-strain on the compressive stress-strain response of Mo-alloy single-crystal micropillars, Acta Materialia 56(17) (2008) 4762-4770.
- [35] W.C. Oliver, G.M. Pharr, An improved technique for determining hardness and elastic modulus using load and displacement sensing indentation experiments, Journal of materials research 7(06) (1992) 1564-1583.
- [36] D. Tabor, A simple theory of static and dynamic hardness, Proceedings of the Royal Society of London A: Mathematical, Physical and Engineering Sciences, The Royal Society, 1948, pp. 247-274.
- [37] H. O'Neill, Hardness measurement of metals and alloys, Chapman & Hall 1967.

- [38] Y. Tirupataiah, G. Sundararajan, On the constraint factor associated with the indentation of work-hardening materials with a spherical ball, *Metallurgical Transactions A* 22(10) (1991) 2375-2384.
- [39] R. Rodriguez, I. Gutierrez, Correlation between nanoindentation and tensile properties: influence of the indentation size effect, *Materials Science and Engineering: A* 361(1-2) (2003) 377-384.
- [40] P. Zhang, S. Li, Z. Zhang, General relationship between strength and hardness, *Materials Science and Engineering: A* 529 (2011) 62-73.
- [41] G.M. Pharr, E.G. Herbert, Y. Gao, The indentation size effect: a critical examination of experimental observations and mechanistic interpretations, *Annual Review of Materials Research* 40 (2010) 271-292.
- [42] W.D. Nix, H. Gao, Indentation size effects in crystalline materials: a law for strain gradient plasticity, *Journal of the Mechanics and Physics of Solids* 46(3) (1998) 411-425.
- [43] J. Swadener, E. George, G. Pharr, The correlation of the indentation size effect measured with indenters of various shapes, *Journal of the Mechanics and Physics of Solids* 50(4) (2002) 681-694.
- [44] S. Pathak, S.R. Kalidindi, C. Klemenz, N. Orlovskaya, Analyzing indentation stress-strain response of LaGaO<sub>3</sub> single crystals using spherical indenters, *Journal of the European Ceramic Society* 28(11) (2008) 2213-2220.
- [45] S. Pathak, D. Stojakovic, S.R. Kalidindi, Measurement of the local mechanical properties in polycrystalline samples using spherical nanoindentation and orientation imaging microscopy, *Acta Materialia* 57(10) (2009) 3020-3028.
- [46] S. Pathak, J. Shaffer, S.R. Kalidindi, Determination of an effective zero-point and extraction of indentation stress-strain curves without the continuous stiffness measurement signal, *Scripta Materialia* 60(6) (2009) 439-442.
- [47] S. Pathak, J. Michler, K. Wasmer, S.R. Kalidindi, Studying grain boundary regions in polycrystalline materials using spherical nano-indentation and orientation imaging microscopy, *Journal of Materials Science* 47(2) (2012) 815-823.
- [48] S.J. Vachhani, S.R. Kalidindi, Grain-scale measurement of slip resistances in aluminum polycrystals using spherical nanoindentation, *Acta Materialia* 90 (2015) 27-36.
- [49] J.S. Weaver, S.R. Kalidindi, Mechanical characterization of Ti-6Al-4V titanium alloy at multiple length scales using spherical indentation stress-strain measurements, *Materials & Design* 111 (2016) 463-472.
- [50] J.S. Weaver, A. Khosravani, A. Castillo, S.R. Kalidindi, High throughput exploration of process-property linkages in Al-6061 using instrumented spherical microindentation and

microstructurally graded samples, *Integrating Materials and Manufacturing Innovation* 5(1) (2016) 1-20.

[51] J.S. Weaver, M.W. Priddy, D.L. McDowell, S.R. Kalidindi, On capturing the grain-scale elastic and plastic anisotropy of alpha-Ti with spherical nanoindentation and electron back-scattered diffraction, *Acta Materialia* 117 (2016) 23-34.

[52] S. Pathak, S.R. Kalidindi, N.A. Mara, Investigations of orientation and length scale effects on micromechanical responses in polycrystalline zirconium using spherical nanoindentation, *Scripta Materialia* 113 (2016) 241-245.

[53] S.J. Vachhani, R.D. Doherty, S.R. Kalidindi, Studies of grain boundary regions in deformed polycrystalline aluminum using spherical nanoindentation, *International Journal of Plasticity* 81 (2016) 87-101.

[54] J. Weaver, E. Aydogan, N.A. Mara, S.A. Maloy, Nanoindentation of Electropolished FeCrAl Alloy Welds, Los Alamos National Laboratory (LANL), 2017.

[55] A. Khosravani, C.M. Caliendo, S.R. Kalidindi, New Insights into the Microstructural Changes During the Processing of Dual-Phase Steels from Multiresolution Spherical Indentation Stress–Strain Protocols, *Metals* 10(1) (2020) 18.

[56] A. Khosravani, A. Cecen, S.R. Kalidindi, Development of high throughput assays for establishing process-structure-property linkages in multiphase polycrystalline metals: Application to dual-phase steels, *Acta Mater.* 123 (2017) 55-69.

[57] A. Iskakov, Y.C. Yabansu, S. Rajagopalan, A. Kapustina, S.R. Kalidindi, Application of spherical indentation and the materials knowledge system framework to establishing microstructure-yield strength linkages from carbon steel scoops excised from high-temperature exposed components, *Acta Materialia* 144 (2018) 758-767.

[58] A. Khosravani, L. Morsdorf, C.C. Tasan, S.R. Kalidindi, Multiresolution mechanical characterization of hierarchical materials: Spherical nanoindentation on martensitic Fe-Ni-C steels, *Acta Materialia* 153 (2018) 257-269.

[59] A. Bhat, R. Neu, On the Constraint Factor Relating Uniaxial and Indentation Yield Strength of Polycrystalline Materials Using Spherical Microindentation, *Materials Performance and Characterization* 9(1) (2020) 324-345.

[60] B.R. Donohue, A. Ambrus, S.R. Kalidindi, Critical evaluation of the indentation data analyses methods for the extraction of isotropic uniaxial mechanical properties using finite element models, *Acta Materialia* 60(9) (2012) 3943-3952.

[61] D.K. Patel, S.R. Kalidindi, Correlation of spherical nanoindentation stress-strain curves to simple compression stress-strain curves for elastic-plastic isotropic materials using finite element models, *Acta Materialia* 112 (2016) 295-302.

- [62] J. Fry, Galaxy N-point correlation functions-Theoretical amplitudes for arbitrary N, *The Astrophysical Journal* 277 (1984) L5-L8.
- [63] A. Moore, A. Connolly, C. Genovese, A. Gray, L. Grone, N. Kanidoris II, R. Nichol, J. Schneider, A. Szalay, I. Szapudi, Fast algorithms and efficient statistics: N-point correlation functions, *Mining the Sky* (2001) 71-82.
- [64] T. Smith, P. Bonacuse, J. Sosa, M. Kulis, L. Evans, A quantifiable and automated volume fraction characterization technique for secondary and tertiary  $\gamma'$  precipitates in Ni-based superalloys, *Materials Characterization* 140 (2018) 86-94.
- [65] M. Santofimia, L. Zhao, R. Petrov, J. Sietsma, Characterization of the microstructure obtained by the quenching and partitioning process in a low-carbon steel, *Materials Characterization* 59(12) (2008) 1758-1764.
- [66] C.A. Paredes-Orta, J.D. Mendiola-Santibañez, F. Manriquez-Guerrero, I.R. Terol-Villalobos, Method for grain size determination in carbon steels based on the ultimate opening, *Measurement* 133 (2019) 193-207.
- [67] E. Payton, P. Phillips, M. Mills, Semi-automated characterization of the  $\gamma'$  phase in Ni-based superalloys via high-resolution backscatter imaging, *Materials Science and Engineering: A* 527(10-11) (2010) 2684-2692.
- [68] A. Campbell, P. Murray, E. Yakushina, S. Marshall, W. Ion, New methods for automatic quantification of microstructural features using digital image processing, *Materials & Design* 141 (2018) 395-406.
- [69] J.R. Foulds, J.P. Shingledecker, An Updated Assessment of Graphitization of Steels in Elevated Temperature Service, *Journal of Materials Engineering and Performance* 24(2) (2015) 586-597.
- [70] J.R. Foulds, R. Viswanathan, Graphitization of steels in elevated-temperature service, *Journal of Materials Engineering and Performance* 10(4) (2001) 484-492.
- [71] K. Kruger, P. Pistorius, C. Orsmond, Repair welding of carbon steel that has been partially graphitized during service, *Welding in the World* 61(4) (2017) 703-710.
- [72] G. Pantazopoulos, A. Toulfatzis, A. Vazdirvanidis, A. Rikos, Analysis of the Degradation Process of Structural Steel Component Subjected to Prolonged Thermal Exposure, *Metallography, Microstructure, and Analysis* 5(2) (2016) 149-156.
- [73] I.U. Pérez, T.L. da Silveira, T.F. da Silveira, H.C. Furtado, Graphitization in Low Alloy Steel Pressure Vessels and Piping, *Journal of Failure Analysis and Prevention* 11(1) (2011) 3-9.
- [74] S. Pathak, S.R. Kalidindi, Spherical nanoindentation stress-strain curves, *Mater. Sci. Eng. R* 91 (2015) 1-36.

- [75] X. Gong, S. Mohan, M. Mendoza, A. Gray, P. Collins, S. Kalidindi, High throughput assays for additively manufactured Ti-Ni alloys based on compositional gradients and spherical indentation, *Integrating Materials and Manufacturing Innovation* 6(3) (2017) 218-228.
- [76] S. Parvinian, Y.C. Yabansu, A. Khosravani, H. Garmestani, S.R. Kalidindi, High-Throughput Exploration of the Process Space in 18% Ni (350) Maraging Steels via Spherical Indentation Stress–Strain Protocols and Gaussian Process Models, *Integrating Materials and Manufacturing Innovation* 9(3) (2020) 199-212.
- [77] N. Millan Espitia, S. Mohan, A.L. Pilchak, S.R. Kalidindi, Spherical nanoindentation stress-strain curves of primary- $\alpha$  grains in Ti5-2.5, Ti811, Ti64, Ti6242 and Ti6246 alloys, (2020).
- [78] S.R. Kalidindi, S.J. Vachhani, Mechanical characterization of grain boundaries using nanoindentation, *Current Opinion in Solid State and Materials Science* 18(4) (2014) 196-204.
- [79] H. Hertz, D. Jones, G. Schott, *Miscellaneous Papers*, Macmillan, New York 1896.
- [80] A. Okamoto, Graphite formation in high-purity cold-rolled carbon steels, *Metallurgical and Materials Transactions A* 20(10) (1989) 1917-1925.
- [81] J. Hau, A. Seijas, T. Munsterman, A. Mayorga, Evaluation of Aging Equipment for Continued Service, *Corrosion 2005*, Paper 05558, NACE International, Houston, USA, 2005.
- [82] T. Bierdel, P. Bullinger, T. Hagedorn, *Life Cycle Value for combined cycle power plants*, Siemens AG, 2013.
- [83] K.L. Johnson, *Contact Mechanics*, Cambridge University Press 1987.
- [84] W. Yu, J.P. Blanchard, An elastic-plastic indentation model and its solutions, *Journal of Materials Research* 11(09) (1996) 2358-2367.
- [85] J. Alcalá, D. Esqué-de los Ojos, Reassessing spherical indentation: Contact regimes and mechanical property extractions, *International journal of solids and structures* 47(20) (2010) 2714-2732.
- [86] F. Perez, B.E. Granger, J.D. Hunter, Python: an ecosystem for scientific computing, *Computing in Science & Engineering* 13(2) (2011) 13-21.
- [87] D.J. Higham, N.J. Higham, *MATLAB guide*, Siam, Philadelphia, 2016.
- [88] M.D. Uchic, M.A. Groeber, D.M. Dimiduk, J. Simmons, 3D microstructural characterization of nickel superalloys via serial-sectioning using a dual beam FIB-SEM, *Scripta Materialia* 55(1) (2006) 23-28.

- [89] B. Cantor, I. Chang, P. Knight, A. Vincent, Microstructural development in equiatomic multicomponent alloys, *Materials Science and Engineering: A* 375 (2004) 213-218.
- [90] F. Otto, A. Dlouhý, K.G. Pradeep, M. Kuběnová, D. Raabe, G. Eggeler, E.P. George, Decomposition of the single-phase high-entropy alloy CrMnFeCoNi after prolonged anneals at intermediate temperatures, *Acta Materialia* 112 (2016) 40-52.
- [91] C. Tan, K. Zhou, W. Ma, P. Zhang, M. Liu, T. Kuang, Microstructural evolution, nanoprecipitation behavior and mechanical properties of selective laser melted high-performance grade 300 maraging steel, *Materials & Design* 134 (2017) 23-34.
- [92] S. Morito, X. Huang, T. Furuhashi, T. Maki, N. Hansen, The morphology and crystallography of lath martensite in alloy steels, *Acta Materialia* 54(19) (2006) 5323-5331.
- [93] I.B. Timokhina, P.D. Hodgson, E. Pereloma, Transmission electron microscopy characterization of the bake-hardening behavior of transformation-induced plasticity and dual-phase steels, *Metallurgical and Materials Transactions A* 38(10) (2007) 2442-2454.
- [94] M. Sarvghad-Moghaddam, R. Parvizi, A. Davoodi, M. Haddad-Sabzevar, A. Imani, Establishing a correlation between interfacial microstructures and corrosion initiation sites in Al/Cu joints by SEM-EDS and AFM-SKPFM, *Corrosion science* 79 (2014) 148-158.
- [95] T. Hu, H. Shi, D. Hou, T. Wei, S. Fan, F. Liu, E.-H. Han, A localized approach to study corrosion inhibition of intermetallic phases of AA 2024-T3 by cerium malate, *Applied Surface Science* 467 (2019) 1011-1032.
- [96] D. Li, Q. Guo, S. Guo, H. Peng, Z. Wu, The microstructure evolution and nucleation mechanisms of dynamic recrystallization in hot-deformed Inconel 625 superalloy, *Materials & Design* 32(2) (2011) 696-705.
- [97] P.C. Collins, B. Welk, T. Searles, J. Tiley, J. Russ, H. Fraser, Development of methods for the quantification of microstructural features in  $\alpha + \beta$ -processed  $\alpha/\beta$  titanium alloys, *Materials Science and Engineering: A* 508(1-2) (2009) 174-182.
- [98] J. Tiley, S. Kim, T. Parthasarathy, G. Loughnane, R. Kublik, A. Salem, Quantifying the effect of microstructure variability on the yield strength predictions of Ni-base superalloys, *Materials Science and Engineering: A* 685 (2017) 178-186.
- [99] H. Peregrina-Barreto, I. Terol-Villalobos, J. Rangel-Magdaleno, A. Herrera-Navarro, L. Morales-Hernández, F. Manríquez-Guerrero, Automatic grain size determination in microstructures using image processing, *Measurement* 46(1) (2013) 249-258.
- [100] A. Cecen, E. Wargo, A. Hanna, D. Turner, S. Kalidindi, E. Kumbur, 3-D microstructure analysis of fuel cell materials: spatial distributions of tortuosity, void size and diffusivity, *Journal of The Electrochemical Society* 159(3) (2012) B299-B307.

- [101] D. Yang, Z. Liu, Quantification of microstructural features and prediction of mechanical properties of a dual-phase Ti-6Al-4V alloy, *Materials* 9(8) (2016) 628.
- [102] W. Zhou, R. Apkarian, Z.L. Wang, D. Joy, *Fundamentals of scanning electron microscopy (SEM)*, Scanning microscopy for nanotechnology, Springer, New York, 2006, pp. 1-40.
- [103] A. Behrooz, J.-C. Tseng, J. Meganck, M. Hopkinton, *Image Resolution in Micro-CT: Principles and Characterization of the Quantum FX and Quantum GX System*, 2016.
- [104] T. Ishitani, C. Kamiya, M. Sato, Influence of random noise on the contrast-to-gradient image resolution in scanning electron microscopy, *Journal of electron microscopy* 54(2) (2005) 85-97.
- [105] J.F. Barrett, N. Keat, Artifacts in CT: recognition and avoidance, *Radiographics* 24(6) (2004) 1679-1691.
- [106] Y.C. Yabansu, P. Steinmetz, J. Hötzer, S.R. Kalidindi, B. Nestler, Extraction of reduced-order process-structure linkages from phase-field simulations, *Acta Materialia* 124 (2017) 182-194.
- [107] D.M. de Oca Zapiain, E. Popova, F. Abdeljawad, J.W. Foulk, S.R. Kalidindi, H. Lim, Reduced-Order Microstructure-Sensitive Models for Damage Initiation in Two-Phase Composites, *Integrating Materials and Manufacturing Innovation* 7(3) (2018) 97-115.
- [108] M.I. Latypov, S.R. Kalidindi, Data-driven reduced order models for effective yield strength and partitioning of strain in multiphase materials, *Journal of Computational Physics* 346 (2017) 242-261.
- [109] N.H. Paulson, M.W. Priddy, D.L. McDowell, S.R. Kalidindi, Reduced-order structure-property linkages for polycrystalline microstructures based on 2-point statistics, *Acta Materialia* 129 (2017) 428-438.
- [110] J.M. Sosa, D.E. Huber, B. Welk, H.L. Fraser, Development and application of MIPAR™: a novel software package for two-and three-dimensional microstructural characterization, *Integrating Materials and Manufacturing Innovation* 3(1) (2014) 123–140.
- [111] M. Jackson, *EM/MPM*, Dayton, OH: BlueQuartz Software ([http://www.bluequartz.net/projects/EIM\\_Segmentation/](http://www.bluequartz.net/projects/EIM_Segmentation/)) (2014).
- [112] N. Otsu, A threshold selection method from gray-level histograms, *IEEE transactions on systems, man, and cybernetics* 9(1) (1979) 62-66.
- [113] D. Bradley, G. Roth, Adaptive thresholding using the integral image, *Journal of graphics tools* 12(2) (2007) 13-21.

- [114] E.R. Davies, Computer and machine vision: theory, algorithms, practicalities, Academic Press 2012.
- [115] P. Soille, Morphological image analysis: principles and applications, Springer Science & Business Media 2013.
- [116] L. Shapiro, Computer vision and image processing, Academic Press 1992.
- [117] K. Zuiderveld, Contrast limited adaptive histogram equalization, Graphics gems IV, Academic Press Professional, Inc., San Diego, CA, USA, 1994, pp. 474-485.
- [118] S. Deshpande, A. Kulkarni, S. Sampath, H. Herman, Application of image analysis for characterization of porosity in thermal spray coatings and correlation with small angle neutron scattering, Surface and coatings technology 187(1) (2004) 6-16.
- [119] K. Surekha, B. Murty, K.P. Rao, Microstructural characterization and corrosion behavior of multipass friction stir processed AA2219 aluminium alloy, Surface and Coatings Technology 202(17) (2008) 4057-4068.
- [120] J. Liu, C. Li, J. Liu, G. Cui, Z. Yang, Study On 3D Spatial Distribution Of Steel Fibers In Fiber Reinforced Cementitious Composites Through Micro-CT Technique, Construction and Building Materials 48 (2013) 656-661.
- [121] M. Saadatfar, F. Garcia-Moreno, S. Hutzler, A. Sheppard, M. Knackstedt, J. Banhart, D. Weaire, Imaging of metallic foams using X-ray micro-CT, Colloids and Surfaces A: Physicochemical and Engineering Aspects 344(1-3) (2009) 107-112.
- [122] S. Gigan, Optical microscopy aims deep, Nature Photonics 11(1) (2017) 14-16.
- [123] H.-J. Butt, B. Cappella, M. Kappl, Force measurements with the atomic force microscope: Technique, interpretation and applications, Surface Science Reports 59(1-6) (2005) 1-152.
- [124] T. Wortmann, Fusion of AFM and SEM Scans, 2009 International Symposium on Optomechatronic Technologies, IEEE, Istanbul, Turkey, 2009, pp. 40-45.
- [125] S.R. Kalidindi, Hierarchical materials informatics: novel analytics for materials data, Elsevier 2015.
- [126] S.R. Niezgoda, D.M. Turner, D.T. Fullwood, S.R. Kalidindi, Optimized structure based representative volume element sets reflecting the ensemble-averaged 2-point statistics, Acta Materialia 58(13) (2010) 4432-4445.
- [127] C.-Y. Chen, R. Klette, Image stitching—Comparisons and new techniques, International Conference on Computer Analysis of Images and Patterns, Springer, 1999, pp. 615-622.

- [128] B. Ma, T. Zimmermann, M. Rohde, S. Winkelbach, F. He, W. Lindenmaier, K.E. Dittmar, Use of autostitch for automatic stitching of microscope images, *Micron* 38(5) (2007) 492-499.
- [129] J. Juntu, J. Sijbers, D. Van Dyck, J. Gielen, Bias field correction for MRI images, *Computer Recognition Systems*, Springer2005, pp. 543-551.
- [130] B. Likar, J.a. Maintz, M.A. Viergever, F. Pernus, Retrospective shading correction based on entropy minimization, *Journal of Microscopy* 197(Pt 3) (2000) 285-295.
- [131] R.A. Peters, A new algorithm for image noise reduction using mathematical morphology, *IEEE transactions on Image Processing* 4(5) (1995) 554-568.
- [132] M.V. Sarode, P.R. Deshmukh, Reduction of speckle noise and image enhancement of images using filtering technique, *International Journal of Advancements in Technology* 2(1) (2011) 30-38.
- [133] D. Van De Ville, M. Nachtegael, D. Van der Weken, E.E. Kerre, W. Philips, I. Lemahieu, Noise reduction by fuzzy image filtering, *IEEE transactions on fuzzy systems* 11(4) (2003) 429-436.
- [134] R. Verma, J. Ali, A comparative study of various types of image noise and efficient noise removal techniques, *International Journal of advanced research in computer science and software engineering* 3(10) (2013) 617-622.
- [135] C. Tomasi, R. Manduchi, Bilateral filtering for gray and color images, *Proceedings of the 1998 IEEE International Conference on Computer Vision*, Bombay, India, 1998, p. 2.
- [136] J.S. Lim, *Two-dimensional signal and image processing*, Prentice Hall, Englewood Cliffs, NJ, 1990, pp. 469-476.
- [137] A.C. Bovik, T.S. Huang, D.C. Munson, The effect of median filtering on edge estimation and detection, *IEEE Transactions on Pattern Analysis and Machine Intelligence* (2) (1987) 181-194.
- [138] M.H. Alkinani, M.R. El-Sakka, Patch-based models and algorithms for image denoising: a comparative review between patch-based images denoising methods for additive noise reduction, *EURASIP Journal on Image and Video Processing* (1) (2017) 1-27.
- [139] A. Buades, B. Coll, J.-M. Morel, A non-local algorithm for image denoising, 2005 *IEEE Computer Society Conference on Computer Vision and Pattern Recognition (CVPR'05)*, IEEE, 2005, pp. 60-65.
- [140] P. Chatterjee, P. Milanfar, Patch-based near-optimal image denoising, *IEEE Transactions on Image Processing* 21(4) (2011) 1635-1649.

- [141] C. Kervrann, J. Boulanger, Optimal spatial adaptation for patch-based image denoising, *IEEE Transactions on Image Processing* 15(10) (2006) 2866-2878.
- [142] L. Zhang, W. Dong, D. Zhang, G. Shi, Two-stage image denoising by principal component analysis with local pixel grouping, *Pattern recognition* 43(4) (2010) 1531-1549.
- [143] K. Dabov, A. Foi, V. Katkovnik, K. Egiazarian, Image denoising by sparse 3-D transform-domain collaborative filtering, *IEEE Transactions on image processing* 16(8) (2007) 2080-2095.
- [144] C.-A. Deledalle, L. Denis, F. Tupin, Iterative weighted maximum likelihood denoising with probabilistic patch-based weights, *IEEE Transactions on Image Processing* 18(12) (2009) 2661-2672.
- [145] S. Van der Walt, J.L. Schönberger, J. Nunez-Iglesias, F. Boulogne, J.D. Warner, N. Yager, E. Gouillart, T. Yu, scikit-image: image processing in Python, *PeerJ* 2 (2014) e453.
- [146] A.K. Jain, *Fundamentals of digital image processing*, Prentice Hall, Englewood Cliffs, NJ, 1989.
- [147] R.C. Gonzalez, R.E. Woods, *Digital image processing*, 2 ed., Prentice-Hall, Englewood Cliffs, NJ, 2002.
- [148] S. Dutta, K. Barat, A. Das, S.K. Das, A. Shukla, H. Roy, Characterization of micrographs and fractographs of Cu-strengthened HSLA steel using image texture analysis, *Measurement* 47 (2014) 130-144.
- [149] S. Gupta, A. Panda, R. Naskar, D.K. Mishra, S. Pal, Processing and refinement of steel microstructure images for assisting in computerized heat treatment of plain carbon steel, *Journal of Electronic Imaging* 26(6) (2017) 063010.
- [150] J.P. Papa, V.H.C. De Albuquerque, A.X. Falcão, J.M.R. Tavares, Fast automatic microstructural segmentation of ferrous alloy samples using optimum-path forest, *International Symposium Computational Modeling of Objects Represented in Images*, Springer, Berlin, Heidelberg, 2010, pp. 210-220.
- [151] K.H. Moon, A.C. Falchetto, J.H. Jeong, Microstructural analysis of asphalt mixtures using digital image processing techniques, *Canadian Journal of Civil Engineering* 41(1) (2013) 74-86.
- [152] B. Shafei, G. Steidl, Segmentation of images with separating layers by fuzzy c-means and convex optimization, *Journal of visual communication and image representation* 23(4) (2012) 611-621.
- [153] J.N. Kapur, P.K. Sahoo, A.K. Wong, A new method for gray-level picture thresholding using the entropy of the histogram, *Computer vision, graphics, and image processing* 29(3) (1985) 273-285.

- [154] T. Kurita, N. Otsu, N. Abdelmalek, Maximum likelihood thresholding based on population mixture models, *Pattern recognition* 25(10) (1992) 1231-1240.
- [155] D.-M. Tsai, Y.-H. Chen, A fast histogram-clustering approach for multi-level thresholding, *Pattern Recognition Letters* 13(4) (1992) 245-252.
- [156] J.R. Parker, *Algorithms for image processing and computer vision*, John Wiley & Sons 2010.
- [157] J. Canny, A computational approach to edge detection, *Readings in computer vision*, Elsevier 1987, pp. 184-203.
- [158] J. Serra, *Image Analysis and Math. Morphology*, Academic Press, 1982.
- [159] Y. Han, C. Lai, B. Wang, H. Gu, Segmenting images with complex textures by using hybrid algorithm, *Journal of Electronic Imaging* 28(1) (2019) 013030.
- [160] M. Paulic, D. Mocnik, M. Ficko, J. Balic, T. Irgolic, S. Klancnik, Intelligent system for prediction of mechanical properties of material based on metallographic images, *Tehnički vjesnik* 22(6) (2015) 1419-1424.
- [161] A.S.f. Testing, *Materials*, ASTM E562-11: standard test method for determining volume fraction by systematic manual point count, ASTM, 2011.
- [162] T. Klein, M. Schachermayer, F. Mendez-Martin, T. Schöberl, B. Rashkova, H. Clemens, S. Mayer, Carbon distribution in multi-phase  $\gamma$ -TiAl based alloys and its influence on mechanical properties and phase formation, *Acta Materialia* 94 (2015) 205-213.
- [163] J. Potgieter, M. Cortie, Determination of the microstructure and alloy element distribution in experimental duplex stainless steels, *Materials characterization* 26(3) (1991) 155-165.
- [164] C. Joseph, C. Persson, M.H. Colliander, Influence of heat treatment on the microstructure and tensile properties of Ni-base superalloy Haynes 282, *Materials Science and Engineering: A* 679 (2017) 520-530.
- [165] G. Melenka, A. Hunt, J. van Ravenhorst, R. Akkerman, C. Pastore, F. Ko, M. Munro, J. Carey, Manufacturing processes for braided composite materials, *Handbook of Advances in Braided Composite Materials*, Elsevier 2017, pp. 47-153.
- [166] A. Standard, E112, "Standard Test Method for Determining Average Grain Size," ASTM International, West Conshohocken, PA, 2010, DOI: 10.1520/E0112-10, 2013.
- [167] A. Standard, E2567-13a, 2013, "Standard Test Method for Determining Nodularity And Nodule Count In Ductile Iron". ASTM Internationals, West Conshohocken, PA, 2013, DOI: 10.1520/E2567-13A.

- [168] D. Fullwood, S. Kalidindi, S. Niezgod, A. Fast, N. Hampson, Gradient-based microstructure reconstructions from distributions using fast Fourier transforms, *Materials Science and Engineering: A* 494(1-2) (2008) 68-72.
- [169] S. Niezgod, D. Fullwood, S. Kalidindi, Delineation of the space of 2-point correlations in a composite material system, *Acta Materialia* 56(18) (2008) 5285-5292.
- [170] D.M. Turner, S.R. Kalidindi, Statistical construction of 3-D microstructures from 2-D exemplars collected on oblique sections, *Acta Materialia* 102 (2016) 136-148.
- [171] Y. Jiao, F. Stillinger, S. Torquato, A superior descriptor of random textures and its predictive capacity, *Proceedings of the National Academy of Sciences* 106(42) (2009) 17634-17639.
- [172] S. Torquato, B. Lu, Chord-length distribution function for two-phase random media, *Physical Review E* 47(4) (1993) 2950.
- [173] Y. Jiao, F. Stillinger, S. Torquato, Modeling heterogeneous materials via two-point correlation functions: Basic principles, *Physical review E* 76(3) (2007) 031110.
- [174] J.G. Berryman, S.C. Blair, Use of digital image analysis to estimate fluid permeability of porous materials: Application of two-point correlation functions, *Journal of applied Physics* 60(6) (1986) 1930-1938.
- [175] R. Kozar, A. Suzuki, W. Milligan, J. Schirra, M. Savage, T. Pollock, Strengthening mechanisms in polycrystalline multimodal nickel-base superalloys, *Metallurgical and Materials Transactions A* 40(7) (2009) 1588-1603.
- [176] E. Francis, B. Grant, J.Q. da Fonseca, P. Phillips, M. Mills, M. Daymond, M. Preuss, High-temperature deformation mechanisms in a polycrystalline nickel-base superalloy studied by neutron diffraction and electron microscopy, *Acta Materialia* 74 (2014) 18-29.
- [177] R. Unocic, L. Kovarik, C. Shen, P. Sarosi, Y. Wang, J. Li, S. Ghosh, M. Mills, Deformation mechanisms in Ni-base disk superalloys at higher temperatures, *Superalloys* 8 (2008) 377.
- [178] A. Marder, B. Bramfitt, The effect of morphology on the strength of pearlite, *Metallurgical Transactions A* 7(3) (1976) 365-372.
- [179] E. ASTM, Standard guide for electrolytic polishing of metallographic specimens, (2009).
- [180] A. Molinari, G. Canova, S. Ahzi, A self consistent approach of the large deformation polycrystal viscoplasticity, *Acta Metallurgica* 35(12) (1987) 2983-2994.
- [181] R.A. Lebensohn, C. Tomé, A self-consistent anisotropic approach for the simulation of plastic deformation and texture development of polycrystals: application to zirconium alloys, *Acta metallurgica et materialia* 41(9) (1993) 2611-2624.

- [182] C.N. Tomé, Self-consistent polycrystal models: a directional compliance criterion to describe grain interactions, *Modelling and Simulation in Materials Science and Engineering* 7(5) (1999) 723.
- [183] M.V. Nebozhyn, P. Gilormini, P.P. Castañeda, Variational self-consistent estimates for cubic viscoplastic polycrystals: the effects of grain anisotropy and shape, *Journal of the Mechanics and Physics of Solids* 49(2) (2001) 313-340.
- [184] W.F. Brown Jr, Solid mixture permittivities, *The Journal of Chemical Physics* 23(8) (1955) 1514-1517.
- [185] E. Kröner, *Statistical continuum mechanics*, Springer 1972.
- [186] S. Torquato, *Random heterogeneous media: microstructure and improved bounds on effective properties*, (1991).
- [187] S. Torquato, G. Stell, Microstructure of two-phase random media. I. The n-point probability functions, *The Journal of Chemical Physics* 77(4) (1982) 2071-2077.
- [188] B.L. Adams, T. Olson, The mesostructure—properties linkage in polycrystals, *Progress in Materials Science* 43(1) (1998) 1-87.
- [189] H. Garmestani, S. Lin, B. Adams, Statistical continuum theory for inelastic behavior of a two-phase medium, *International Journal of Plasticity* 14(8) (1998) 719-731.
- [190] B.L. Adams, X. Gao, S.R. Kalidindi, Finite approximations to the second-order properties closure in single phase polycrystals, *Acta Materialia* 53(13) (2005) 3563-3577.
- [191] S. Torquato, *Random heterogeneous materials: microstructure and macroscopic properties*, Springer Science & Business Media 2013.
- [192] B.L. Adams, S.R. Kalidindi, D.T. Fullwood, *Microstructure Sensitive Design for Performance Optimization*, Elsevier Science 2012.
- [193] S. Ghosh, K. Lee, S. Moorthy, Multiple scale analysis of heterogeneous elastic structures using homogenization theory and Voronoi cell finite element method, *International Journal of Solids and Structures* 32(1) (1995) 27-62.
- [194] P. Gilormini, Y. Germain, A finite element analysis of the inclusion problem for power law viscous materials, *International journal of solids and structures* 23(3) (1987) 413-437.
- [195] J. Segurado, J. Llorca, A numerical approximation to the elastic properties of sphere-reinforced composites, *Journal of the Mechanics and Physics of Solids* 50(10) (2002) 2107-2121.

- [196] M.G. Geers, V.G. Kouznetsova, W. Brekelmans, Multi-scale computational homogenization: Trends and challenges, *Journal of computational and applied mathematics* 234(7) (2010) 2175-2182.
- [197] H. Moulinec, P. Suquet, A numerical method for computing the overall response of nonlinear composites with complex microstructure, *Computer methods in applied mechanics and engineering* 157(1-2) (1998) 69-94.
- [198] J.-C. Michel, H. Moulinec, P. Suquet, Effective properties of composite materials with periodic microstructure: a computational approach, *Computer methods in applied mechanics and engineering* 172(1-4) (1999) 109-143.
- [199] R.A. Lebensohn, N-site modeling of a 3D viscoplastic polycrystal using fast Fourier transform, *Acta materialia* 49(14) (2001) 2723-2737.
- [200] P. Eisenlohr, M. Diehl, R.A. Lebensohn, F. Roters, A spectral method solution to crystal elasto-viscoplasticity at finite strains, *International Journal of Plasticity* 46 (2013) 37-53.
- [201] T. Nakamura, T. Wang, S. Sampath, Determination of properties of graded materials by inverse analysis and instrumented indentation, *Acta Materialia* 48(17) (2000) 4293-4306.
- [202] K. Cho, J. Gurland, The law of mixtures applied to the plastic deformation of two-phase alloys of coarse microstructures, *Metallurgical Transactions A* 19(8) (1988) 2027-2040.
- [203] R. Williamson, B. Rabin, J. Drake, Finite element analysis of thermal residual stresses at graded ceramic-metal interfaces. Part I. Model description and geometrical effects, *Journal of Applied Physics* 74(2) (1993) 1310-1320.
- [204] W. Voigt, Ueber die Beziehung zwischen den beiden Elasticitätsconstanten isotroper Körper, *Annalen der physik* 274(12) (1889) 573-587.
- [205] A. Reuß, Berechnung der fließgrenze von mischkristallen auf grund der plastizitätsbedingung für einkristalle, *ZAMM-Journal of Applied Mathematics and Mechanics/Zeitschrift für Angewandte Mathematik und Mechanik* 9(1) (1929) 49-58.
- [206] T. Tamura, Y., and Ozawa, H, *Proceedings of the Third International Conference on Strength of Metals and Alloys* (Institute of Metal and Iron and Steel Institute, London, 1973) p.
- [207] H. Fischmeister, B. Karlsson, Plasticity of two-phase materials with a coarse microstructure, *Z METALLKD* (1977).
- [208] M. Berveiller, A. Zaoui, A simplified self-consistent scheme for the plasticity of two-phase metals, *Res. Mech. Lett* 1(3) (1981) 119-124.

[209] R.G. Stringfellow, D.M. Parks, A self-consistent model of isotropic viscoplastic behavior in multiphase materials, *International journal of plasticity* 7(6) (1991) 529-547.

[210] P. Suquet, Overall potentials and extremal surfaces of power law or ideally plastic composites, *Journal of the Mechanics and Physics of Solids* 41(6) (1993) 981-1002.

[211] I. Chen, A. Argon, Steady state power-law creep in heterogeneous alloys with coarse microstructures, *Acta Metallurgica* 27(5) (1979) 785-791.